High Temperature Forging of AZ31B Magnesium Alloy

by

Tsz Wun Wong

A thesis

presented to the University of Waterloo

in fulfilment of the

thesis requirement for the degree of

Master of Applied Science

in

Mechanical Engineering

Waterloo, Ontario, Canada, 2016

Author’s Declaration

I hereby declare that I am the sole author of this thesis. This is a true copy of the thesis, including any required final revisions, as accepted by my examiners.

I understand that my thesis may be made electronically available to the public.

Abstract

Isothermal uniaxial compression tests were conducted on AZ31B magnesium alloy with the intention of applying the findings to an industrial forging operation. Given the poor workability of magnesium at low temperatures, deformation was conducted in the temperature range of 300°C to 500°C, at strain rates of $10^{-3}s^{-1}$ to $1.0s^{-1}$. Small cylindrical compression samples (Ø10mm by 15mm) were extracted from a commercially available extruded rod in two orientations: along the extrusion direction (ED), and along the transverse direction (TD). In addition, samples were extracted from a large cast ingot and used to evaluate the impact of homogenization on the deformation behaviour.

Both ED and TD samples from the extruded rod exhibited elliptical cross-sections after deformation, with samples deformed at 300°C and high strain rate resulting in fracture. The preferential material flow observed was attributed to the initial texture in the extruded rod. The anisotropy in the ED samples was observed to be dependent on strain rate, with deformation at the lowest strain rate of $10^{-3}s^{-1}$ resulting in circular cross-sections. On the contrary, the anisotropy in the TD samples showed strong dependence on deformation temperature. Deformation at high temperature and high strain rate resulted in minimal anisotropy. Deformation of the extruded material at temperatures below 450°C resulted in the formation of shear bands; therefore these processing conditions should be avoided for bulk deformation processes. Although no viable processing conditions were observed in the as-cast condition, the workability window was greatly improved after homogenization at 450°C for five hours. Deformation could be conducted at high temperature (i.e. above 400°C) and high strain rate (i.e. $1.0s^{-1}$) without the formation of surface cracks. Furthermore, it was observed that a furnace soak in the temperature range of 400°C to 500°C for five hours had suppressed melting of the $Mg_{17}Al_{12}$ phase. In addition, it was observed that higher strains could be achieved by processing at higher deformation temperatures.

The volume fraction of DRX grains and the DRX grain size were observed to increase with deformation temperature and with decreasing strain rate. Comparing the extruded and cast-homogenized samples under the same deformation conditions, it was evident that the extruded material exhibited a higher volume fraction of DRX grains, despite very similar DRX grain sizes.

Slow cooling of the samples after deformation revealed rapid grain growth in the early stages, but longer times at high temperature had little to no impact on the final microstructure. The use of processing maps to predict viable hot working conditions revealed the inadequacies associated with applying such a numerical approach to predict the mechanisms within a dynamic process. The maps proved to be very sensitive to input data, and inconsistencies between the predictions and the actual microstructure were observed for several processing conditions.

Deformation was successfully conducted on both the extruded and cast-homogenized conditions at 500°C and $1.0s^{-1}$, to a true strain of 1.0, with no observable damage to the final microstructures. However, a higher volume of DRX grains was observed with the extruded material. With preference given to high strain rate processing conditions for economic reasons (i.e. higher production rates), the proposed processing condition proved to be viable for an industrial forging application.

Acknowledgements

I would like to thank my supervisor, Dr. Mary Wells, and my postdoctoral mentor, Dr. Amir Hadadzadeh, for their time and effort spent on guiding my research. I would also like to thank Dr. Hamid Jahed and Dr. Steve Lambert for their time spent reviewing my thesis. I wish to thank Mr. Rick Forgett and his staff from the engineering machine shop for producing the countless samples used in this research. Furthermore, I wish to thank Mr. Mark Whitney for operating the Gleeble® and DSC, Dr. Hamid Jahed and Dr. Sugrib Shaha for producing and sharing the XRD pole figures used in this research, Mr. Ralph Dickhout for operation of the ICP-OES, and Ms. Ramneek Kaur for her assistance in conducting the grain size analysis.

In addition, I would also like to thank Dr. Bruce Williams and Mr. Jonathan McKinley from CanmetMATERIALS for providing valuable insight on the practices used in an industrial forging process. Furthermore, I want to acknowledge the financial and material contributions from our partners at the Natural Sciences and Engineering Research Council of Canada (NSERC), Automotive Partnership Canada (APC), Multimatic Inc., Ford Motor Company, the University of Waterloo, Canada Foundation of Innovation (CFI), CanmetMATERIALS, and Centerline.

Finally, I wish to thank my family and friends for their support throughout the duration of my research. My achievements would not be possible without them.

Table of Contents

List of Figures

1.0 Introduction

1.1 Application of Magnesium Alloys

As an engineering material with low density and high specific strength, the potential applications for magnesium alloys are widespread across many industries. Being less than a quarter the density of steel, and approximately two-thirds that of aluminum [1], magnesium is particularly desirable in applications where a reduction in component weight is a key objective. In recent years, magnesium has garnered interest in the automotive industry as more stringent emissions standards are being implemented. Automotive manufacturers have begun investigating methods to reduce fuel consumption, and subsequent exhaust emissions. In addition to performance benefits, the reduction in overall vehicle weight has been identified as one of the most effective approaches to reducing fuel consumption. Figure 1-1 compares the relative changes in fuel consumption for various physical parameters [2].

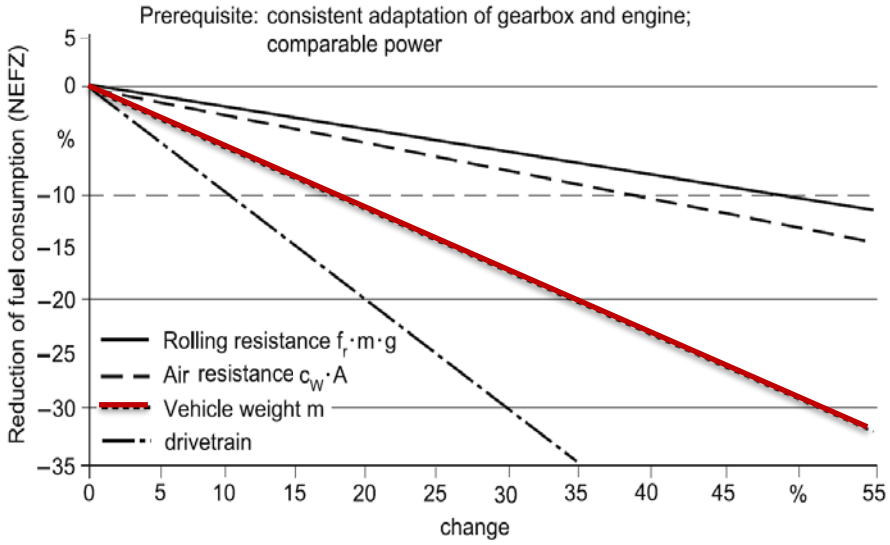

Figure 1-1: Influence of various parameters in fuel consumption of automobiles [2].

The physical properties of magnesium make it an ideal material choice for the light-weighting of automobiles. In Europe, manufacturers such as Volkswagen, Audi, and BMW have developed

prototypes to showcase how magnesium can be integrated into automobiles for various applications. Some examples include gearbox housings, intake manifolds, crankcases, seat structures, and aluminum-magnesium hybrid body panels [2]. Although the components were only produced as showcases of technology, it is evident that the applications of magnesium have mostly been limited to die-cast and sheet-formed components. The same trend follows in North America, where automotive applications of magnesium have been limited to die-cast wheels, housings for powertrain components, and mounting brackets [2]. The relatively poor mechanical properties obtained from casting have prevented the use of magnesium in structural components such as suspension control arms and subframes [2]. However, it has been observed that more favourable mechanical properties can be obtained with wrought alloys, particularly in applications involving cyclic loading [2]. Of the commercially available magnesium alloys, the aluminum-zinc (AZ) family is of high industrial importance, as they are relatively inexpensive and easy to produce.

1.2 Forging of Magnesium Alloys

Over the years, magnesium has not received the same amount of attention as more conventional engineering metals like steels and aluminum alloys. The brittleness of magnesium at low forming temperatures is well documented, and the lack of development and knowledge in the area of magnesium alloys can be traced back to the difficulties associated with forming of the alloys. The limited ductility at low temperatures is attributed to the lack of easily activated slip systems in the hexagonal close-packed (HCP) crystal structure. The commonly observed slip and twinning systems for magnesium crystals are outlined schematically in Figure 1-2. At low forming temperatures, tensile twinning and basal slip can readily occur, however the general lack of contribution from non-basal systems greatly hinders the formability.

The two key benefits of high temperature deformation of magnesium alloys are the lower critical resolved shear stresses (CRSS) required for slip on non-basal planes [2], and the occurrence of dynamic recrystallization (DRX). The temperature dependence of CRSS values for various slip

and twinning systems in pure magnesium single crystals is shown in Figure 1-3 [3]. It is evident that magnesium and its alloys can be successful formed at high temperature.

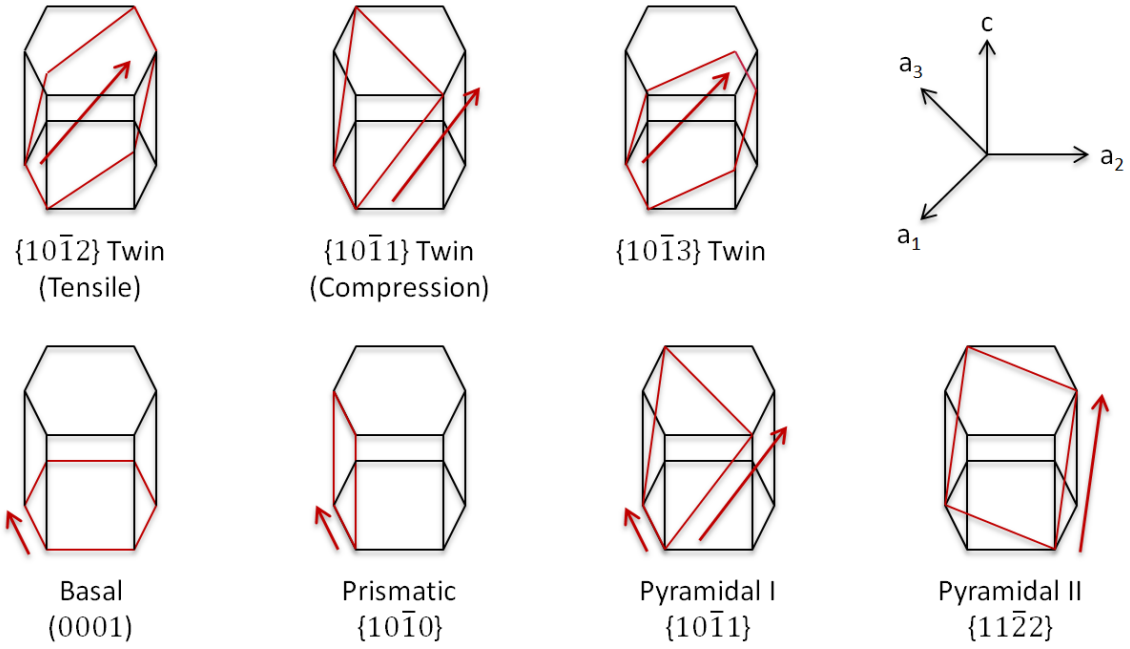

Figure 1-2: Slip and twinning systems in magnesium.

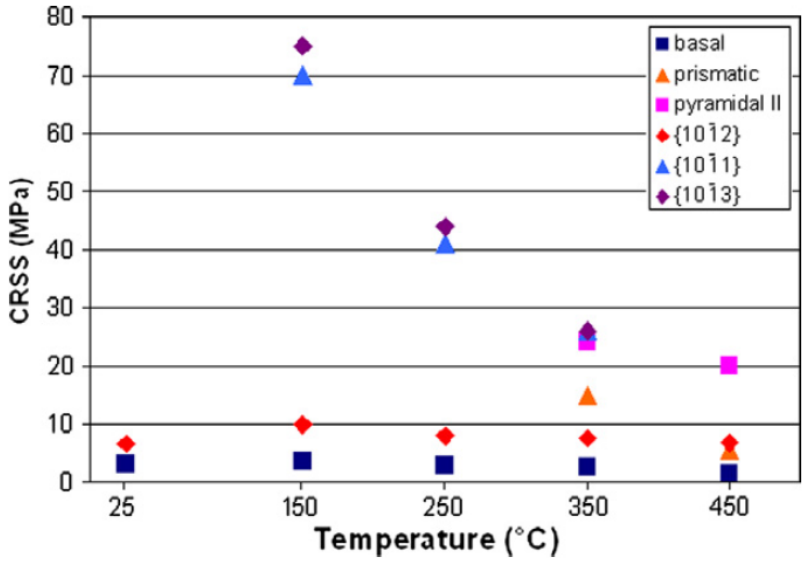

Figure 1-3: CRSS values for various slip and twinning systems in pure magnesium [3].

Despite the knowledge gathered on slip and twinning in magnesium single crystals, slip in polycrystals is more complicated. In order for homogeneous plastic deformation to occur in

polycrystals, there must be no slip at the boundary between two adjacent grains. In other words, the strain components on both sides of the boundary must be the same. Since the orientation of each individual grain is different, the above constraint poses limitations on the slip systems that can be activated. Therefore it is to be expected that the stresses associated with deformation of polycrystals will be higher than those in single crystals [4].

Mechanical anisotropy in compression and tension has been commonly observed with magnesium alloys. Moreover, the activity of twins strongly depends on the texture of the material [2], with activity being the most significant when the direction of loading is parallel to the basal planes [5]. Like many other wrought products however, the development of deformation textures during material processing is inevitable. For example, the hot rolling process produces a strong basal plane texture, where the c-axes of the HCP crystals are aligned normal to the rolling direction. In hot extrusion, an axisymmetric fiber texture is produced where the c-axes are oriented radially and perpendicular to the extrusion axis [6]. Although more desirable mechanical properties, such strength and ductility, have been observed with wrought products, the said properties also show strong directional dependence. On the contrary, die-cast products exhibit minimal anisotropy [7].

In order to produce wrought products, the alloy must first be cast into ingot form. The cast stock used to produce wrought products is typically direct chill (D.C.) cast and homogenized at 300°C to 500°C prior to extrusion or forging. In general, extrusion operations are conducted in the temperature range of 300°C to 450°C, at strain rates of $10^{-3}s^{-1}$ to $10^{3}s^{-1}$, with dies at 25°C to 50°C below the workpiece temperature [2]. It has been observed that a finer initial grain size improves both extrudability [2] and forgeability [8].

1.3 Problem Statement

1.3.1 Scope

The current study was part of a larger investigation on the usage of forged magnesium alloys in fatigue-critical automotive applications. The investigation involved three magnesium alloys

(AZ31, AZ80 and ZK60), in both extruded and cast conditions, as potential candidates for forging and industrial trials at CanmetMATERIALS on both the 110-ton and 500-ton forging presses. The objective of the overall investigation was to identify the most promising alloy and the associated processing condition(s) for forging of a fatigue-critical automotive suspension component. Separate studies investigated finite element modeling of the forging process, and the fatigue and corrosion behaviours of the magnesium forgings.

In the current study, experimental work was conducted on commercially available AZ31B magnesium alloy. Three starting conditions were investigated: as-cast, cast-homogenized, and as-extruded. Isothermal uniaxial compression tests were conducted in the temperature range of 300°C to 500°C, at constant true strain rates of $10^{-3}s^{-1}$ to $1.0s^{-1}$, to various final true strains using the Gleeble 3500® thermal-mechanical simulation system available at the University of Waterloo. The lower and upper temperature limits were chosen to readily activate non-basal slip systems, and to avoid large-scale melting of the alloy as a result of deformation heating. The lower and upper strain rate limits were chosen with consideration to economically feasible production rates, and instrument limitations in controlling a constant true strain rate.

1.3.2 Objectives

The compression tests were designed to replicate high temperature open die upsetting, with the intention of applying the findings to better understand the key parameters involved in an industrial forging operation for AZ31B, and to identify viable processing conditions. The objectives of the study were to investigate:

- The implications of starting condition on the deformation behaviour
- The effects of homogenization on workability of the cast material
- The implications of initial texture on anisotropy
- The effects of thermal-mechanical processing condition (i.e. temperature and strain rate) on the workability and subsequent microstructure
- The evolution of microstructure with respect to strain
- The processing conditions resulting in favourable microstructures

2.0 Literature Review

2.1 Magnesium Slip Systems and Single Crystal Deformation

Like many other materials with a hexagonal close-packed (HCP) crystal structure, it has been widely documented that magnesium alloys exhibit very limited workability at low temperatures. The HCP crystal structure has three predominant slip systems: slip along the close-packed basal plane (i.e. basal slip), prismatic slip, and pyramidal slip. Von Mises had proposed in 1928 that five independent strain components are required to achieve homogeneous plastic deformation. Due to the fact that pyramidal slip can be represented as a combination of basal and prismatic slip, a material with a HCP crystal structure only has four independent slip components. Therefore it has been suggested that deformation twinning accounts for the fifth strain component required for homogeneous deformation [4].

Although magnesium is very difficult to form at low temperatures, it has been observed that the critical resolved shear stress (CRSS) required for slip on the non-basal planes is greatly reduced at elevated temperatures. Since the mechanisms activated during deformation depend on the direction of loading relative to the crystallographic orientation, as well as the CRSS required for each slip system, it is important to understand how the CRSS varies under different thermal-mechanical processing conditions. In 2011, Chapuis and Driver [3] studied the temperature dependency of slip and twinning using magnesium single crystals under plane strain compression. The single crystal compression samples were produced in four different orientations, allowing for the independent observation of (1) tensile twinning, (2) basal slip, (3) compressive twinning, and (4) prismatic slip. The stress-strain curves are presented in Figure 2-1.

(1) It was confirmed that tensile twinning can readily occur up to a strain of 6.5% (i.e. until the entire crystal is twinned), and it was seen that very little work hardening occurs up to that strain. However the flow stress beyond 6.5% strain exhibits substantial work hardening, as the twinned crystal resists basal slip [3].

(2) It was observed that the flow stress decreases with increasing temperature; however the flow stress obtained at room temperature is lower than those at 150°C and 250°C [3].

(3) Rapid work hardening was observed, followed by rapid flow softening. Compression twins were not observed at 450°C [3].

(4) Compression and tensile twins were observed at temperatures below 250°C. However prismatic slip dominated at temperatures of 350°C and 450°C, with peak stresses observed at strains of 20% and 25% respectively. It is believed that the peak is a result of crystal rotation during deformation [3].

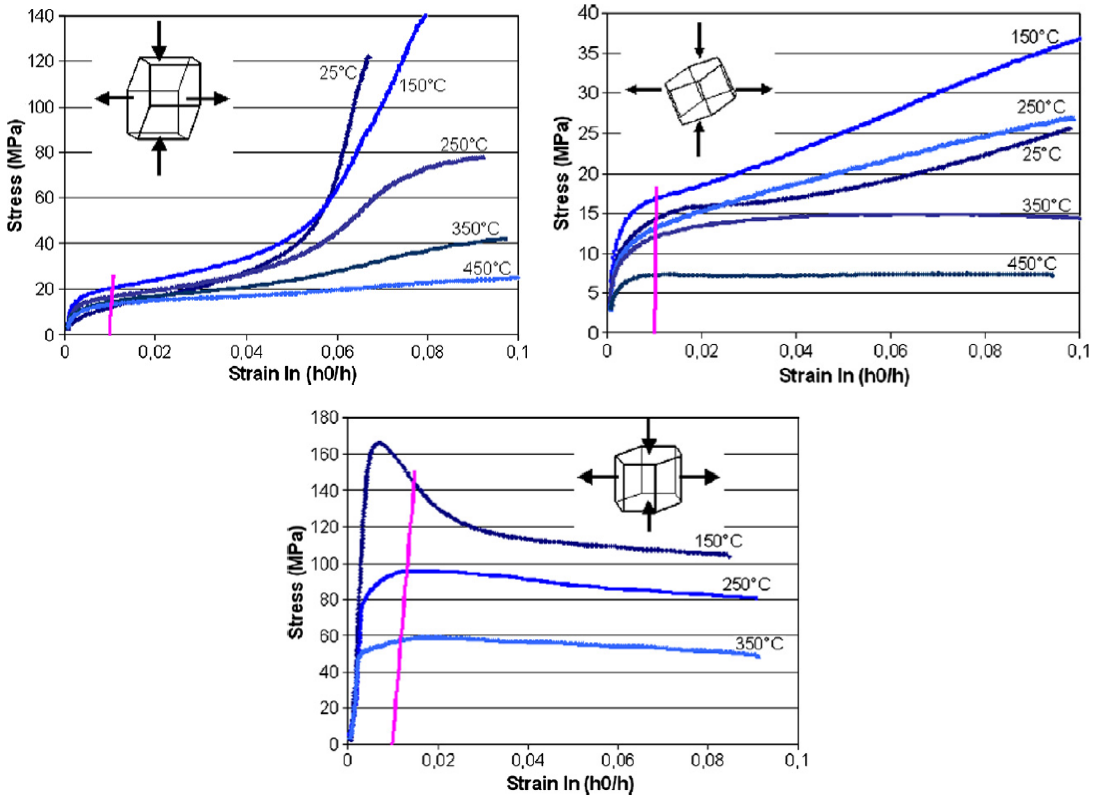

Figure 2-1: Flow stress curves corresponding to: (1) tensile twinning - top left, (2) basal slip - top right, and (3) compressive twinning - bottom [3].

From the results of Chapuis and Driver [3], it is evident that the mechanisms which operate under the specified deformation conditions can influence the flow stress behaviour at low strains. However it is equally important to understand the implications of elevated temperature deformation and the mechanisms that operate during large plastic flow.

2.2 Dynamic Restoration Mechanisms and Microstructure Evolution

Restoration mechanisms that occur in materials during high temperature deformation allow for large strains to be imparted without the workpiece undergoing fracture. One mechanism that is commonly observed in aluminum alloys and ferritic steels is dynamic recovery. Like in static recovery, dynamic recovery sees the elimination of dislocations. The stress-strain curve of a material undergoing dynamic recovery is characterized by strain hardening, followed by a steady state flow stress [9]. At the early stages of deformation, the dislocation density increases and the material undergoes strain hardening. However as deformation progresses and dislocation density rises, the driving force and therefore the rate of recovery increase. A steady state flow stress is observed when the rate of strain hardening matches that of recovery. The microstructure obtained from dynamic recovery is characterized by serrated grain boundaries, and the presence of numerous subgrains within each grain interior [9].

Another restoration mechanism that can occur during hot deformation is dynamic recrystallization. Unlike static recrystallization, which occurs at high temperatures in stationary workpieces, dynamic recrystallization (DRX) occurs during hot deformation. In general, it has been observed that grain refinement and flow softening are signatures of DRX. Dynamic recrystallization can be further classified as continuous (CDRX) or discontinuous (DDRX). DDRX is characterized by the nucleation and growth of new grains at previously existing grain boundaries. However intragranular nucleation has been observed at very low strain rates, and in materials with large initial grain size [9]. As deformation progresses, the dislocation density in the grains increases, and the driving force for grain growth decreases until growth is no longer observed. In addition, the nucleation of new grains adjacent to growing grains can further hinder growth. Bulging of the grain boundaries is considered to be an early sign of DDRX, and the nucleation of new grains at the boundaries follows [9].

The stress-strain curve of a material undergoing DDRX can exhibit a single broad peak, or several peaks, followed by flow softening. Each observed peak represents one cycle of work hardening followed by recrystallization. The number of peaks is dependent on the timing of recrystallization cycles. Several peaks can be observed if the recrystallization cycles do not overlap (i.e. one cycle finishes before the start of the next), or a single broad peak can be

observed if the cycles overlap. Each DDRX cycle increases the volume fraction of recrystallized grains, and the cycles continue until the material has been fully recrystallized [9]. It has been observed that the mean DRX grain size reaches a steady state value and does not change with increasing DRX volume fraction. Furthermore, DDRX is only observed after a critical strain (ε_c) has been reached. The critical strain has been observed to decrease with stress, while the DRX grain size increases with decreasing stress [9].

In addition to DDRX, CDRX can occur during high temperature deformation. Dynamic recrystallization of the continuous type can be further classified into two processes: geometric CDRX, and rotation CDRX. Geometric CDRX is often observed in materials that have undergone processes resulting in large cross-sectional reductions (i.e. hot rolling, extrusion, drawing, etc.). The serrated grain boundaries from dynamic recovery become close together as the grains are flattened at high strains, the proximity allows for the interpenetration of the high angle grain boundaries. The microstructure after geometric CDRX consists of small equiaxed grains separated by high angle boundaries. Furthermore, it has been seen that the occurrence of geometric CDRX requires high strains when the associated stresses are high [9]. Unlike geometric CDRX which involves the interpenetration of high angle boundaries, rotation CDRX (also known as strain-induced CDRX) is characterized by strain-induced subgrain rotation. It has been observed that the subgrains along the grain boundaries rotate to produce a misorientation gradient from the surface to the centre of the grain, and often results in a partially recrystallized microstructure. Rotation CDRX has often been observed in materials where the movement of dislocations is inhibited by the lack of slip systems (i.e. like in magnesium alloys) [9].

There is still debate over the restoration mechanisms exhibited by magnesium alloys during hot deformation. In 2003, Yang et al. [10] observed the presence of kink bands in the microstructure of AZ31 at low strain, along with grain boundary sliding and grain rotation at higher strain. Orientation imaging microscopy (OIM) had shown the presence of medium angle grain boundaries along the corrugated high angle boundaries. An OIM image of the microstructure at a strain of 0.1 is shown in Figure 2-2. It was observed that the medium angle boundaries corresponded to the kink bands observed with optical microscopy. It was proposed that the kink bands fragmented the original grains and the newly formed grains rotated upon further straining to produce high angle boundaries. OIM line scans across the grains revealed a misorientation

gradient synonymous with rotation CDRX. Furthermore, it was observed that new, randomly oriented grains developed homogeneously throughout the microstructure during flow softening, and the average misorientation angle increased at the same time. It was seen that the size of the fragmented regions at low strain roughly corresponded to the size of DRX grains at high strain, and the boundaries transitioned from low angle to medium or high angle. For deformation at 400˚C, it was noted that the volume fraction of dynamically recrystallized grains remained at 0.85 and the average misorientation angle remained at a constant 42˚, beyond a strain of 0.5. The observations made by the authors led to the conclusion that the development of new grains was a result of rotation CDRX, and the flow softening behaviour was due to the evolution of texture.

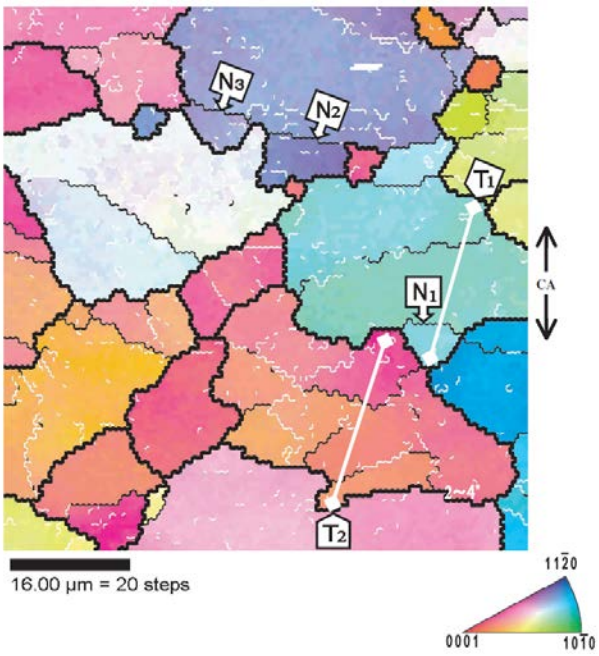

Figure 2-2: OIM mage after deformation at 400˚C and $10^{-3}s^{-1}$ to a strain of 0.1. The thin white, thin black and thick black lines correspond to misorientation angles of > 2˚, > 4˚ and > 15˚ respectively [10].

In a separate study conducted by Fatemi-Varzaneh et al. [11] in 2007, the effects of deformation condition on the restoration mechanisms and resulting microstructures in AZ31 were investigated. It was observed that the compression tests conducted at the highest temperature of 450˚C and strain rates slower than $0.01s^{-1}$ rarely produced new high angle grain boundaries. The observation suggested the operation of CDRX under those conditions. On the contrary, deformation at lower temperatures and/or higher strain rates suggested the occurrence of DDRX.

Furthermore, it was observed that both the volume fraction and size of DRX grains decreased with temperature and/or increasing strain rate. The stress-strain curves showed that the rate of work hardening increased with decreasing temperature and/or increasing strain rate. As the work hardening increased, the driving force for grain growth decreased and the DRX grain size became stagnant. It was proposed that the volume fraction of DRX grains was higher for high temperature and/or low strain rate conditions because the DRX grain size was larger, and fewer DDRX cycles were required to achieve a fully recrystallized microstructure. The volume fraction of DRX grains was observed to increase in a sigmoidal behaviour with strain; but like Yang et al. [10], Fatemi-Varzaneh et al. [11] had observed a steady state DRX grain size.

Moving forward to 2008, Al-Samman and Gottstein [12] also studied the microstructural evolution of AZ31 during hot deformation. DRX was observed even at 200˚C, whereby the twins provided high energy sites for DRX to occur. It was shown that DRX within the twins weakened the macrotexture of the sample. Furthermore, it was seen that the grain size was more sensitive to strain rate at high temperature. Samples extracted in different orientations also showed no statistically significant difference in average grain size under any of the investigated processing conditions. A plot illustrating the influence of temperature, strain rate and sample orientation on the observed average grain size is provided in Figure 2-3. Nomenclature in Figure 2-3 follows: CD [Compression Direction] - angle with respect to - ED [Extrusion direction]. Furthermore, strong post-deformation textures were observed under all test conditions.

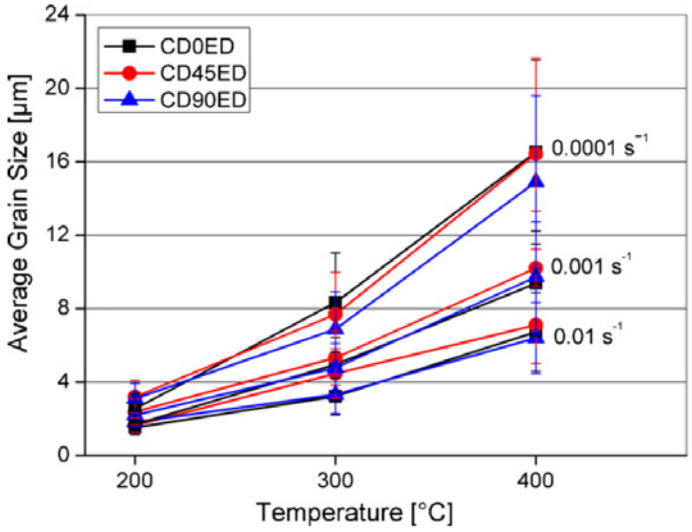

Figure 2-3: Average grain sizes observed under various deformation conditions [12].

2.3 Effects of Thermal-mechanical Processing Conditions

In 2004, Barnett et al. [13] observed that a finer initial grain size resulted in lower flow stresses during deformation of AZ31. Furthermore, it was observed that the finer initial grain size produced an equiaxed and fine-grained DRX microstructure, where the coarser initial grain size produced a mixed microstructure consisting of deformed and equiaxed DRX grains. Later in 2007, Beer and Barnett [14] conducted a thorough study on the microstructural evolution of both wrought and cast AZ31 for various processing conditions. At a strain of 1.0, it was observed that the wrought material exhibited a higher volume fraction of DRX grains, as well as a finer DRX grain size, for all investigated deformation conditions. The post-deformation microstructures are provided for both wrought and cast samples in Figure 2-4 and Figure 2-5 respectively.

Furthermore, it was observed that a finer DRX grain size was obtained with the wrought AZ31 under all strain levels, and a substantially higher volume fraction of DRX grains was observed at high strain. The microstructures obtained after deformation at 350˚C and $0.01s^{-1}$ for the wrought and cast samples are presented in Figure 2-6 and Figure 2-7, respectively [14]. In addition to the findings on grain size evolution, electron backscatter diffraction (EBSD) maps revealed that the cast material exhibited misorientation gradients within the large grains, indicating the operation of CDRX [14].

Separate studies by Sun et al. [15] in 2010 and Kim et al. [16] in 2012 observed the formation of shear bands during deformation of AZ31 at 200˚C and 300˚C, respectively. Sun et al. [15] had observed that the shear bands consisted of fine DRX grains. It was proposed that strain localization was due to rotation of the DRX grains during deformation, resulting in geometric softening of the region. Kim et al. [16] had observed the formation of shear bands along directions of maximum shear during compression. It was proposed that twins formed during the early stages of deformation had split the coarse grains, and provided high energy sites for the nucleation of DRX grains. As deformation progressed, the strain became localized in the strain-free DRX regions until fracture was observed at the boundary of the DRX and deformed regions due to strain incompatibility [16].

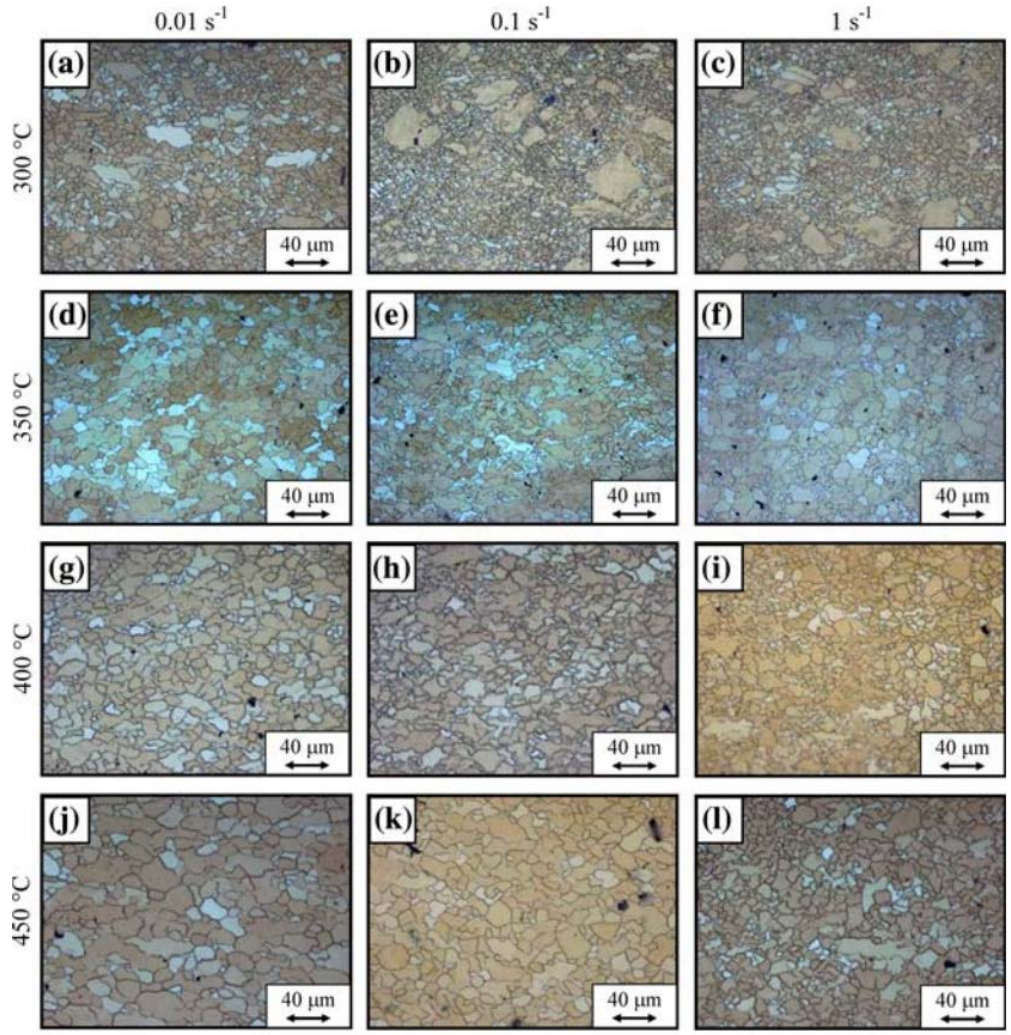

Figure 2-4: Microstructures of wrought AZ31 deformed under various conditions to a strain of 1.0 [14].

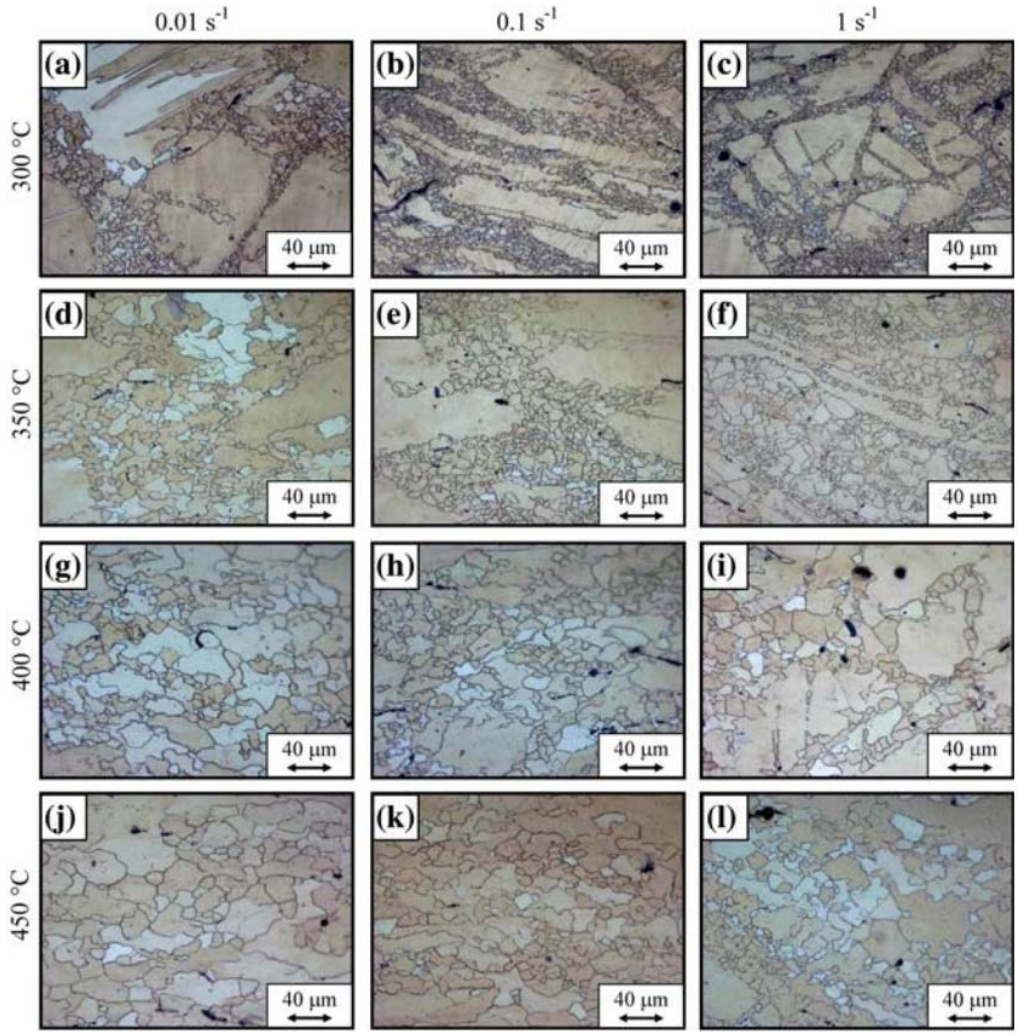

Figure 2-5: Microstructures of cast AZ31 under various deformation conditions to a strain of 1.0 [14].

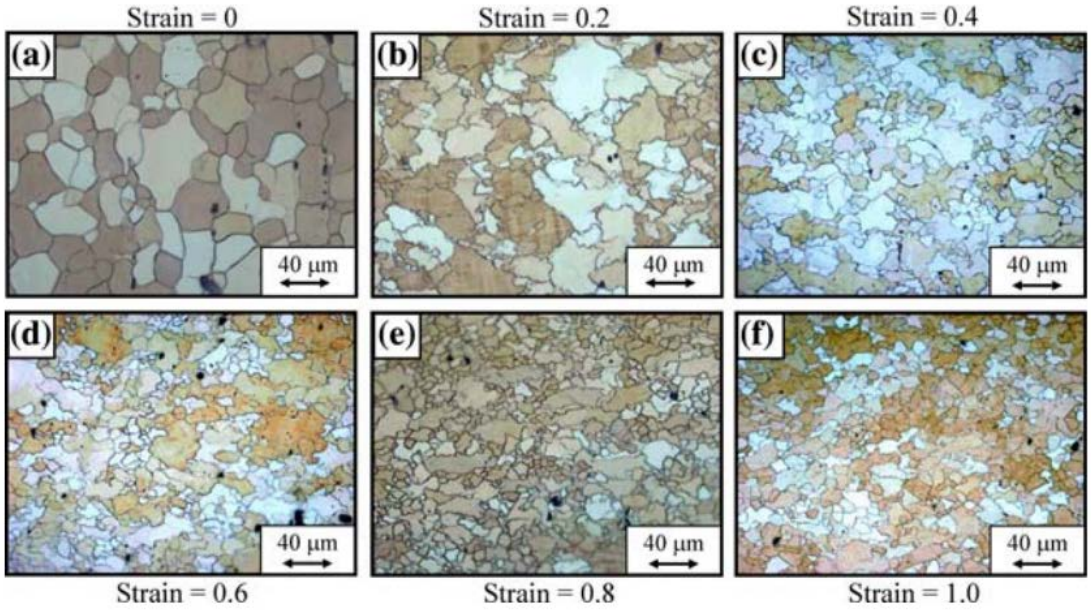

Figure 2-6: Microstructures of wrought AZ31 after deformation at 350˚C and $0.01s^{-1}$ to various strains [14].

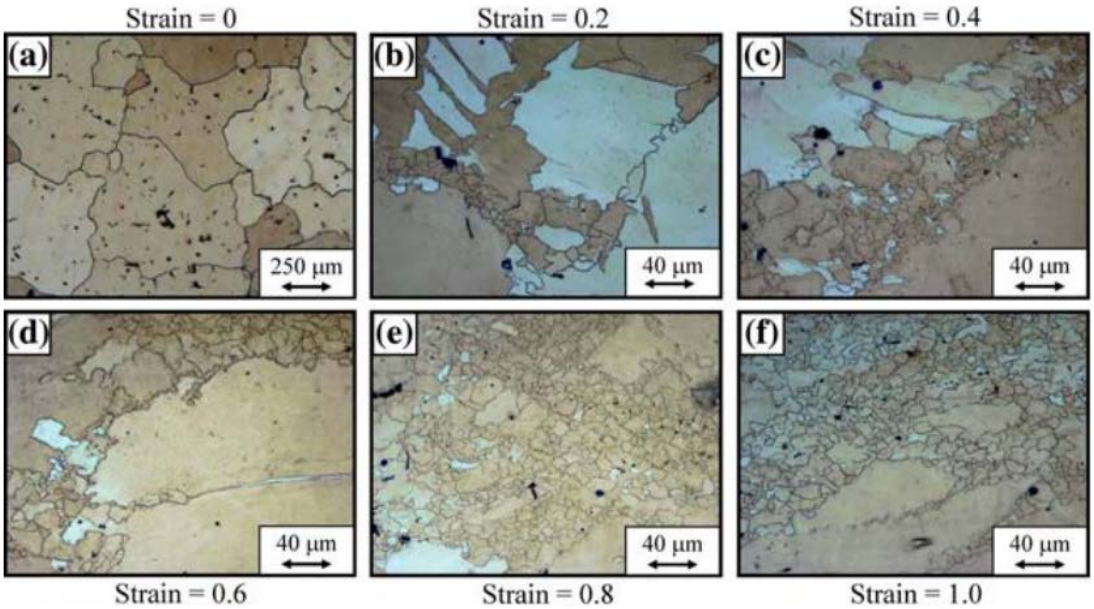

Figure 2-7: Microstructures of cast AZ31 after deformation at 350˚C and $0.01s^{-1}$ to various strains [14].

2.4 Role of Initial Texture on Anisotropy of Material Flow

Similar to cubic metals, it is common for HCP metals to form strong textures from processing. A number of studies have documented the textures generated from the processing of magnesium alloys, and also the implications of such textures on further deformation. In 2003, Yukutake et al. [17] studied the anisotropy in mechanical properties for AZ31. It was observed the samples extracted from the surface of the rolled sheet exhibited the strongest basal plane texture, as well as the most severe mechanical anisotropy. Room temperature compression tests revealed low yield points followed by rapid strain hardening for the transverse and rolling directions. The behaviour was attributed to tensile twinning that can readily occur under compression. Moreover, it was observed that the compression samples along the transverse and rolling directions exhibited elliptical cross-sections after deformation. When the deformation temperature was raised to 300˚C however, the anisotropy in the stress-strain behaviour had disappeared.

In a separate study conducted by Lee et al. [18] in 2011, the tensile twinning signature in the stress-strain behaviour of samples along the rolling direction was again observed for deformation temperatures below 300˚C. Consistent with previous observations by Yukutake et al. [17], the samples exhibited elliptical cross-sections for deformation temperatures below 400˚C. Furthermore, Lee et al. [18] had attributed the tendency towards twinning and thus the resulting anisotropy of material flow to the initial texture of the sheet. The mechanical anisotropy observed under tensile loading was also observed to decrease with increasing temperature, as more slip systems became active.

The dependence of anisotropy on both strain rate and temperature was studied by Dai et al. [19] in 2011. It was observed that twins were only present in the microstructure for low temperature and high strain rate conditions. Therefore it was suggested that the twinning mechanism is accelerated at high strain rate. Furthermore, samples extracted in various orientations of the hot rolled plate exhibited the same basal plane texture after compression, but of varying strengths, regardless of the starting texture. Additional discussion on the evolution of texture will be provided in a later section. Dai et al. [19] had also observed that the degree of flow anisotropy decreases with strain rate, as well as with increasing temperature. The tensile twin signature was again observed in the stress-strain curve for the sample oriented along the rolling direction;

however twins were no longer observed at strains above 0.2, suggesting that slip became the dominant deformation mechanism at higher strains. The stress-strain curves for the two orientations, as well as the corresponding microstructures, are shown in Figure 2-8.

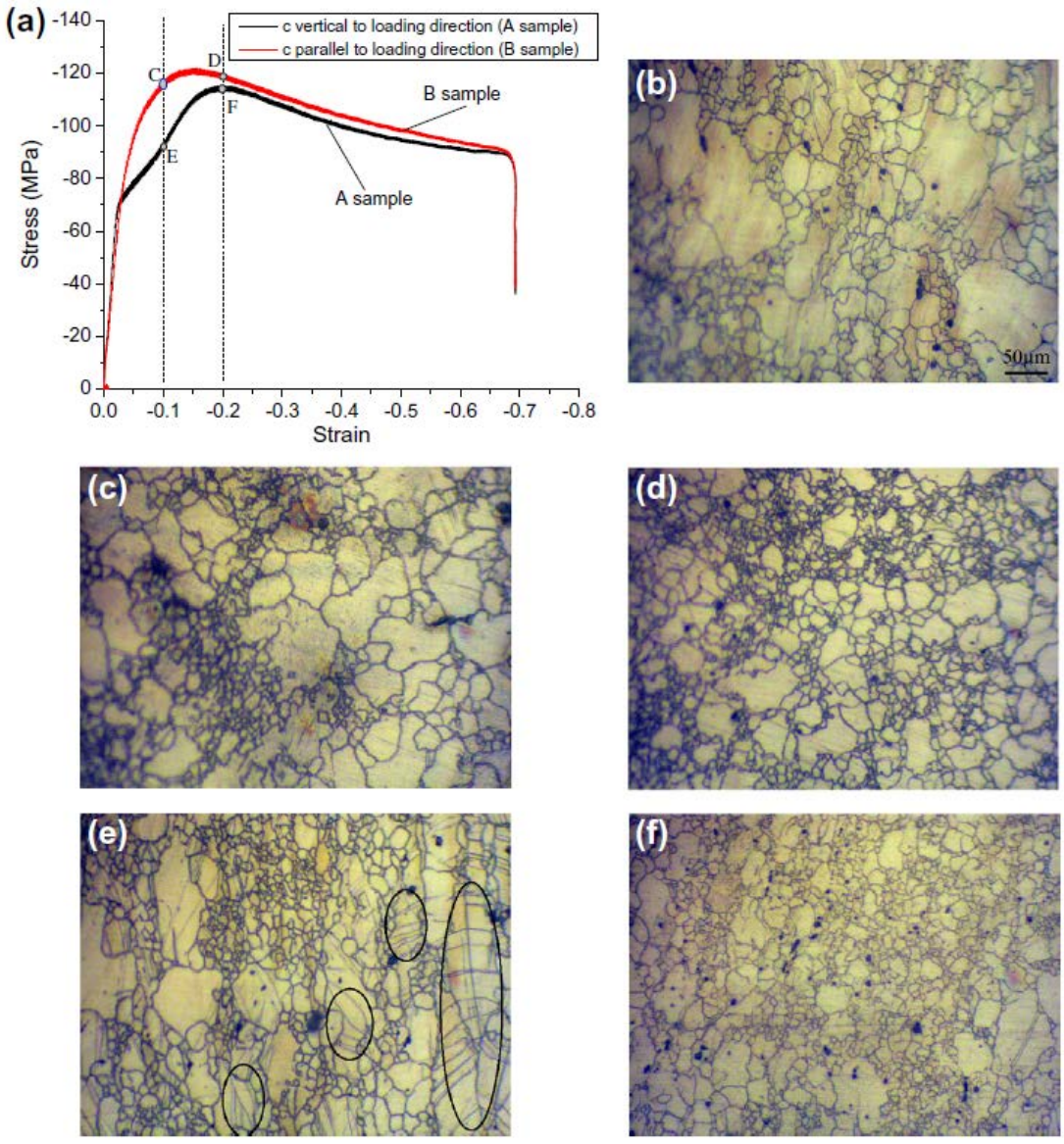

Figure 2-8: Stress-strain behaviour of samples during compression at 300˚C and $1s^{-1}$, with snapshots of the corresponding microstructures for the strains illustrated in (a) [19].

In addition to the studies mentioned previously, Rao et al. [20] had conducted a forging study to further investigate the anisotropy observed in magnesium alloys. For the samples oriented along

the rolling direction, it was observed that the major axis of the ellipse corresponded to the transverse direction of the sheet, and vice versa for the samples along the transverse direction. However it was seen that the samples forged at 450˚C and 500˚C and low strain rates resulted in near circular cross-sections, with uniform microstructures throughout. On the contrary, the samples oriented along the normal direction showed no anisotropy under any investigated condition. Images of the forged samples from each orientation are shown in Figure 2-9. The anisotropy observed was attributed to preferential material flow resulting from prismatic slip at deformation temperatures below 350˚C. It was suggested that pyramidal slip, combined with DRX, at temperatures above 350˚C negate the effects of initial texture and near isotropic flow is achieved at high temperature. In addition to the anisotropy, it was observed that forging at a strain rate of $0.1s^{-1}$ resulted in abnormal grain growth for all samples.

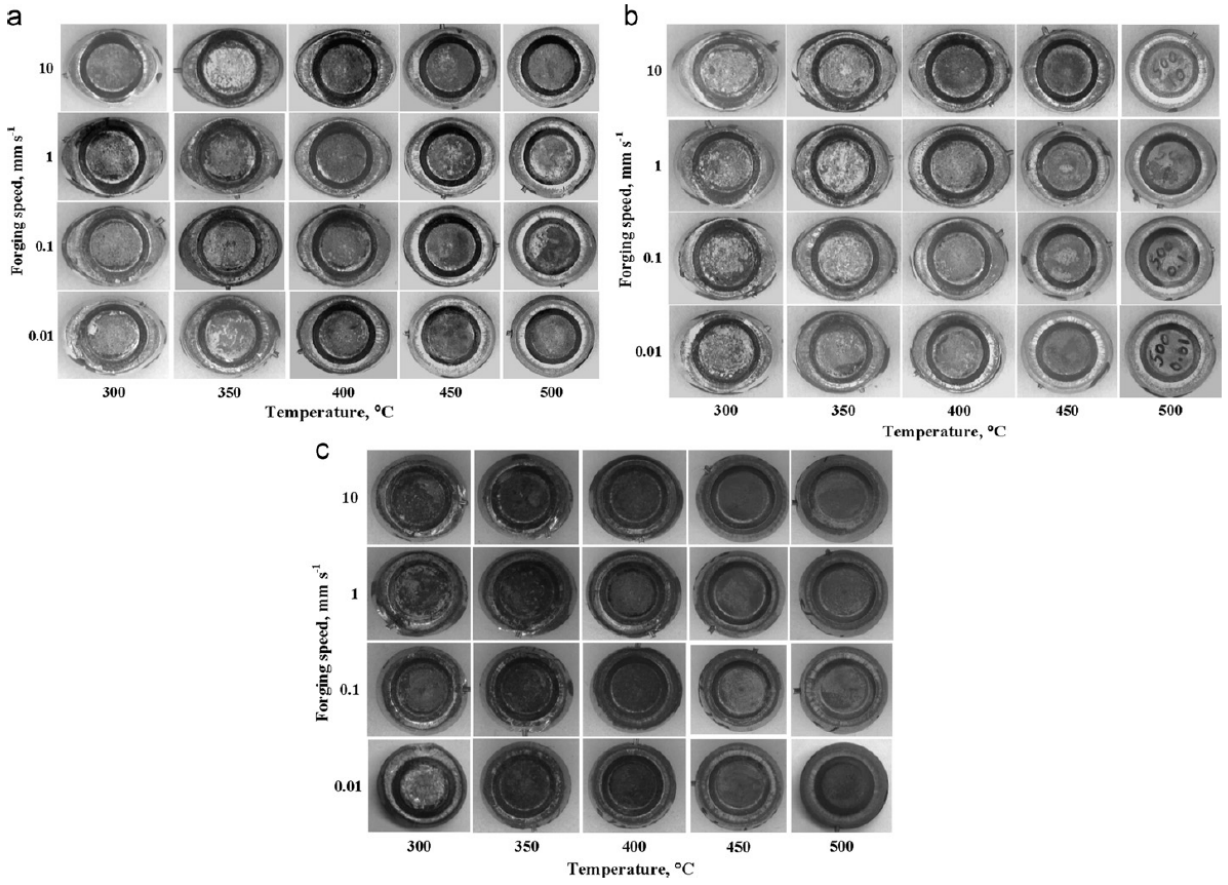

Figure 2-9: Images of forgings produced under various deformation conditions. Forging direction is oriented along the a) rolling b) transverse c) normal directions [20].

2.5 Effects of Annealing or Homogenization Prior to Hot Deformation

From a materials processing perspective, any high temperature heat treatment has the potential to alter the grain structure and/or texture of a material. Therefore it is important to understand the implications of homogenization (on a cast material) and annealing (on a wrought material) on the deformation behaviour. In 2009, Prasad and Rao [21, 22] evaluated the impact of a homogenization heat treatment on the hot deformation behaviour of cast AZ31. Intermetallic compound ($Al_2Mg_3Zn_3$) and eutectic phase ($Mg_{17}Al_{12}$) were observed at the grain boundaries, with Al-Mn intermetallic particles present within the matrix of the initial cast microstructure [23]. Compression samples were homogenized for five hours at 450˚C and subsequently furnace cooled prior to compression. It was seen that the intermetallic $Al_2Mg_3Zn_3$ and eutectic phase had dissolved after homogenization, and only fine Al-Mn intermetallic particles remained in the matrix. In 2014, Mohammadi et al. [24] had observed the rapid dissolution of the eutectic phase $Mg_{17}Al_{12}$ once homogenization temperatures exceeded the eutectic temperature of 437˚C. The finding supports the post-homogenization microstructure observed by Prasad and Rao [22] and Murai et al. [23]. For Prasad and Rao [22], it was observed that the flow stress of the homogenized samples was lower than their cast counterparts, with the exception of those at strain rates above $1s^{-1}$, where the cast samples experienced fracture.

Examination of the post-deformation microstructures by Prasad and Rao [22] revealed that homogenization had widened the working window and eliminated regimes of flow instability that were previously observed at temperatures below 475˚C. With consideration to the higher strain rates that would be desirable for industrial forging applications, it was concluded that the cast material should be formed at 350˚C with a strain rate of $1s^{-1}$. On the contrary, the working window of the cast-homogenized material was enlarged to temperatures of 300˚C to 450˚C and strain rates of $1s^{-1}$ to $10s^{-1}$. Microstructures corresponding to those working conditions are shown in Figure 2-10. In 2013, Bajargan et al. [25] also studied the deformation behaviour of cast AZ31 after homogenization at 400˚C for 24 hours. It was evident that processing at increasingly higher temperatures allowed for deformation to be performed at higher strain rates without the occurrence of flow localization.

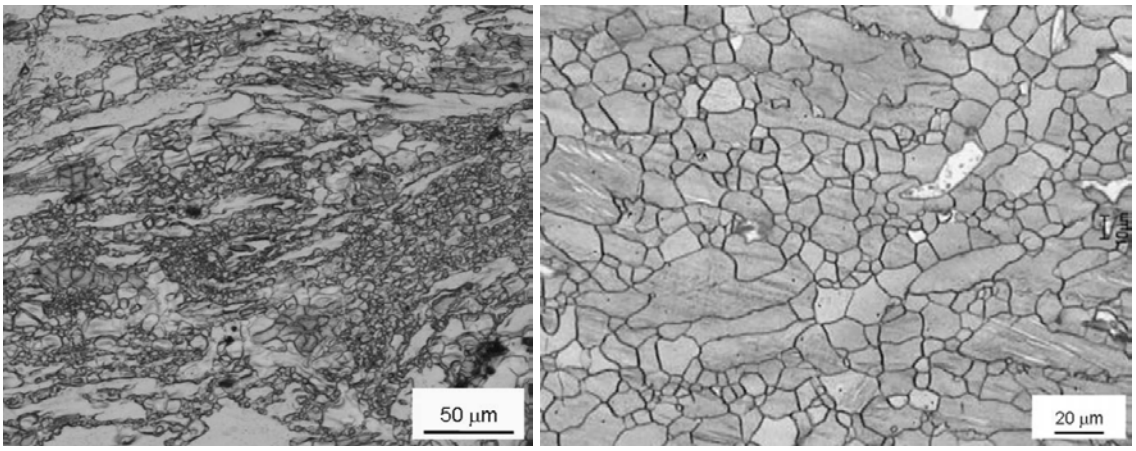

Figure 2-10: Microstructures at a strain of 0.7, for the cast sample (400˚C and $1s^{-1}$) - left, and cast-homogenized sample (400˚C and $10s^{-1}$) - right [22].

It had been observed in the previous section that the anisotropy of flow is attributed to the initial texture present in the material; therefore it is important to understand how the texture evolves during annealing. In 2002, Pérez-Prado and Ruano [26] conducted annealing treatments at 450˚C and 520˚C, for times of 30 minutes, 3 hours, and 17 hours on AZ31. A grain size gradient was observed across the section of the sheet, with finer grains at the surface. The starting texture was observed to vary through the thickness of the sheet. The pole figures obtained from the surface and the middle of the sheet are shown in Figure 2-11. Upon heat treatment, it was observed that the grain size increased with annealing temperature, as well as with annealing time. The average grain size was largely unchanged between 30 minute and 3 hour treatments, but had substantially increased after 17 hours. Abnormal grain growth was observed at the surface after annealing at 450˚C for 30 minutes. Furthermore, the strengthening of the $\{11\bar{2}0\}$ pole suggested that abnormal grain growth occurred in grains with that orientation. The texture after annealing at 520˚C for 3 hours is shown in Figure 2-12. Despite changes in local texture at the surface, it was shown that even after annealing at 520˚C for 19 hours, the bulk texture showed a strong $\{11\bar{2}0\}$ pole as a result of significant grain growth.

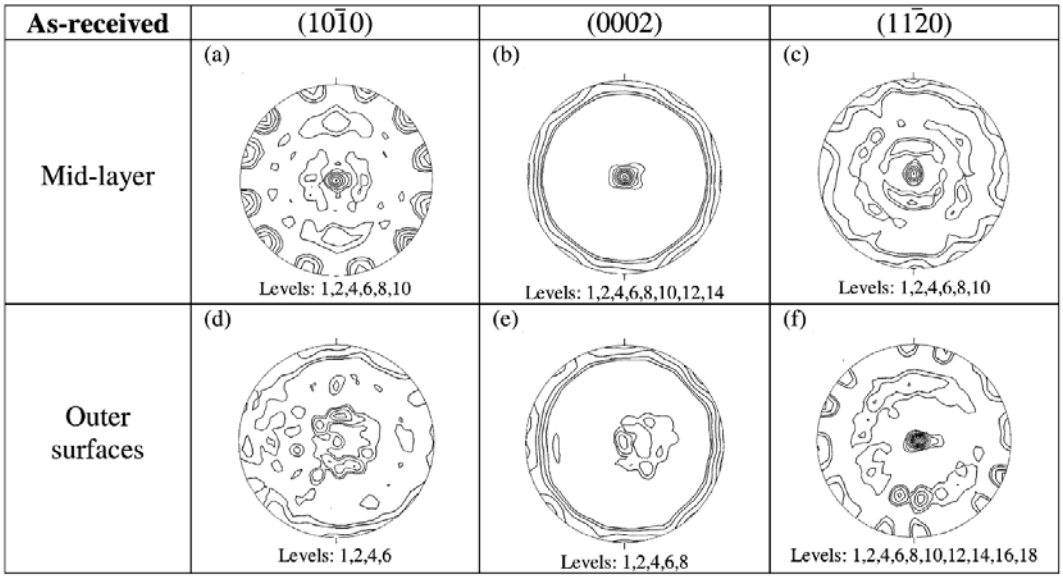

Figure 2-11: Pole figures for middle and surface layers of as-received AZ31 sheet [26].

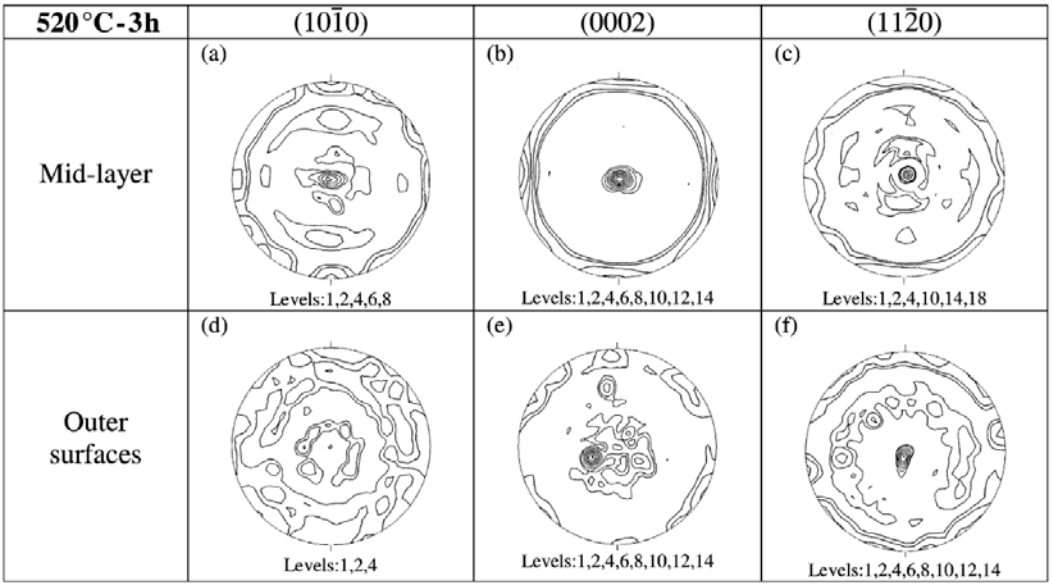

Figure 2-12: Pole figures for middle and surface layers after annealing at 520˚C for 3 hours [26].

Moving forward to 2010, Yi et al. [27] had studied the evolution of texture upon annealing of an AZ31 extruded rod at 400˚C for times ranging from 180 to 1800 seconds. The strong <10$\bar{1}$0> fiber texture was observed to weaken with increasing annealing time, while the <11$\bar{2}$0> pole increased in strength. The two pole intensities are plotted against annealing time in Figure 2-13.

The initial microstructure consisted of equiaxed DRX grains, alongside elongated deformed grains. However, high angle grain boundaries were not observed adjacent to the elongated grains, suggesting that rotation CDRX was in operation. EBSD maps showed that the equiaxed grains adjacent to the deformed grains developed high angle boundaries upon annealing. The formation of high angle grain boundaries, along with the strengthening of the <$11\bar{2}0$> pole, suggested that the grains rotated from the <$10\bar{1}0$> to the <$11\bar{2}0$> orientation during grain growth. After annealing for 1800 seconds, it was observed that the <$11\bar{2}0$> pole was still dominant, suggesting that grain growth was preferential in grains with the <$11\bar{2}0$> orientation.

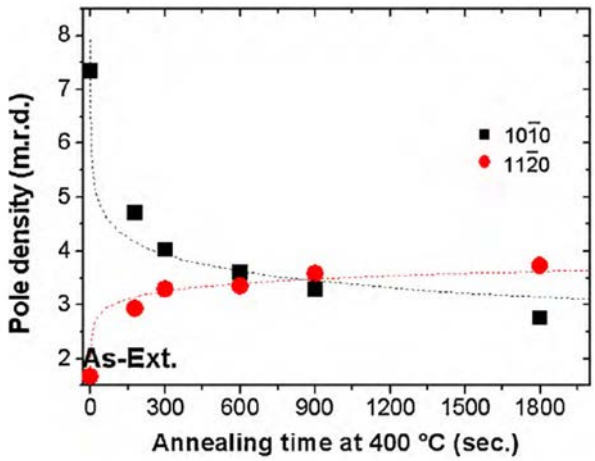

Figure 2-13: Pole densities as a function of annealing time [27].

2.6 Texture Evolution during Hot Compression

In addition to the changes in texture during homogenization and annealing, it had been observed by several researchers that the texture evolves during deformation. In 2005, Li et al. [28] observed that all AZ31 plane strain compression samples had evolved to a basal plane texture after deformation, regardless of the initial texture. The samples oriented along the normal direction, which exhibited a basal plane texture prior to compression, had undergone strengthening of the texture during deformation. Furthermore, it was observed that the evolution

of texture could be accelerated (i.e. with respect to strain) by increasing the deformation strain rate. Similar observations in texture evolution were reported by Wang et al. [29] in 2008.

In 2009, Yang et al. [30] had proposed that the softening behaviour seen in the stress-strain curves of AZ31 for samples oriented along the extrusion direction could be attributed to texture evolution (i.e. geometric softening). At a strain of 1.2, it was seen that the grains had rotated almost 90˚ to have their c-axes aligned with the compression axis, and had rotated through orientations of soft slip. The evolution of texture observed for various strains is shown in Figure 2-14. Kink bands that were observed at low strain were said to have fragmented the existing grains, and the fragmented regions developed into high angle boundaries with minimal changes in size. The development of new grains was observed to be very rapid during the flow softening regime; however a fully recrystallized microstructure was not obtained even after steady state flow. In addition, the average misorientation angle, the volume fraction of DRX grains, and hardness values showed no differences between samples of different orientation.

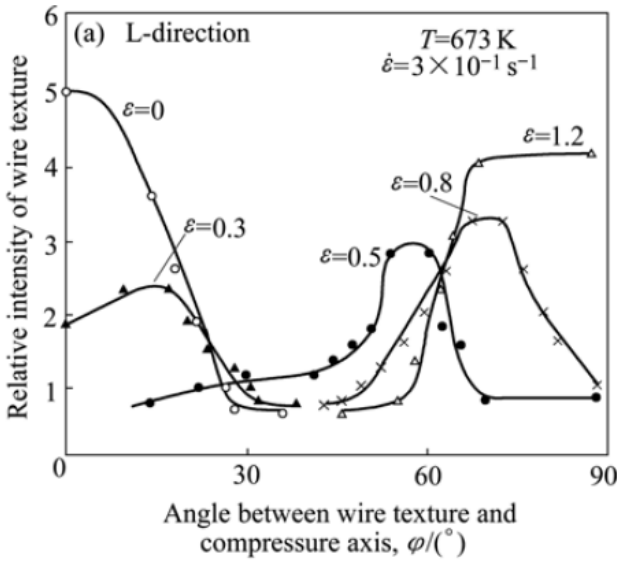

Figure 2-14: Evolution of texture at various stages of deformation [30].

2.7 Texture and Microstructural Evolution upon Subsequent Cooling

Post-deformation texture and microstructural evolutions are static processes and must be studied separately from the dynamic processes occurring during deformation. In 2003, Barnett [31] had observed post-deformation grain growth and the weakening of textures after annealing. Yang et al. [32] had studied the annealing behaviour of AZ31 after hot compression at two different strain rates. After deformation, the samples were subsequently annealed for 1000 seconds at temperatures ranging from 100˚C to 400˚C. Prior to annealing, it was observed that the sample deformed at the higher strain rate required a higher strain to reach steady state values of DRX volume fraction and DRX grain size. Furthermore, the higher strain rate resulted in lower steady state values for DRX volume fraction and DRX grain size, but higher room temperature hardness. It was evident that the grain size exhibited no change at lower annealing temperatures, but experienced rapid growth at an intermediate temperature, and slower growth continued at higher temperature. It was also observed that the temperature range of rapid growth was delayed in the sample deformed at the lower strain rate; the trend can be seen in Figure 2-15. Despite the large changes observed in the microstructure, the texture of the samples remained largely unchanged after annealing, as shown in Figure 2-16.

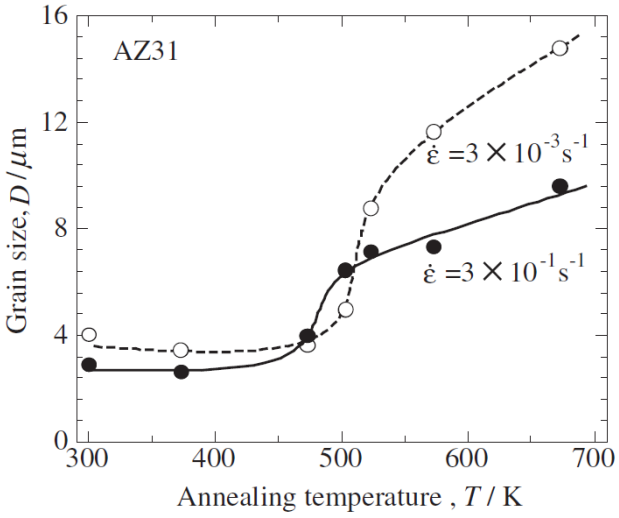

Figure 2-15: Grain size evolution with increasing annealing temperature [32].

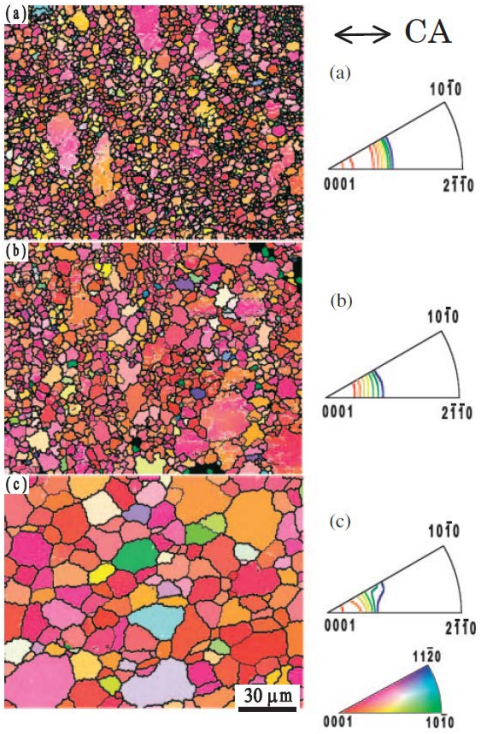

Figure 2-16: OIM images at a strain of 1.2, a) after deformation at 400˚C and 3 x $10^{-1}s^{-1}$, b) after annealing at 200˚C, c) after annealing at 400˚C for 1000 seconds [32].

To further the knowledge obtained from the isochronal study of 2005, Yang et al. [33] conducted an isothermal annealing study in 2010. After deformation, annealing was conducted at temperatures of 220˚C, 230˚C and 240˚C for times ranging from 10^2 to 10^5 seconds. The average grain sizes for various annealing conditions are shown in Figure 2-17. It was evident that grain coarsening occurred sooner for higher annealing temperatures. It was clear that the average grain size experienced minimal changes for annealing times below $7x10^2$ seconds (i.e. region 1), but rapid growth followed (i.e. region 2), and slowed beyond $7x10^4$ seconds (i.e. region 3). Furthermore, the final grain size obtained after annealing for long periods was almost identical for all annealing temperatures. Although the deformation texture remained largely unchanged after long annealing times, it was observed that the average misorientation angle had shifted slightly from 36˚ to 41.1˚.

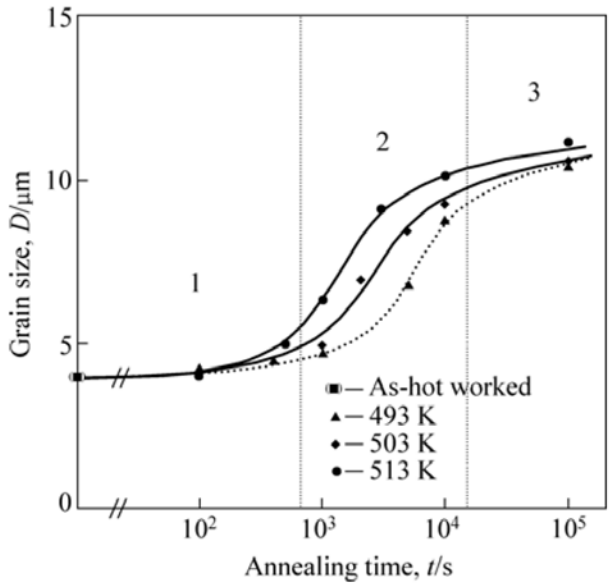

Figure 2-17: Grain size evolution with increasing annealing time [33].

2.8 Processing Maps and their Applications

When a workpiece undergoes bulk deformation, time is considered an independent variable, and the key parameter is the rate of energy input into the dynamic system. All of the power inputted is converted to heat and energy relating to microstructural changes. A processing map is commonly used to help determine deformation conditions that yield stable microstructures. A processing map consists of two maps superimposed over one another: a power dissipation map, and an instability map. In general, the working temperature is plotted on the horizontal axis and the logarithmic strain rate on the vertical axis, with contours of constant power dissipation efficiency, and distinct regions of flow instability [34]. Processing maps have been used for a wide range of alloys, examples of these can be found in the literature [34, 35]. Furthermore, Prasad and Rao have since applied the concept of processing maps to AZ31 with various starting conditions: hot extruded [36], hot rolled [20], cast [22], and cast-homogenized [21, 22]. An example of a processing map for high-temperature extruded AZ31 is provided in Figure 2-18.

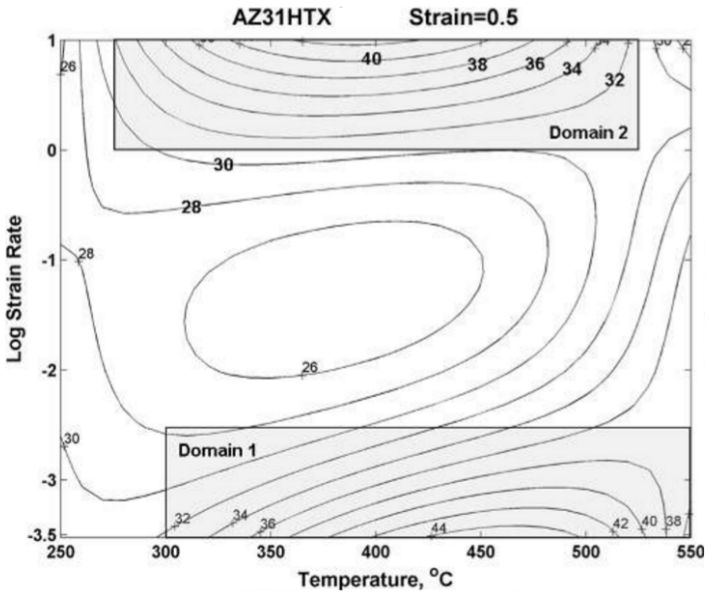

Figure 2-18: Processing map for hot extruded AZ31 at a strain of 0.5 [36].

Microstructural mechanisms that operate under specific hot working conditions are reflected in the processing map as high efficiency regions and instability regions. Processing maps utilize principles from the continuum mechanics of large plastic flow, deterministic chaos, and irreversible thermodynamics [35]. Under hot deformation conditions, it has been shown that the power dissipated is proportional to the rate of entropy generation. Since bulk deformation is irreversible, the production of entropy is consisted of two parts: conduction entropy from the transfer of heat within the workpiece, and microstructural dissipation. It has been shown that the partitioning of power dissipation between the two is controlled by the strain rate sensitivity, m [34]. By examining the flow stress curves obtained from hot compression tests, the strain rate sensitivity can be determined for a specific temperature and strain rate condition as shown in equation (1) [34]:

$$m = \left[\frac{\Delta log\bar{\sigma}}{\Delta log\dot{\bar{\varepsilon}}}\right]_{\varepsilon,T} \qquad (1)$$

where $\bar{\sigma}$ is the effective stress at the specific strain of interest and $\dot{\bar{\varepsilon}}$ is the effective strain rate. Although controversial, the power dissipation efficiency parameter introduced by Prasad [34] will be outlined briefly in this review. The dissipation efficiency is defined, for a temperature and strain rate condition, as the power that results in microstructural changes as a ratio of the

theoretical maximum possible dissipation through changes in the microstructure (i.e. m = 1) [34]. With knowledge of the strain rate sensitivity, the efficiency of power dissipation can be determined using equation (2) [35]:

$$\eta = \frac{2m}{m+1} \quad (2)$$

The power dissipation map can be plotted once the efficiencies for all deformation conditions have been determined. The plot consists of iso-efficiency contours and it has been observed that the power dissipation maps obtained at different strains are very similar. Regimes of high power dissipation efficiency reflect the operation of microstructural mechanisms; however metallurgical examination of water quenched samples is required to identify each specific mechanism. Examples of mechanisms that operate in high efficiency domains include DRX, superplasticity/wedge cracking and ductile fracture. In addition to the identification of high efficiency working domains, the processing map can be used to determine regimes of flow instability. Examples of flow instabilities include kink bands, adiabatic shear bands, Lüders bands, and flow localization [34]. The criterion for flow instability is based on the dynamic materials model and is defined by equation (3) [35]:

$$\xi(\dot{\varepsilon}) = \frac{\partial \ln\left[\frac{m}{m+1}\right]}{\partial \ln(\dot{\varepsilon})} + m \leq 0 \quad (3)$$

Although the above instability criterion has been applied to many applications, it is evident that the instability parameter cannot be computed for cases where m is negative. Furthermore, Babu et al. [37] observed that the efficiency parameter defined by Prasad [34] is only valid if the material flow stress behaviour can be modelled using the constitutive equation $\sigma = K\dot{\varepsilon}^m$, where K and m are constants for a given strain and temperature. However for complex alloy systems, the strain rate sensitivity parameter varies with strain rate. Therefore Babu et al. [37] proposed an alternate method for the determination of instability regimes in magnesium alloys:

$$\frac{\partial m}{\partial \ln(\dot{\varepsilon})} + m^2 \leq 0 \quad (4)$$

The modified instability criterion has been verified using data for various magnesium alloys, and the observed instabilities were closely predicted [37].

3.0 Experimental Methodology

3.1 Hot Compression Testing

3.1.1 Compression Specimens

To investigate the deformation behaviour of AZ31B, commercially available Ø63.5mm (Ø2.5”) extruded rods and Ø304.8mm (Ø12”) cast ingots were purchased from Magnesium Elektron. Cylindrical compression samples (Ø10mm by 15mm) were machined from both materials. To examine the anisotropy in the extruded material, two orientations in the extruded rod were investigated. Compression samples were extracted from an offset radial position in the rod, as well as along the centerline. Samples with the compression axis oriented parallel to the extrusion direction were termed ED (i.e. extrusion direction), and samples oriented along the radial direction were termed TD (i.e. transverse direction). The sample orientations and locations are shown schematically in Figure 3-1.

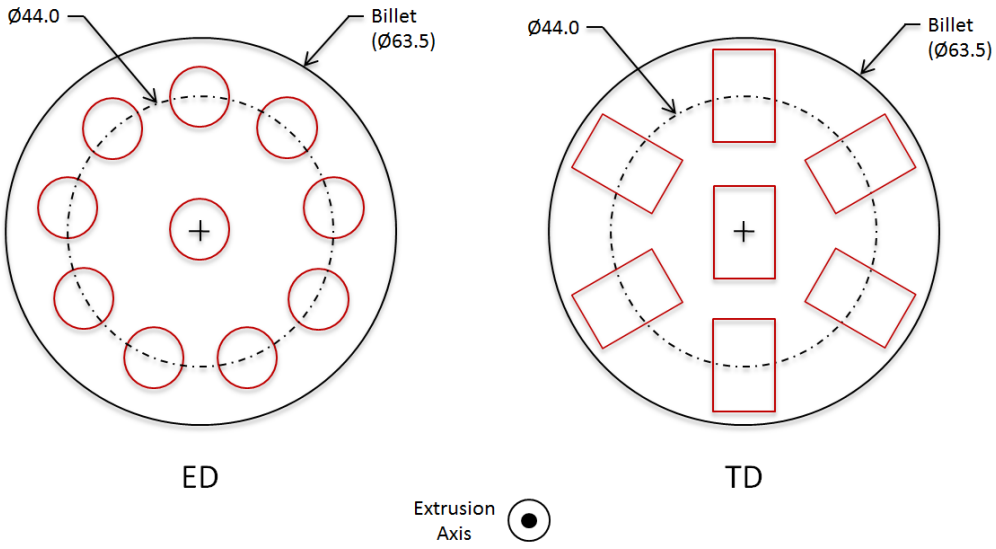

Figure 3-1: Orientation of ED and TD compression samples.

Furthermore, compression samples were extracted from the as-cast billet at various radial positions; the compression axis was oriented parallel to the casting direction for all cases. The specific locations of the samples are shown in Figure 3-9, with each ring offset by 15mm. To

avoid edge and centreline defects that may have resulted from casting, the compression samples were taken from rings 7 and 8 of the ingot. A full set of engineering drawings for the compression samples is provided in Appendix A.

3.1.2 Uniaxial Compression – Gleeble 3500®

As outlined previously, isothermal uniaxial compression tests were conducted in the temperature range from 300°C to 500°C, at constant true strain rates of $10^{-3}s^{-1}$ to $1.0s^{-1}$, and the samples were water quenched immediately to preserve the microstructure. All tests were performed using a Gleeble 3500® thermal-mechanical simulator with an air atmosphere. A type K (i.e. chromel-alumel) thermocouple was welded to the axial centre of each sample to complete the closed-loop temperature control system. Prior to placing the sample between the two compression anvils, a nickel-graphite-based lubricant (i.e. Thred Gard® High Temperature Anti-Seize) was applied to the two ends of each sample to minimize the friction at the contact surfaces. An image of the setup is shown in Figure 3-2; the sample is highlighted in the centre of the image. As a reference, the room temperature stress-strain curves obtained for both the extruded and cast materials can be found in Appendix B.

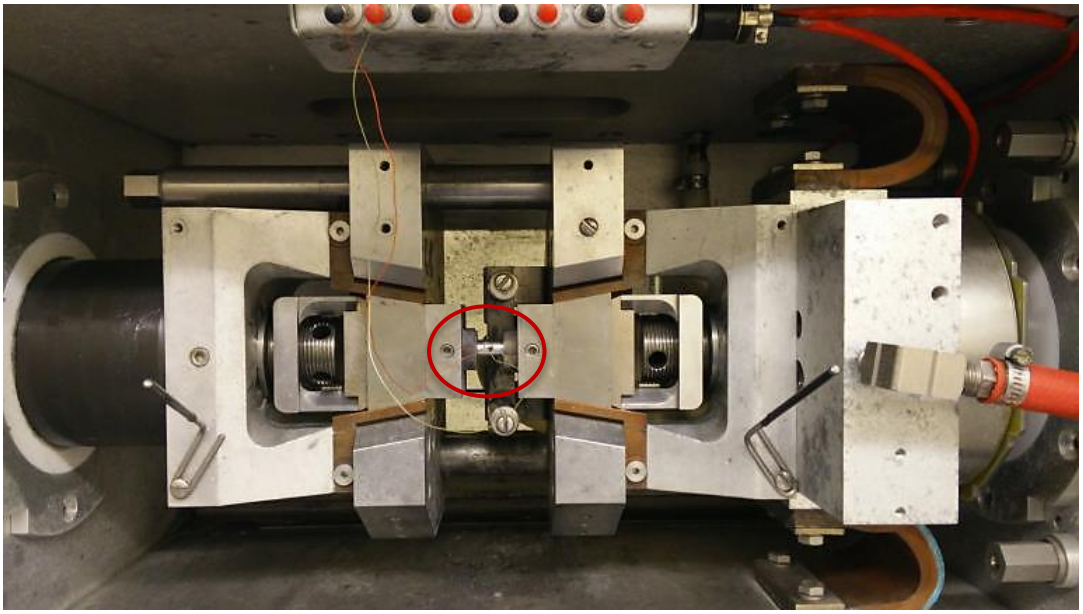

Figure 3-2: Instrument setup for uniaxial compression test.

Each sample was resistively heated to the specified testing temperature at a rate of 10°C per second, and held for five seconds to ensure uniform temperature distribution throughout. As a

calibration, a compression sample instrumented with three thermocouples was heated to 450°C before each set of tests. A thermocouple in the centre was utilized for temperature control, with two additional thermocouples, one close to each end face, for local temperature measurements. A typical experimentally measured heating profile is provided in Figure 3-3. It is evident that the heating rate is very linear and the samples reach uniform temperature within five seconds.

In addition to the temperature, the strain rate is an important parameter for which accurate control is crucial. In Figure 3-4, the true strain is plotted against the time fraction to test completion (i.e. to a true strain of 0.5) for various strain rates. It is evident that a constant true strain rate can be maintained for lower strain rates (i.e. $10^{-3}s^{-1}$ and $10^{-2}s^{-1}$). However at the higher strain rates, particularly at a strain rate of $1.0s^{-1}$, acceleration and deceleration effects of the hydraulic ram are evident. Despite the ram effects, a minimum average strain rate of $0.8s^{-1}$ can be achieved with lower strain tests (i.e. final true strain of 0.5), and average strain rates very close to $1.0s^{-1}$ can be achieved with higher strain tests (i.e. final true strain of 1.0). These effects were seen in the flow stress curves obtained for high strain rate tests, where a rapid drop in measured force was observed in the final 10% true strain of each test as the ram decelerated. To circumvent the issue, flow stress values for intermediate strains were extracted from compression data obtained from high strain tests.

The stress-strain curves outputted by the Gleeble® were automatically determined using standard true stress and true strain equations (i.e. assumed no friction or temperature rise). However, to obtain representative curves, the effects of friction at the contact surfaces and adiabatic temperature rise during deformation had to be accounted for. From the load and displacement data obtained from the Gleeble®, corrected stress-strain curves were produced using the procedure outlined by Luan et al. [38]. The correction only required knowledge of the sample geometry after deformation and instantaneous temperatures throughout the compression test. In general, the correction for friction lowered the observed flow stress. However the procedure had been developed for isotropic material flow. Therefore, for samples with non-circular cross-sections after deformation, the stress-strain curves presented in this research were only corrected using standard true stress and true strain equations. It was observed that friction had a significant impact on the observed flow stress beyond a true strain of 0.6. Therefore, many of the compression tests were conducted to a final true strain of 0.5.

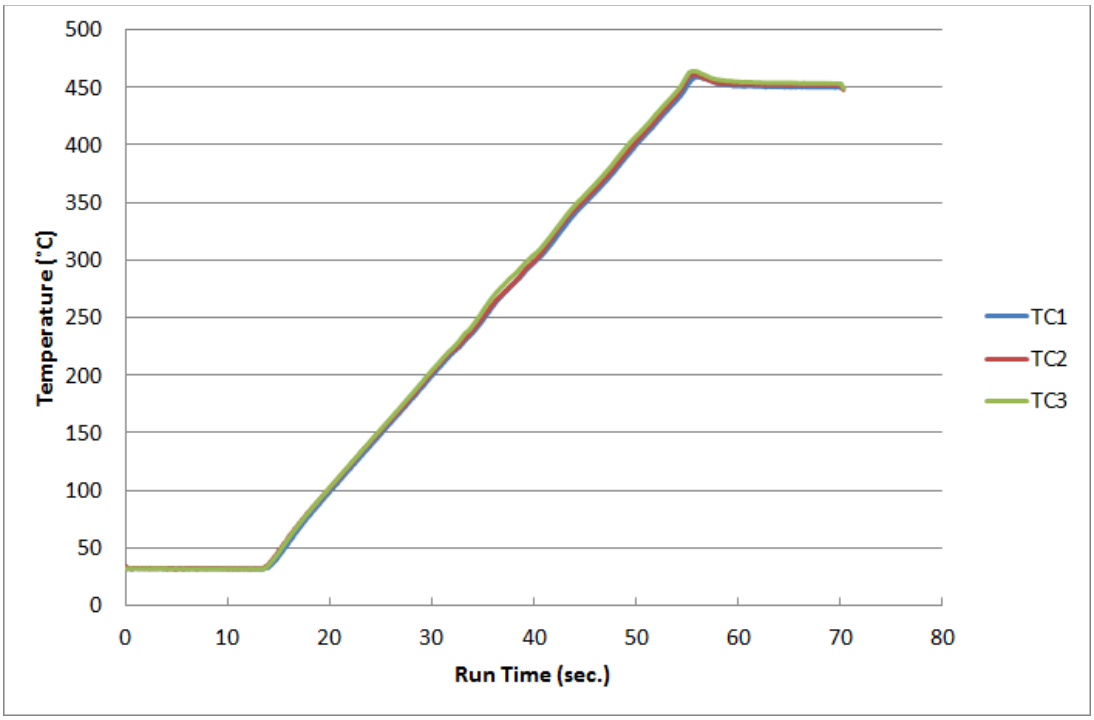

Figure 3-3: Heating profile up to 450°C on Gleeble 3500® (Control – TC2).

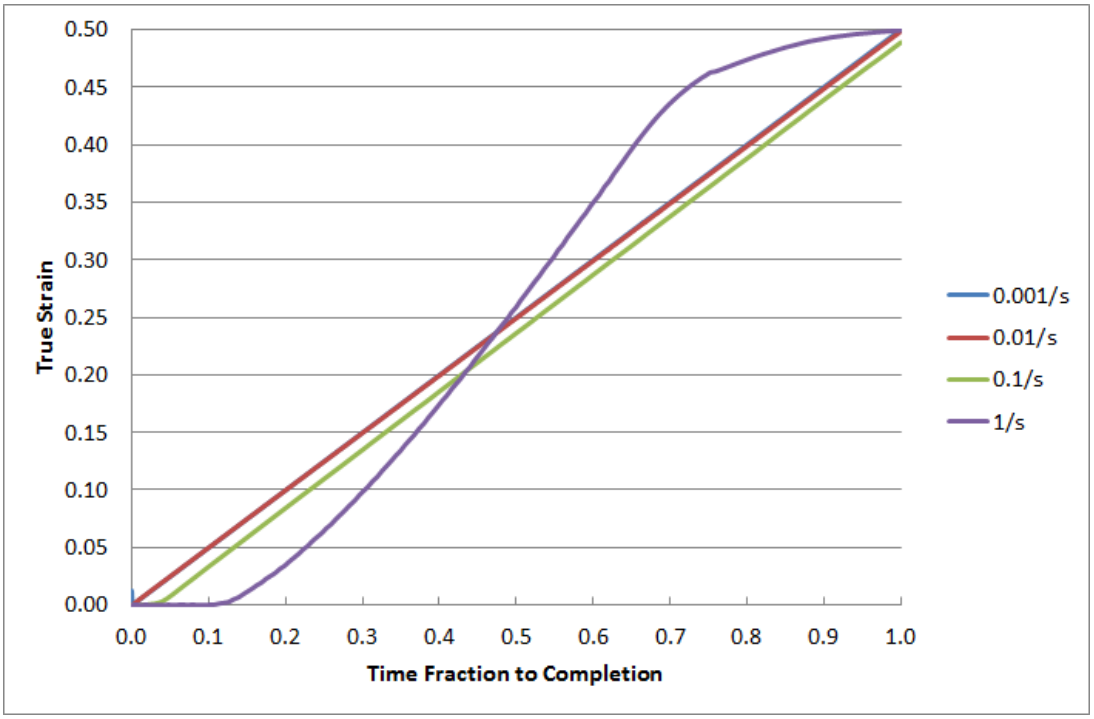

Figure 3-4: Strain rate control on Gleeble 3500® for a test to 0.5 true strain.

3.2 Material Characterization

3.2.1 Extruded Condition

To characterize the initial material, inductively coupled plasma optical emission spectrometry (ICP-OES) was employed to determine the chemical composition of the compression sample. One sample from each orientation, at the offset location, of the extruded rod was analyzed. Each sample was completely dissolved in a solution of 37% hydrochloric acid prior to analysis. The results for ED and TD are shown in Figure 3-5 and Figure 3-6, respectively.

From the ICP-OES results, it was evident that the aluminum, zinc and manganese contents in the compression sample were higher than the nominal compositions of 3.0%, 1.0% and 0.2%, respectively. The initial microstructure for the extruded rod is shown in Figure 3-7; the procedure for metallography will be discussed in a subsequent section. It was evident that the material consisted of fine, equiaxed grains at the centre, with coarser grains in the mid-section, and a large number of twins just below the surface. The average grain size at the centreline was 12.1µm, but increased to 54.9µm for the offset compression samples. Without knowledge of the material processing history from the manufacturer, it was not possible to determine the exact reason for the microstructural variation.

In addition to the microstructure, the macrotexture of the extruded rod was measured using a Bruker D8 Discover x-ray diffraction system (XRD). The pole figures are shown in Figure 3-8; it was evident that the axisymmetric fiber texture commonly observed in extrusions was present. However, the peak intensities were shifted slightly compared to the theoretical texture. The differences may be attributed to local variations in texture, or slight deviations between the plane of examination and the perceived plane of interest.

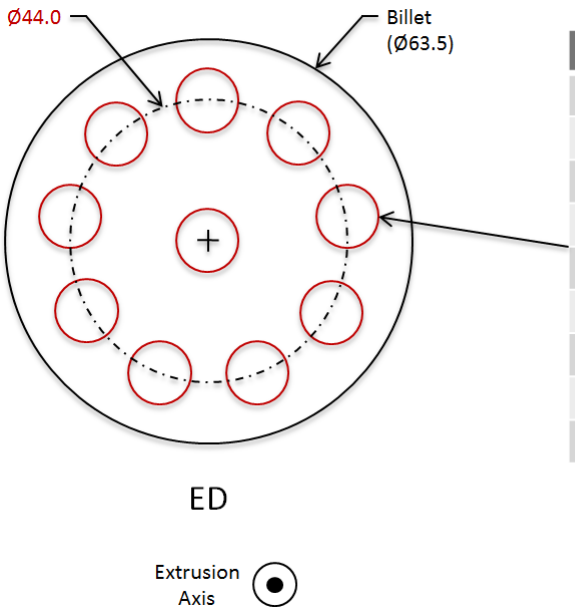

Element	Wt %
Mg	94.189
Al	3.805
Zn	1.275
Mn	0.701
Fe	0.006
Ca	0.006
Cu	0.001
Ni	0.002
Si	0.014

Figure 3-5: Chemical composition of ED specimen obtained via ICP-OES.

Element	Wt %
Mg	94.188
Al	3.813
Zn	1.276
Mn	0.700
Fe	0.005
Ca	0.003
Cu	0.001
Ni	0.002
Si	0.014

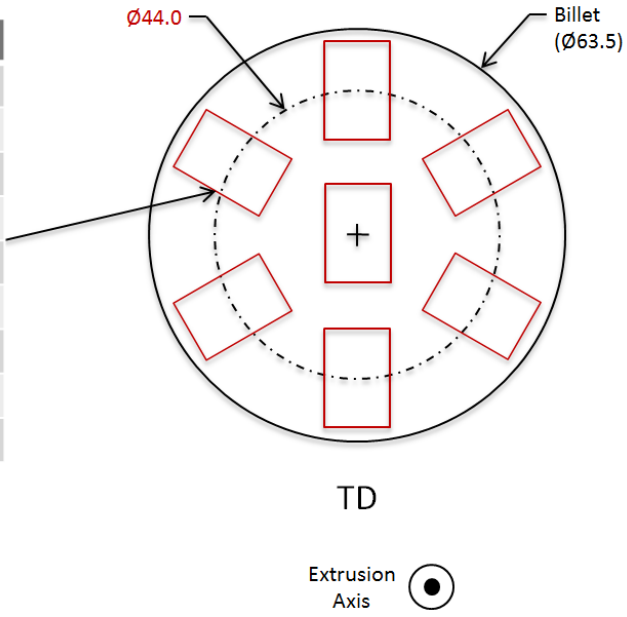

Figure 3-6: Chemical composition of TD specimen obtained via ICP-OES.

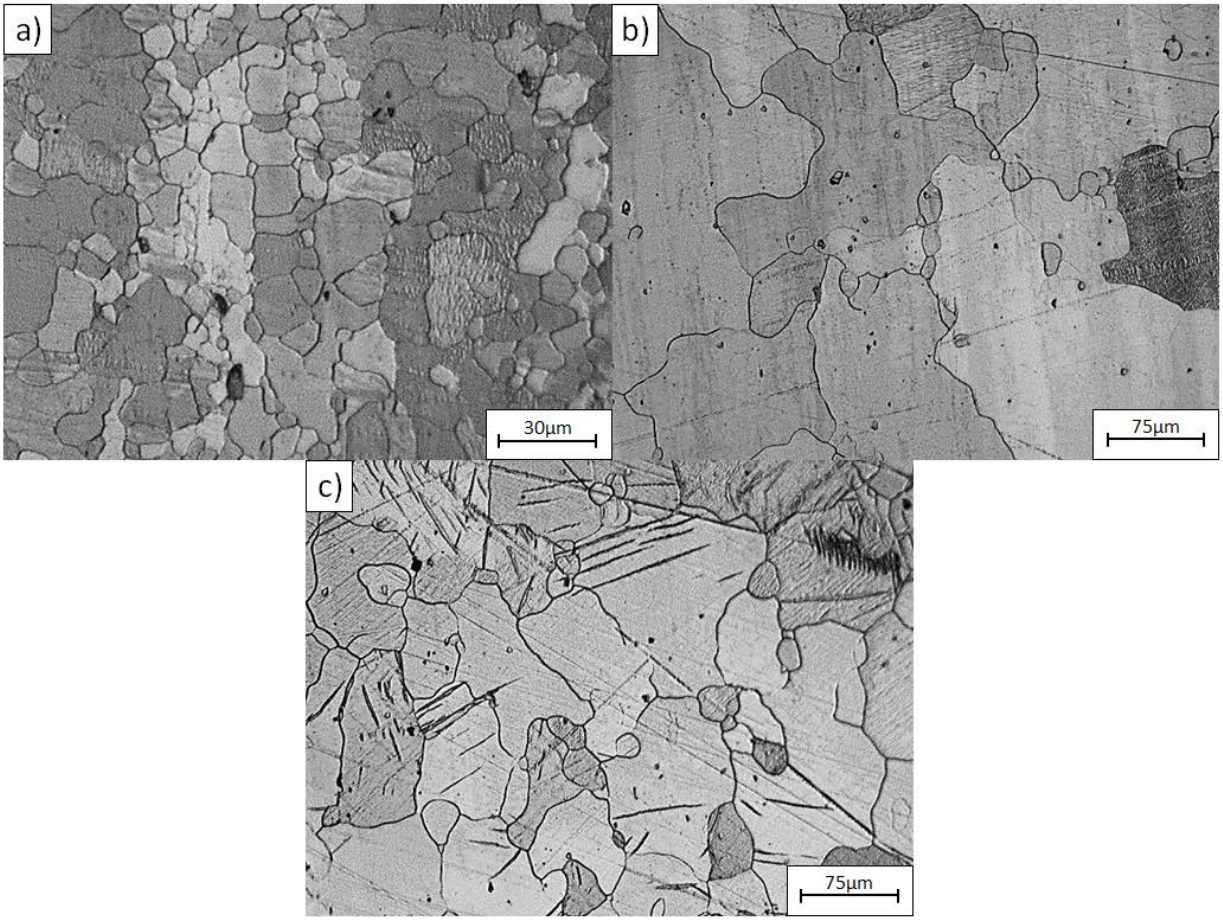

Figure 3-7: Initial microstructure of extruded rod at various locations: a) centreline b) 20mm from the centreline c) near surface (extrusion axis aligned vertically).

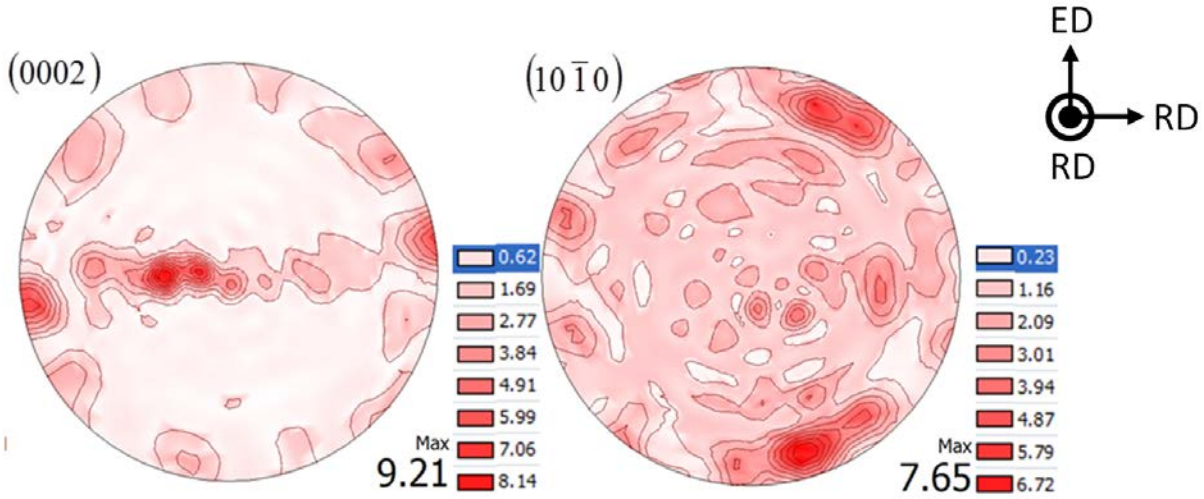

Figure 3-8: XRD pole figures for initial texture in extruded rod.

3.2.2 As-Cast and Cast-Homogenized Conditions

As outlined previously, compression samples were extracted from various locations in the cast ingot. The chemical compositions obtained from rings 4 and 7 with ICP-OES are shown in Figure 3-9. It was evident that the solute content was higher towards the surface of the ingot; the inverse segregation observed is common for magnesium DC castings [39]. In addition, the random initial texture observed in the as-cast ingot is shown in Figure 3-10. Homogenization heat treatments were conducted in a Thermo Scientific Lindberg Blue M furnace with an air atmosphere. The furnace was allowed to heat up to temperature before the samples were placed inside. A control sample instrumented with a thermocouple was also placed in the furnace to provide local temperature verification. An image showing the homogenization procedure is provided in Figure 3-11.

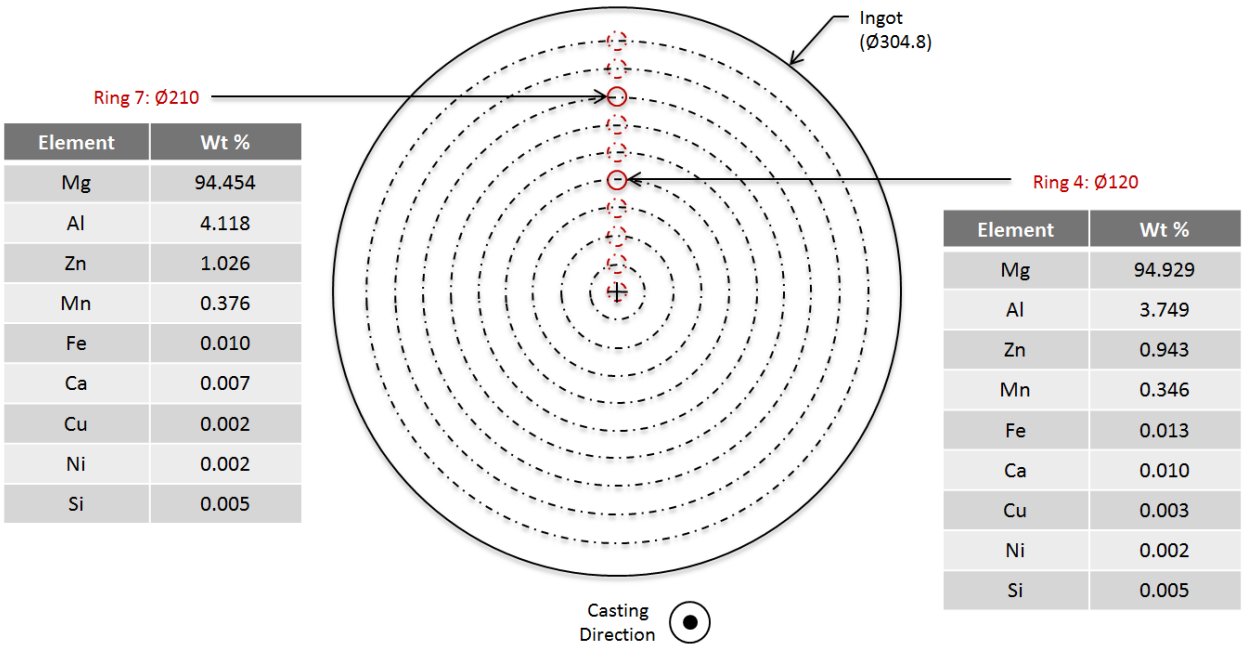

Element	Wt %
Mg	94.454
Al	4.118
Zn	1.026
Mn	0.376
Fe	0.010
Ca	0.007
Cu	0.002
Ni	0.002
Si	0.005

Element	Wt %
Mg	94.929
Al	3.749
Zn	0.943
Mn	0.346
Fe	0.013
Ca	0.010
Cu	0.003
Ni	0.002
Si	0.005

Figure 3-9: Chemical composition at two locations in the cast ingot obtained via ICP-OES.

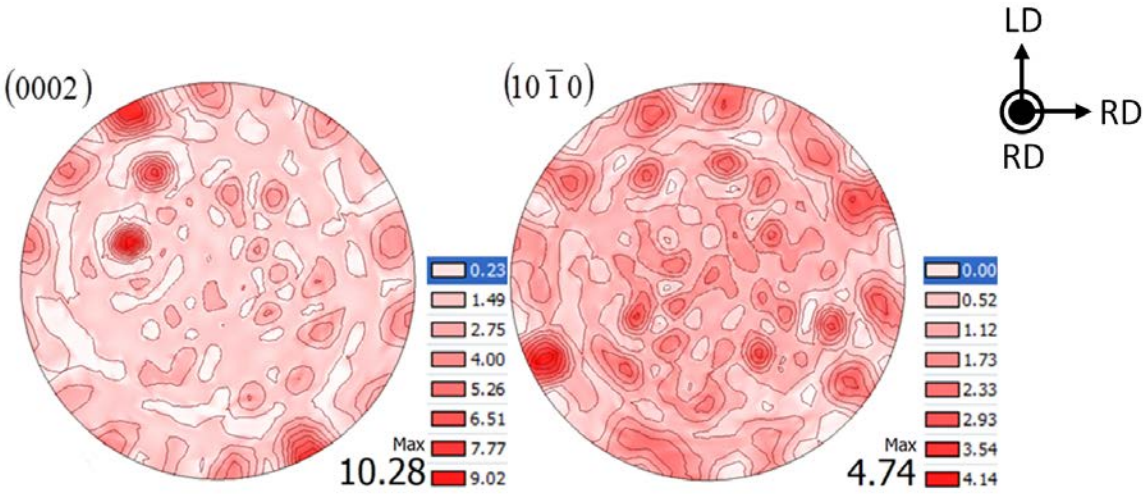

Figure 3-10: XRD pole figures for initial texture in as-cast ingot.

Homogenization was conducted at 450°C for five hours, and the samples were subsequently furnace cooled. However, it should be mentioned that samples which had been air cooled exhibited very similar microstructures and compression behaviours to their furnace cooled counterparts. The microstructures before and after homogenization are shown in Figure 3-12. The dendritic structure was clearly visible in the as-cast condition but was no longer visible after homogenization. It was evident that the heat treatment had allowed sufficient time for diffusion to occur and had minimized microsegregation in the compression sample.

Figure 3-11: Temperature calibration for homogenization procedure.

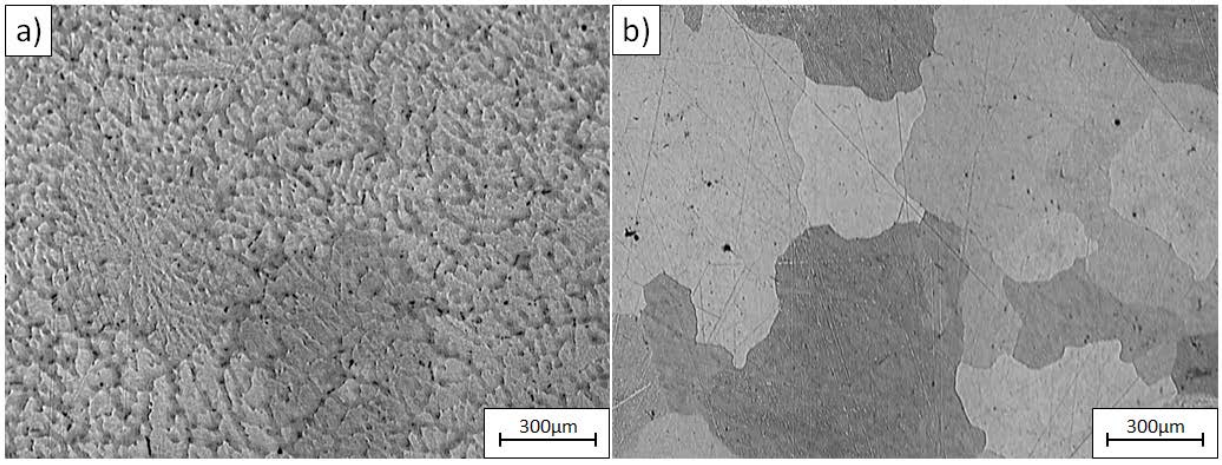

Figure 3-12: Microstructures of a) as-cast and b) cast-homogenized conditions.

3.3 Optical Microscopy

3.3.1 Metallography

To examine the microstructures prior to or after deformation, the compression samples were sectioned along the compression axis at the midplane. To protect the microstructures from heat and pressure associated with hot mounting, samples were cold mounted in epoxy. Grinding on progressively finer grits of silicon carbide grinding paper, down to 2400 grit, was followed by polishing with using 3µm, 1µm and 0.25µm diamond solutions. Surfaces for microstructural examination were subsequently etched using a solution of 4.2g picric acid, 10mL acetic acid, 10mL water, and 70mL ethanol. The full sample preparation procedure is outlined in Appendix C. Optical images of the microstructure were taken with an Olympus BH2-UMA optical microscope, at magnifications ranging from 50x to 500x.

3.3.2 Grain Size Analysis

Micrographs obtained via optical microscopy were analyzed using image processing software ImageJ [40], from which grain statistics could be computed. Due to slight surface imperfections from polishing, the software was unable to automatically detect all of the grain boundaries directly from the micrographs. As a result, the 200x micrographs were traced onto transparent sheets, and scanned to produce a black and white image for analysis. An example of the

procedure is provided in Figure 3-13. With knowledge of the scale and resolution of the original micrograph, the area of each individual partition obtained via the image analysis algorithm could be easily converted to grain areas. Parameters such as the number of grains, the average grain area and the grain area distribution were extracted from the data.

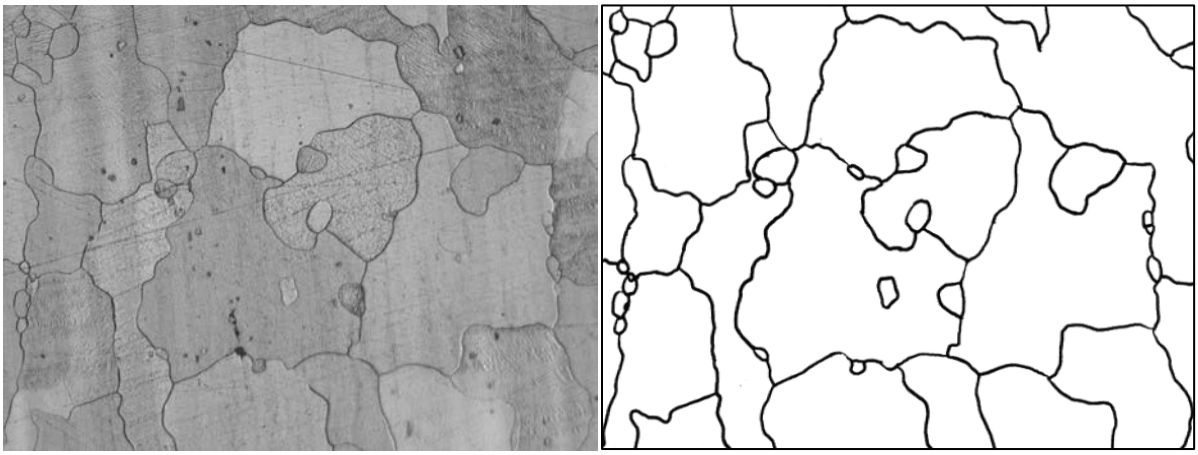

Figure 3-13: Images for grain size analysis, original micrograph - left, traced image – right.

3.4 Differential Scanning Calorimetry

Differential scanning calorimetry (DSC) was utilized to investigate thermal events occurring within the samples prior to and post homogenization. DSC measures the energy input required by the system to maintain a specified heating rate in the sample. An empty Al_2O_3 crucible was first heated to the specified temperature, in a controlled environment which had been purged with argon, and cooled to obtain the baseline energy input for an empty crucible. A small disc (Ø5mm by 3mm) of the material was then placed into the same crucible and heated under the same conditions; energy inputs that deviated from the baseline were automatically computed. Since changes in the microstructure are either endothermic or exothermic, the amount of energy input by the system will vary for the temperature range in which a thermal event is occurring. For the current study, the heating rate was 10°C per minute for all tests. A temperature and sensitivity calibrated Netzsch 404 C Pegasus® DSC was employed to investigate the thermal events occurring in the as-received materials, and also after homogenization.

4.0 Results and Discussion

4.1 Anisotropic Plastic Behaviour

4.1.1 Extrusion Direction

The offset ED samples which had undergone uniaxial compression tests to a final true strain of 0.5 exhibited varying degrees of anisotropy. It was observed that samples deformed at 300°C and the two highest strain rates (i.e. $10^{-1}s^{-1}$ and $1.0s^{-1}$) exhibited fractures oriented approximately 45° to the compression axis, which corresponded to the direction of maximum shear stress. Images showing the top-view cross-sections of the ED samples are shown in Figure 4-1. It was evident the samples deformed at the lowest strain rate of $10^{-3}s^{-1}$ exhibited almost circular cross-sections, and elliptical cross-sections were observed for all other deformation conditions. Furthermore, the extent of anisotropy was observed to increase with strain rate.

To quantify the anisotropy associated with each deformed sample, the maximum minor axis (D_{min}) and major axis dimensions (D_{maj}) were measured and the ratio of the two dimensions (D_{min}/D_{maj}) was determined. A ratio of 1.0 represented a circular cross-section resulting from symmetric material flow, and a deviation from that would have reflected an elliptical cross-section. It was observed that repetitions of randomly selected deformation conditions exhibited very consistent external dimensions. The minor to major axis ratios measured from the samples are shown in Figure 4-2. It was evident from the results that the degree of anisotropy increased with deformation strain rate. Omitting the two samples which exhibited fractures, it was observed that the deformation temperature had no clear effect on the anisotropy of material flow. However, the results differed from those observed by Dai et al. [19] and Rao et al. [20], where the final geometry of the AZ31 compression/forging samples showed strong dependence on both strain rate and temperature.

Consistent with studies conducted by several other researchers [17, 18, 19], the flow stress curves obtained at low temperatures and high strain rates exhibited sigmoidal behaviour at low strains. As discussed previously, this behaviour had been attributed to the dominance of tensile twinning. The flow stress curves at 300°C and various strain rates are presented in Figure 4-3. It

was evident the die load, and hence the flow stress, decreased with strain rate and with increasing deformation temperature. The prominence of the twinning signature in high strain rate tests suggested that tensile twinning was the dominant deformation mechanism. For deformation strain rates of $10^{-1}s^{-1}$ and $1.0s^{-1}$, the twinning signature was observed up to temperatures of 350°C and 400°C, respectively. The disappearance of the twinning signature in the flow stress curves suggested a change in deformation mechanism for tests conducted at elevated temperatures. To verify the dominance of twinning, an interrupted compression test was conducted at 300°C and $1.0s^{-1}$, to a final true strain of 0.10; the corresponding microstructure is provided in Figure 4-4. Although twins were not observed in the microstructure at higher strains, it was evident the microstructure contained a large number of twins at low strain.

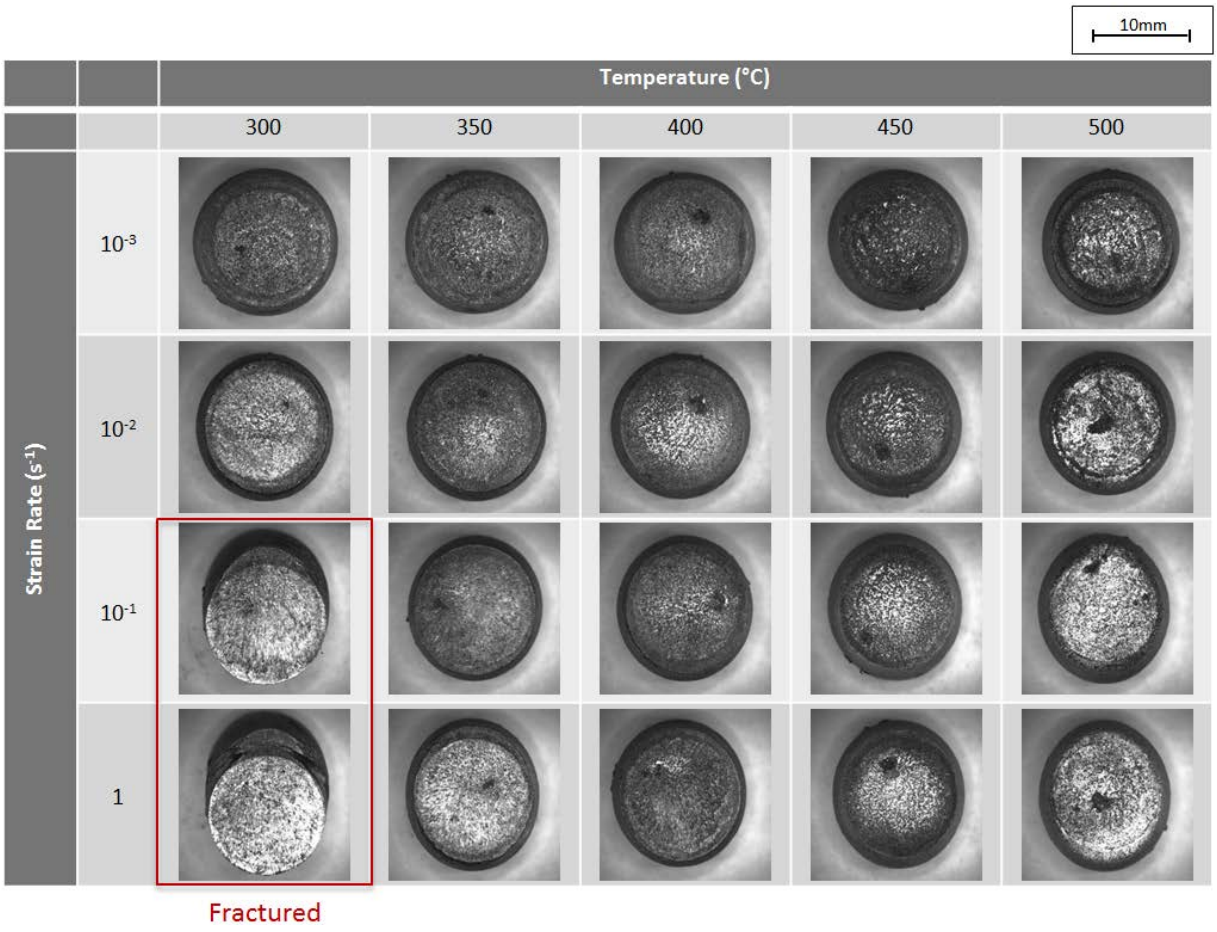

Figure 4-1: Top-view images of offset ED samples deformed to a true strain of 0.50.

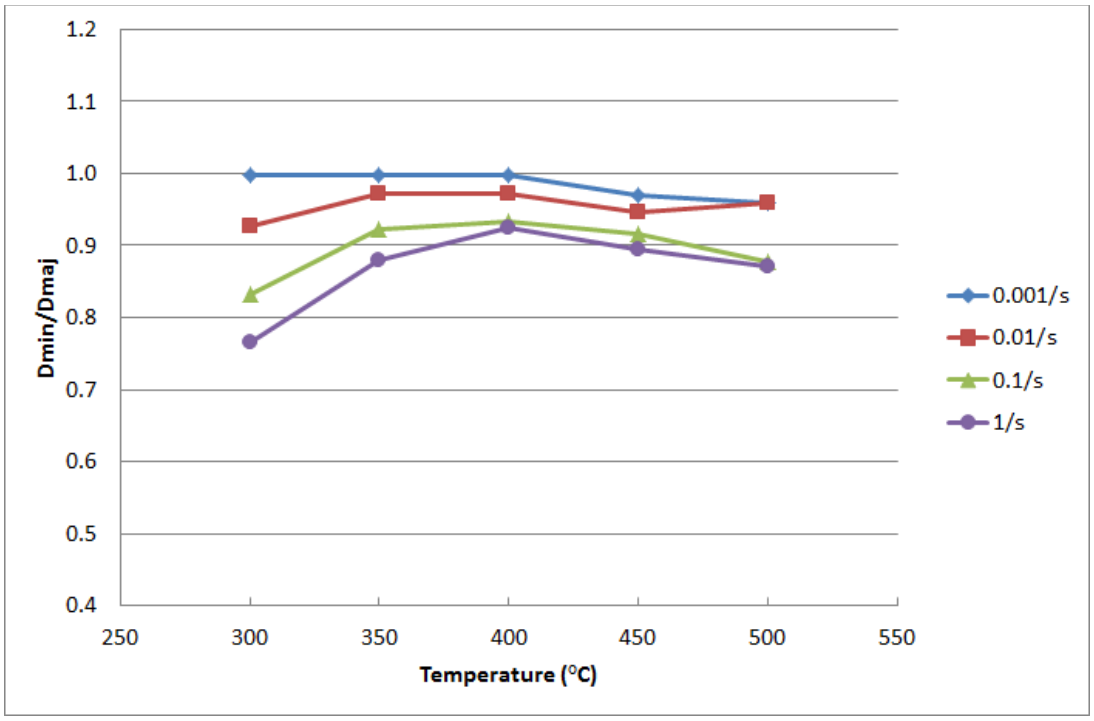

Figure 4-2: Minor to major axis ratios for offset ED samples at a true strain of 0.50, deformed under various conditions.

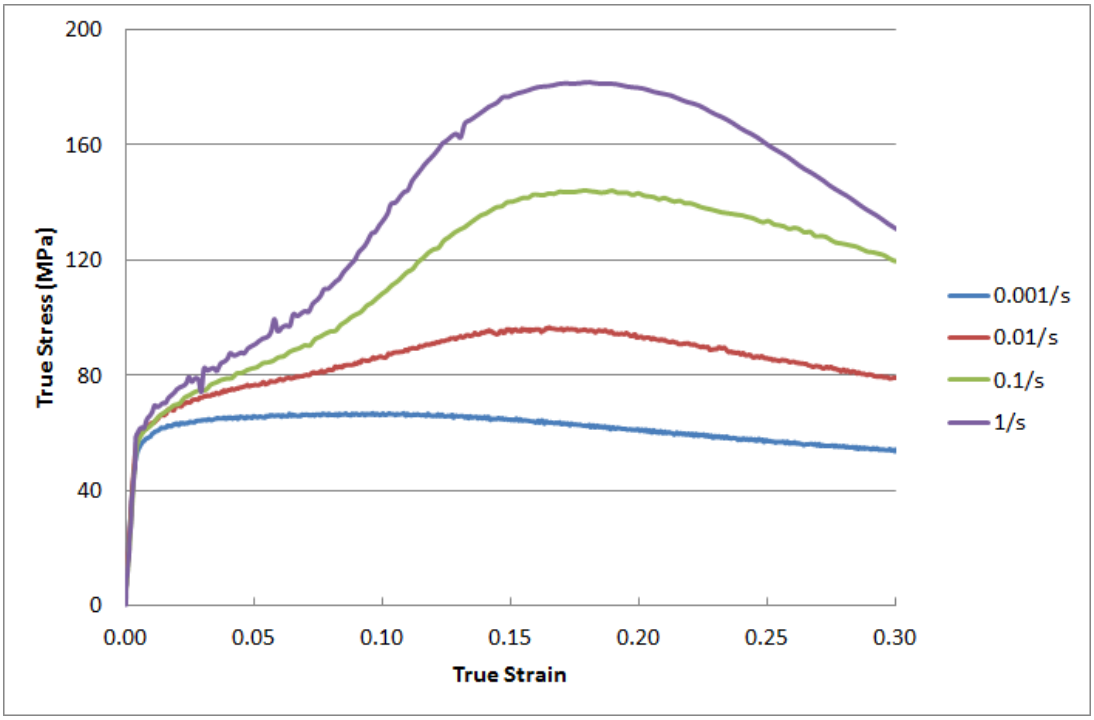

Figure 4-3: Flow stress curves for offset ED samples at 300°C and various strain rates.

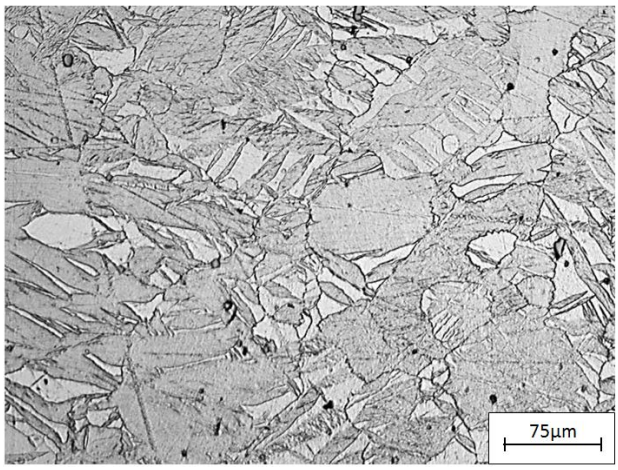

Figure 4-4: Micrograph of offset ED sample after deformation to a true strain of 0.10 at 300°C and $1.0s^{-1}$.

From the flow stress curves and supporting microstructure, it was evident that tensile twinning was an active deformation mechanism under certain deformation conditions. Recall that Lee et al. [18] attributed the anisotropy of material flow to the initial texture of the hot rolled sheet. Since the compression samples were extracted from an offset location in the extruded rod, the initial texture was not axisymmetric, as it would be along the centreline of the extrusion. The grains in the sample would have been favourably oriented such that the c-axes were aligned along one direction, perpendicular to the compression axis. Upon loading, the compressive forces were exerted onto two parallel prismatic faces of the HCP structure; the geometry favoured tensile twinning, prismatic slip and pyramidal slip. By examining the directions and planes on which tensile twinning occur, it was evident that the dominance of twinning resulted in a major strain component in the < c > direction. Furthermore, examination of the slip planes within the pyramidal systems revealed a similar result. However, the grains in the compression sample were also oriented favourably for prismatic slip, which resulted in preferential material flow in the < a > direction. To further add to the complexity, tensile twinning of the $\{10\bar{1}2\}$ type would have caused the grain to rotate almost 90° [41], and grain rotation during deformation would have produced an orientation of hard slip (i.e. resisted basal slip and prismatic slip) [28, 29, 30].

It was evident the partitioning of tensile twinning, prismatic slip and pyramidal slip played an important role in developing the final geometry after deformation. With the addition of scribe

lines on the sample end face, compression tests were conducted at 300°C, 350°C and 500°C, at a strain rate of $1.0s^{-1}$, to a final true strain of 0.5. In all cases, it was observed that the major axis of the sample coincided with the direction of the c-axes; the result was in agreement with those of Dai et al. [19]. Recall that Dai et al. [19] had proposed an acceleration of the twinning mechanism at high strain rate. Therefore, for a given strain, the activity of twins was expected to be greater under a higher strain rate. In the current study, the greater degree of anisotropy at low temperature and high strain rates was attributed to accelerated twinning activity. The relatively low twinning activity at low strain rates provided a partitioning of tensile twinning and prismatic slip which resulted in almost circular cross-sections. At higher temperatures, the accelerated grain rotation at high strain rate observed by Li et al. [28] resulted in the rapid suppression of prismatic slip at low strain, which led to the dominance of pyramidal slip and the subsequent anisotropy of flow at intermediate levels of strains. With consideration to the above finding, it was determined that the major axes of the deformed samples corresponded to the radial direction of the extruded rod, as a result of tensile twinning at low temperatures, and pyramidal slip at high temperatures. To further study the development of anisotropy, compression tests were conducted on offset ED samples to various strains; images of the samples are shown in Figure 4-5, and the final dimensions are provided in Figure 4-6.

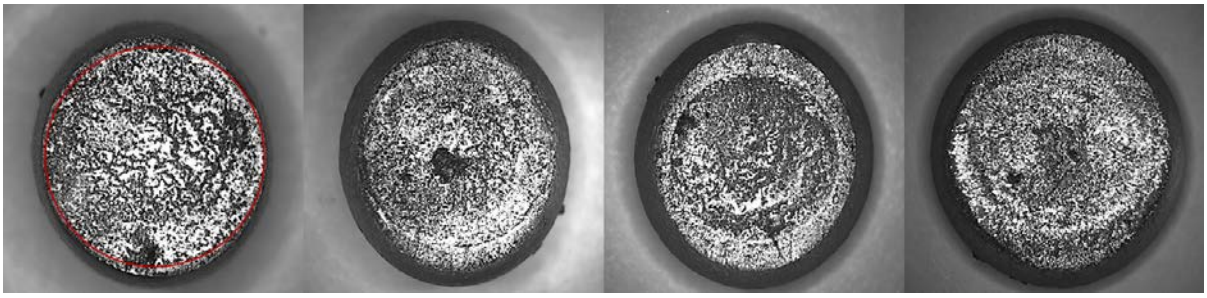

Figure 4-5: Images of offset ED samples after deformation at 500°C and $1.0s^{-1}$, to final true strains of 0.25, 0.50, 0.75, and 1.0 (from left to right – not to scale).

It was evident anisotropy began developing at low strain, and both dimensions grew steadily at intermediate levels of strains, before beginning to converge at high strain. Considering the tests were conducted at 500°C, the CRSS values required for slip on various non-basal systems were relatively low. Dai et al. [19] had not observed the presence of twins after deformation at 400°C and $1.0s^{-1}$, which suggested that tensile twinning was no longer the most favourable deformation

mechanism. Therefore, it was presumed that tensile twinning had little to no impact on the observed anisotropy at 500°C. Contrary to observations made in the current study and those by Dai et al. [19], Rao et al. [20] observed the major axis of the forged cups to be aligned perpendicular to the c-axis under all investigated conditions. The relative strength of the initial basal plane texture in each study may have played a role in the observed behaviour. Furthermore, it was observed in the current study that the major axis remained along the radial direction after deformation to a true strain of 1.0, at 500°C and $1.0s^{-1}$. As strain increased, the grains rotated to orientations of hard slip and prismatic slip was no longer favourable. Therefore it was suspected that soft slip (i.e. basal slip) that occurred during grain rotation, as well as pyramidal slip which resulted from c-axis compression after grain rotation, had restored the symmetry of material flow at high strain. Since the basal plane texture strengthens with strain, it was expected that anisotropy of flow would decrease with increasing strain.

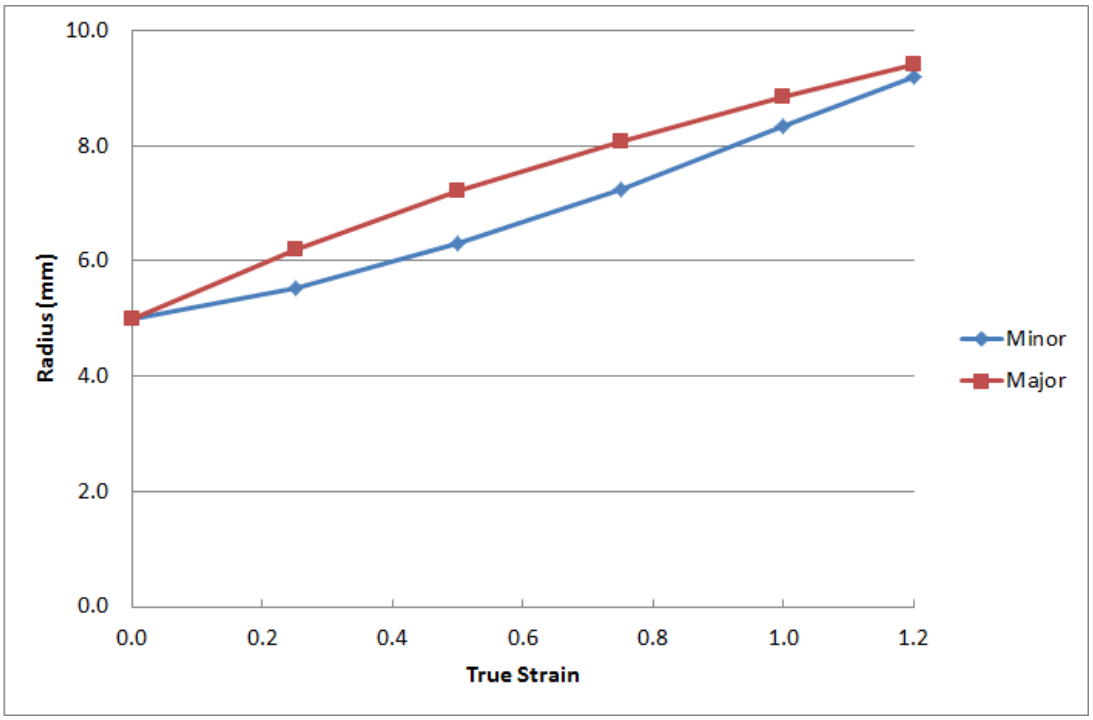

Figure 4-6: Development of anisotropy in offset ED samples deformed at 500°C and $1.0s^{-1}$, to various final true strains.

To verify that the initial texture plays a vital role in producing the final geometry, a compression test was conducted on a centreline ED sample. Given the axisymmetric fiber texture observed in

the extruded rod, the centerline samples were expected to deform symmetrically about the compression axis. The results are shown in Figure 4-7; indeed the centreline sample exhibited no anisotropy in flow behaviour, and thus the result supported the proposed role of initial texture.

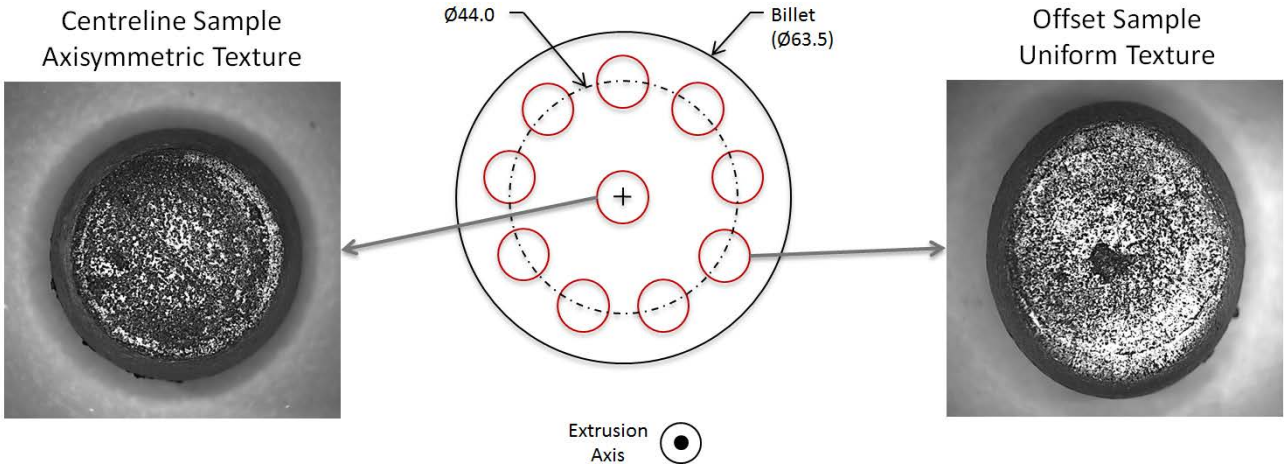

Figure 4-7: Images of centreline and offset ED samples at a true strain of 0.50 after deformation at 500°C and 1.0s^{-1}.

4.1.2 Transverse Direction

The anisotropy observed in the offset TD samples of the extruded rod differed from that in the ED samples. The final geometry observed in the TD samples showed strong dependence on deformation temperature; top-view images of the deformed samples are shown in Figure 4-8. It was evident the anisotropy of flow was significant at low deformation temperatures, but weakened with increasing temperature. Unlike the ED samples, which exhibited the least anisotropy at low strain rate, the TD samples deformed at high temperature and high strain rate exhibited the least anisotropy.

The minor to major axis ratios obtained from the samples are presented in Figure 4-9. It was evident that anisotropy was more significant at higher strain rates for deformation temperatures below 400°C; however the trend reversed beyond 400°C and anisotropy became most prominent at lower strain rates. The flow stress curves obtained from the offset TD samples at a deformation temperature of 300°C are shown in Figure 4-10. It was evident the tensile twinning signature that was observed for the ED samples was not present for the TD samples.

With consideration to the initial texture in the extruded rod, it was evident that uniaxial compression and forging tests conducted on samples along the normal direction of a hot rolled plate exhibited the same c-axis compression as in the case of a TD sample in the current study. However, the results obtained by other researchers showed little to no anisotropy under all investigated conditions [17, 18, 19, 20]. The initial texture in the TD sample was expected to resist tensile twinning, basal slip, and prismatic slip. With compression twinning and pyramidal slip being the only mechanisms oriented favourably for activation, anisotropy of flow was expected to be minimal. Additional offset TD samples, marked with scribe lines running across one of the end faces, were produced to assist in understanding the observed anisotropy. The scribe line was oriented perpendicular to the extrusion direction. Upon deformation, it was observed that the scribe line was oriented along the major axis of the elliptical cross-section. Images of the marked TD sample prior to, and after, deformation are shown in Figure 4-11.

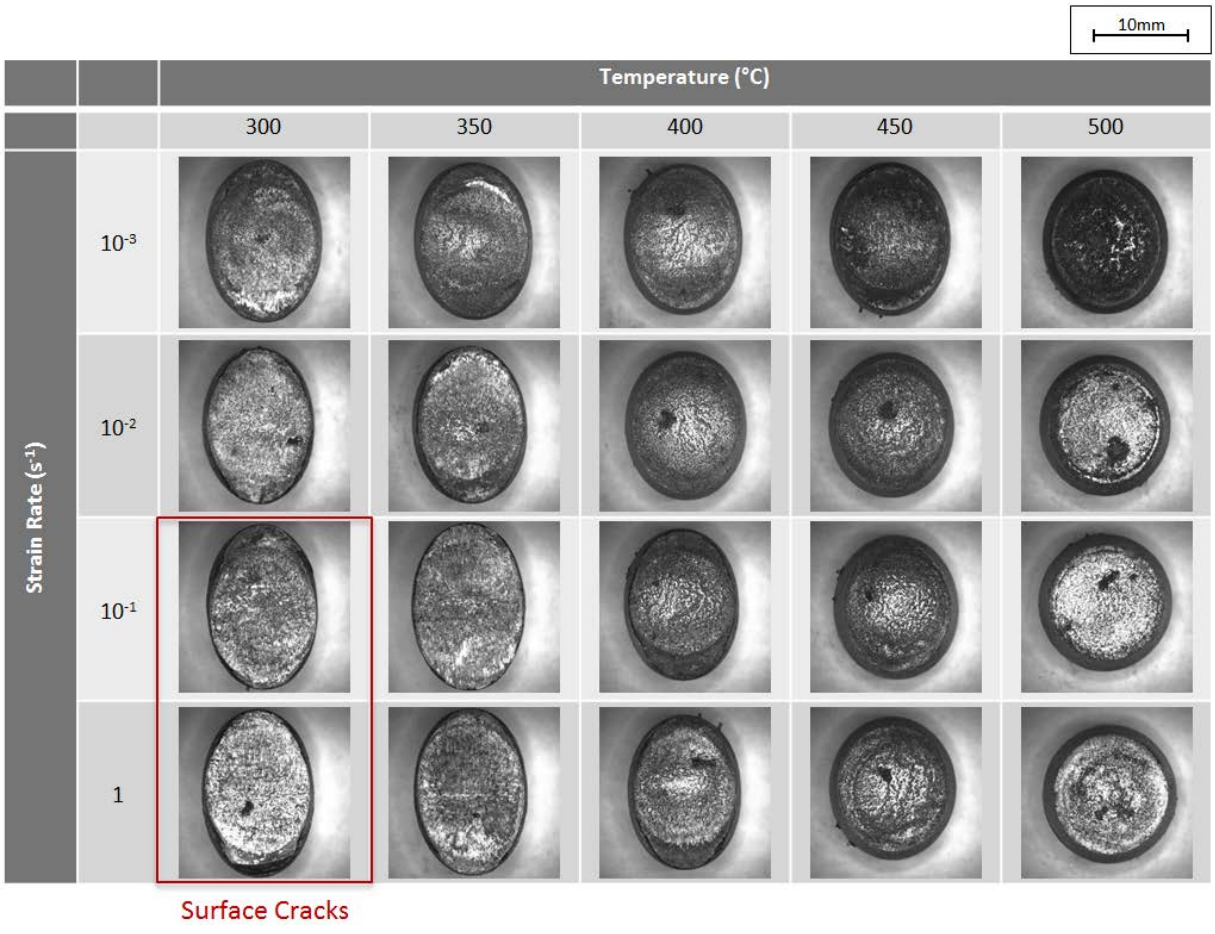

Figure 4-8: Top-view images of offset TD samples deformed to a true strain of 0.50.

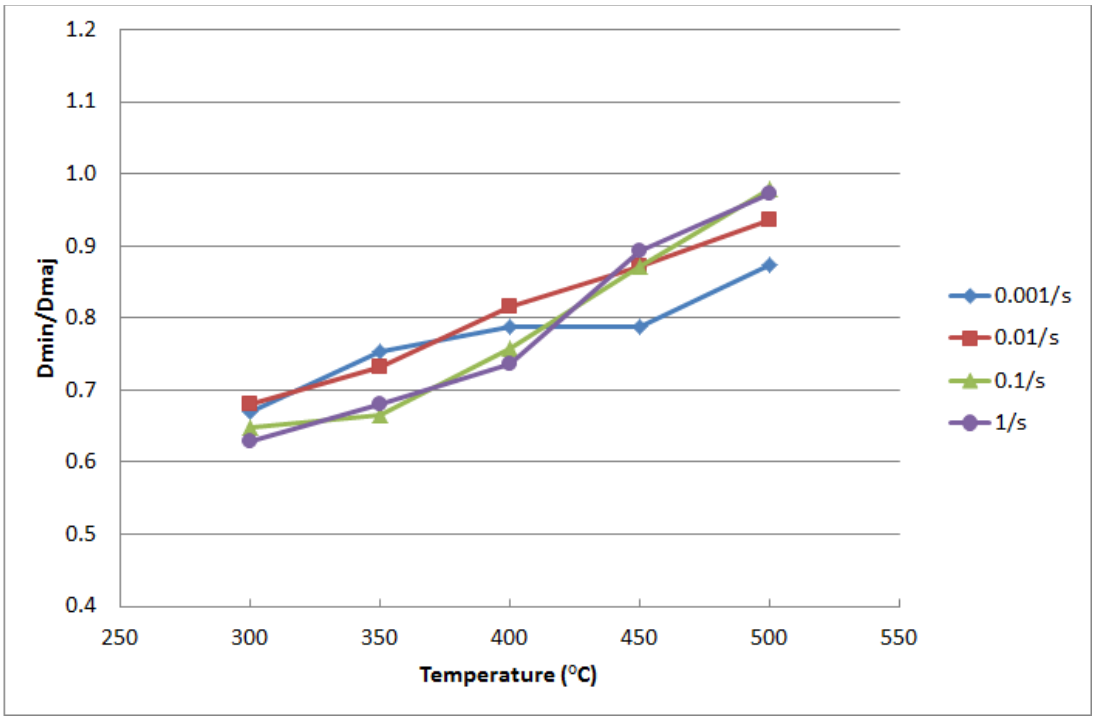

Figure 4-9: Minor to major axis ratios for offset TD samples at a true strain of 0.50, deformed under various conditions.

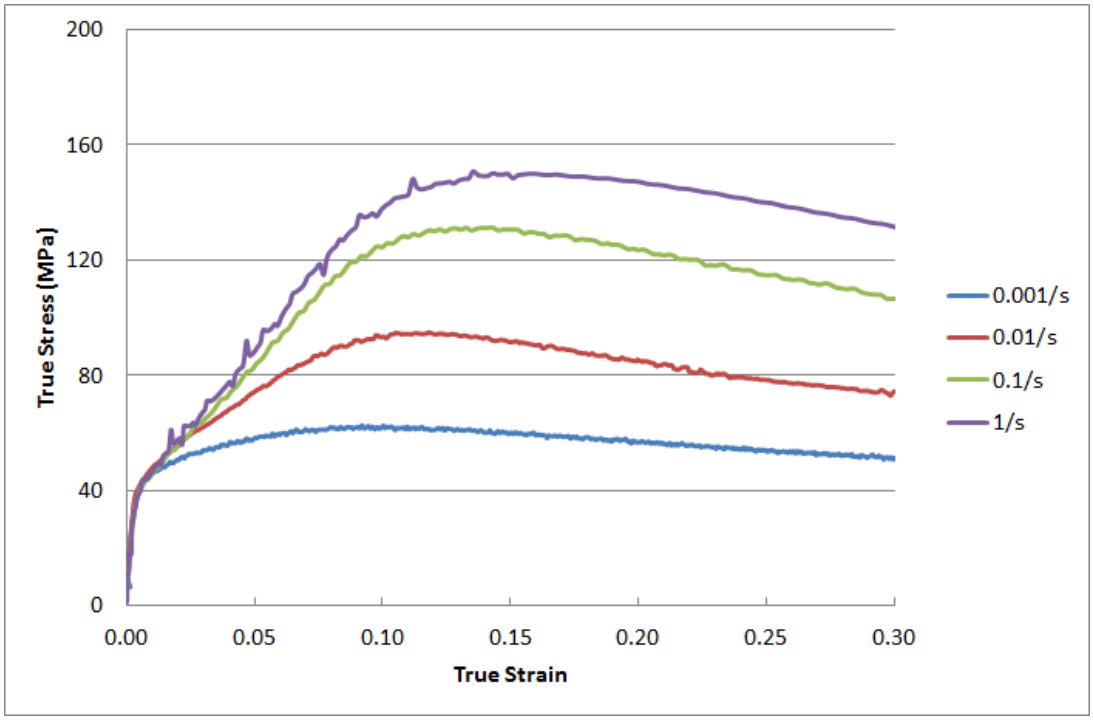

Figure 4-10: Flow stress curves for offset TD samples at 300°C and various strain rates.

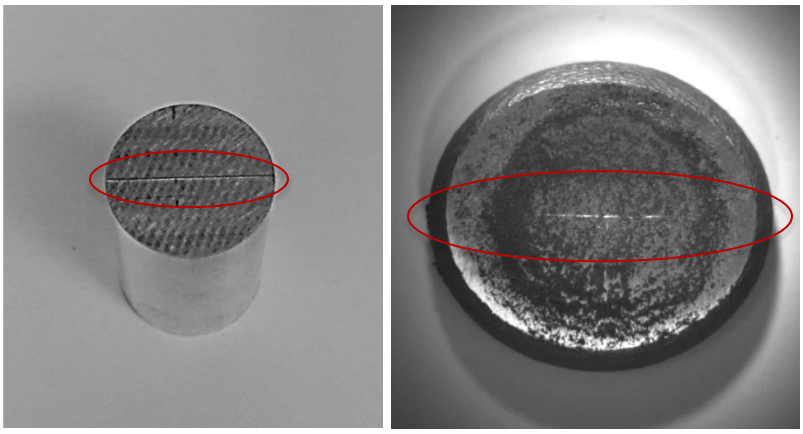

Figure 4-11: Images of offset TD samples prior to (left) and after (right) deformation at 500°C and $1.0s^{-1}$ to a true strain of 1.0 (extrusion axis aligned vertically).

Given that compression twinning and pyramidal slip were the only mechanisms oriented favourably, the observed anisotropy suggested that the initial texture in the compression sample was not as uniform as originally assumed. With consideration to the axisymmetric fiber texture in the extruded rod, it was evident the grains away from the sample centreline were rotated slightly, such that their c-axes were no longer parallel with the compression axis. The lack of texture uniformity in the sample produced a favourable orientation for basal slip at locations away from the sample centreline. Considering the initial texture of the sample, the occurrence of basal slip along the direction of the scribe line would result in preferential elongation in that direction.

The activation of basal slip at select locations of the compression sample was supported by the observed flow behaviour. Comparing the flow stress curves for the offset ED and TD samples, it was evident that the TD sample exhibited a lower yield stress. The flow stress curves for an offset ED and an offset TD sample, deformed at 300°C and $1.0s^{-1}$, are shown in Figure 4-12. If all the grains in the TD sample were assumed to be undergoing c-axis compression, the flow stress curve was not in agreement with those observed by Yukutake et al. [17], Lee et al. [18], and Dai et al. [19], where samples along the normal direction of the hot rolled plate exhibited a higher yield stress. Therefore, the low yield stress observed in the offset TD sample of the current study was attributed to the activation of basal slip at select locations of the sample.

Examination of the sample surfaces revealed the presence of macroscopic shear bands for certain deformation conditions. Shear bands were observed for all deformation temperatures below 450°C for strain rates of $1.0s^{-1}$ and $10^{-1}s^{-1}$, and below 400°C for strain rates of $10^{-2}s^{-1}$ and $10^{-3}s^{-1}$. The observation suggested that shear band formation was more likely to occur at higher strain rates. The presence of shear bands on the surface after deformation at 300°C, and the absence of them after deformation at 500°C, is evident in Figure 4-13.

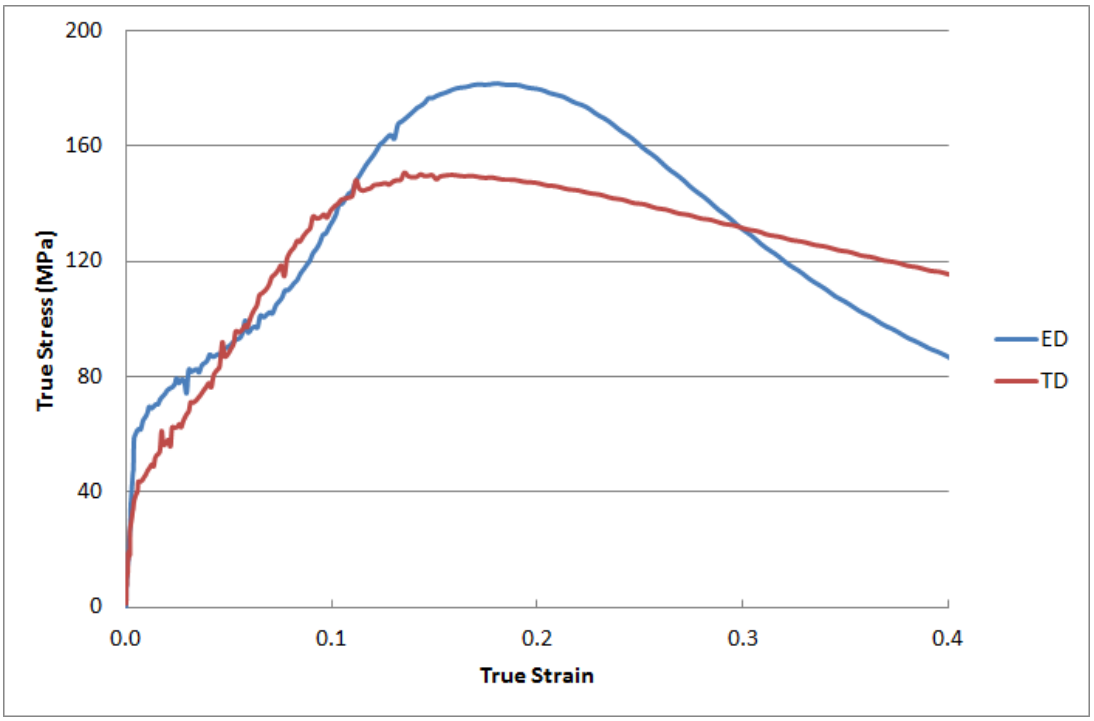

Figure 4-12: Flow stress curves for offset ED and TD samples at 300°C and $1.0s^{-1}$.

Consistent with the observations of Sun et al. [15] and Kim et al. [16], the shear bands consisted of fine DRX grains and appeared to have developed within twins that had split coarse grains during early stages of deformation. Since the initial texture along the centreline of the compression sample did not favour tensile twinning, the twins observed in the microstructure were suspected to be compression twins. The microstructures of offset TD samples after deformation at 300°C and 500°C are shown in Figure 4-14. With the DRX regions still retaining the twin outline after deformation at 300°C, it was evident that strain had been localized within the DRX region up to a true strain of 0.50. However, no such evidence was observed at 500°C, which suggested the relative ease at which pyramidal slip was activated at high temperature.

Furthermore, it was evident that compressive twinning was no longer the most favourable deformation mechanism.

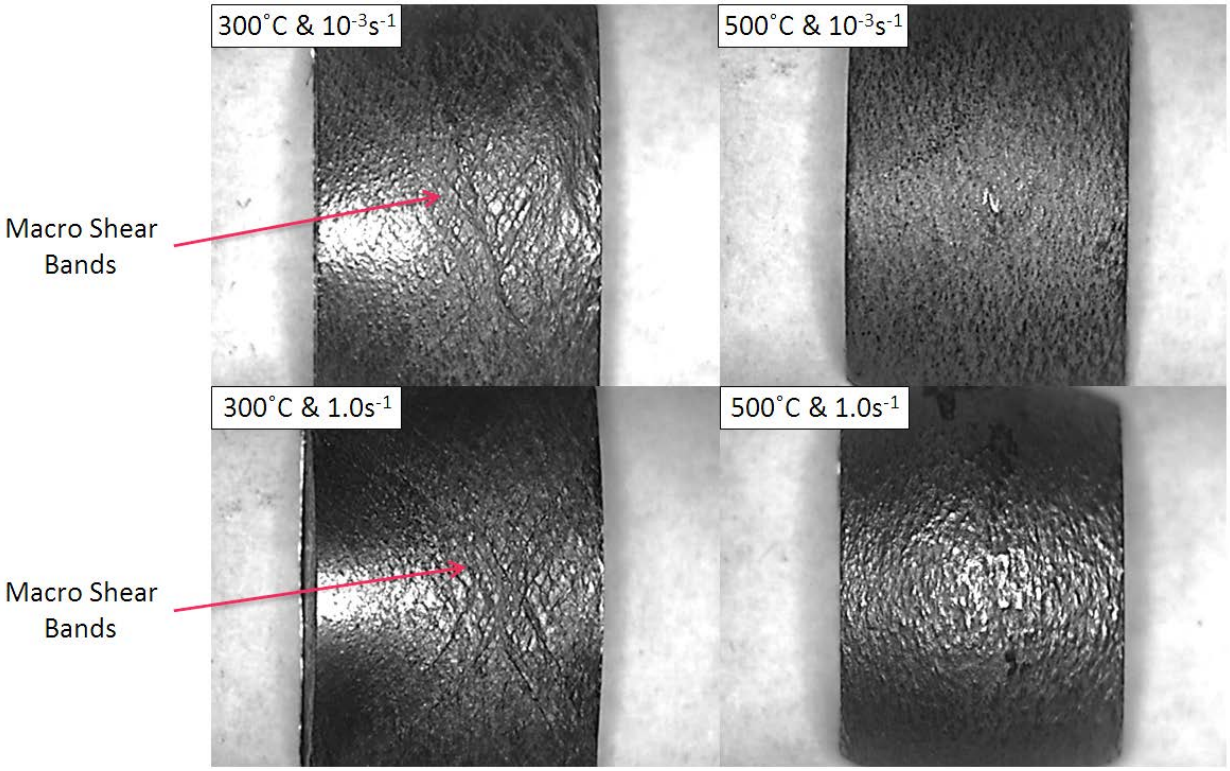

Figure 4-13: Images of offset TD samples deformed to a true strain of 0.50, under various conditions.

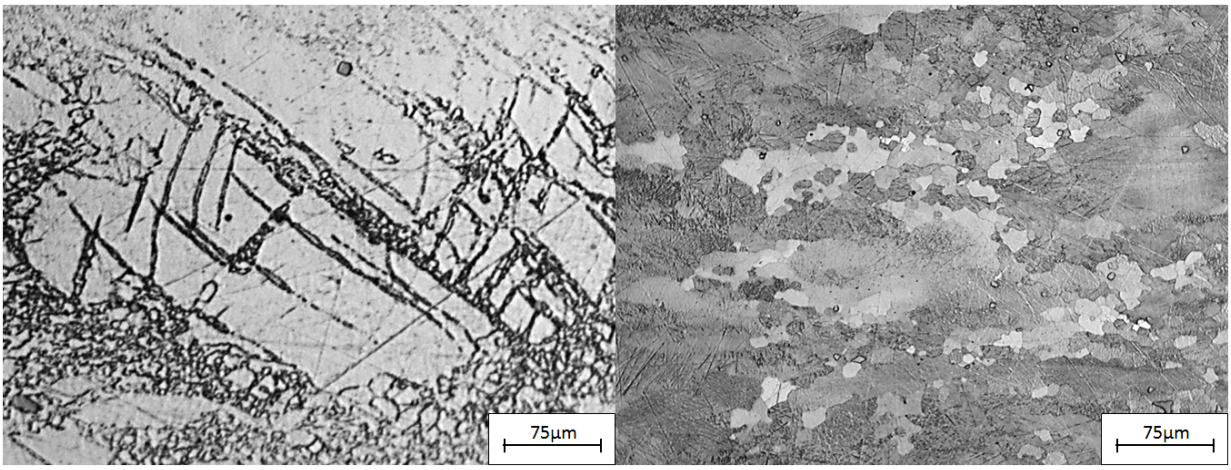

Figure 4-14: Micrographs of offset TD samples deformed to a true strain of 0.50, at 300°C and $1.0s^{-1}$ (left), 500°C and $1.0s^{-1}$ (right).

It was previously determined that the activation of basal slip resulted in preferential material flow within the TD sample, thus the suppression of basal slip would therefore restore the symmetry of flow. Recall that Li et al. [28] observed the acceleration of texture evolution with an increase in deformation strain rate. By increasing the deformation strain rate, the grains oriented favourably for basal slip more rapidly rotated into orientations of hard slip, thus basal slip was more rapidly suppressed and pyramidal slip became favoured. The above explains why the TD samples deformed at 500°C and high strain rates exhibited the least anisotropy, and the extent of anisotropy increased with decreasing strain rate. The transition in strain rate dependence observed after 400°C was attributed to a change in deformation mechanism, with pyramidal slip becoming more favourable than compressive twinning.

With pyramidal slip not being readily activated at low temperatures, strain along the < c > direction at the sample centreline was accommodated by compressive twinning. Since compressive twinning of the $\{10\bar{1}1\}$ type rotates the grains by almost 60° [41], grains along the centreline of the TD sample rotated to orientations of soft slip, where basal slip and prismatic slip were favourable. Both basal slip and prismatic slip would have a strain component along the direction of the scribe line. Given that samples deformed below 400°C exhibited greater anisotropy at higher strain rates, it was suspected that, like tensile twinning, the activity of compression twins was greater at higher strain rates.

To study the impacts of texture uniformity on the observed anisotropy and flow stress behaviour, smaller (i.e. Ø4mm by 6mm) offset TD samples were produced from the same Ø63.5mm extruded rod. The smaller size resulted in less texture variation within each compression sample. A schematic of the scaled TD sample is shown in Figure 4-15. The flow curves for the full sized ED and TD samples, along with the scaled TD sample, deformed at 350°C and $1.0s^{-1}$ are shown in Figure 4-16. The reduced activity of basal slip, as a result of more uniform texture, was observed through the increase in flow stress compared to the full sized TD sample. Furthermore, the minor to major axis ratio had increased slightly from 0.68 for the full sized TD sample to 0.70 for the scaled sample, and the scribe line was still oriented along the major axis. In the case of a hot rolled plate (i.e. uniform texture within the sample), the limited activation of basal slip would have resulted in the flow stress being even higher than that of the ED sample [17, 18, 19].

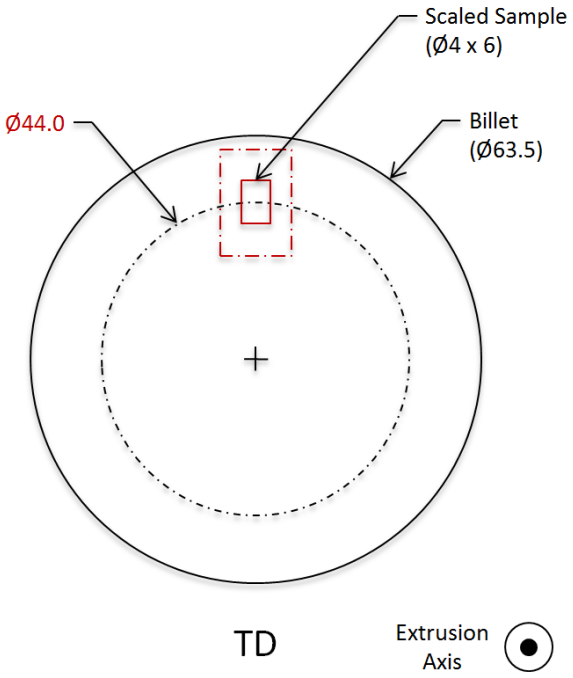

Figure 4-15: Schematic of scaled TD sample. Dashed outline represents the full sized sample.

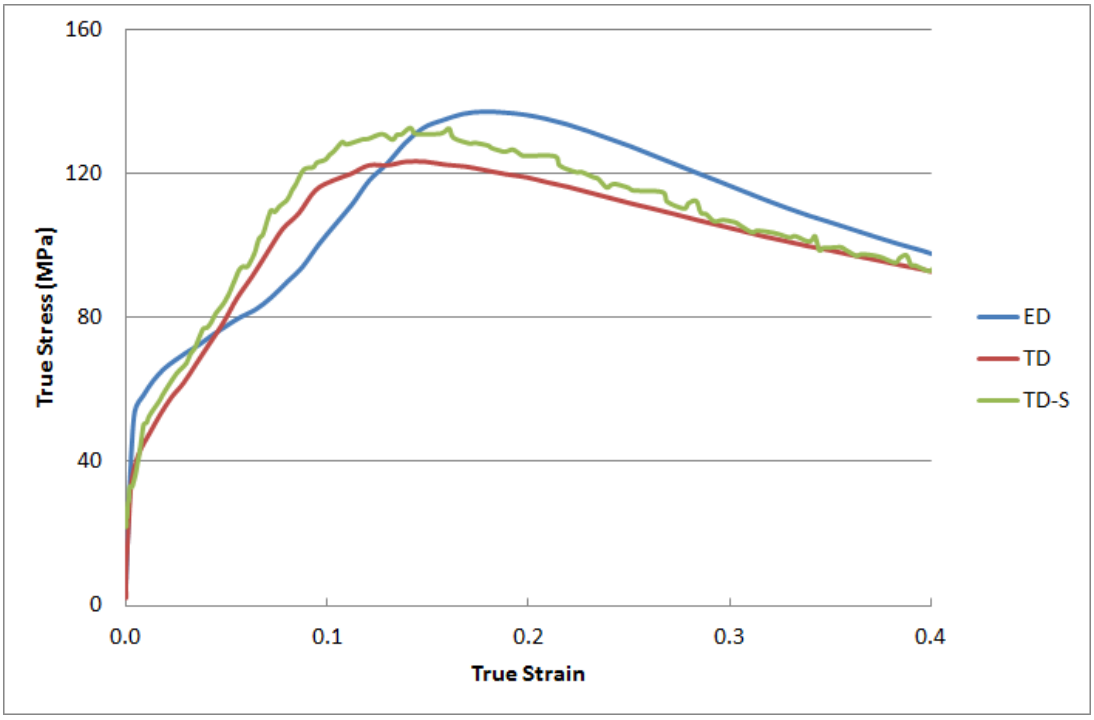

Figure 4-16: Flow stress curves for full sized offset ED and TD samples, and TD-Scaled samples deformed at 350°C and 1.0s^{-1}.

4.1.3 As-Cast Condition

As discussed previously, the initial texture of the compression samples had resulted in preferential material flow during hot deformation. The role of initial texture was verified through examination of the final geometries for the as-cast samples. The strong axisymmetric fiber texture developed through hot extrusion was not expected in the cast material; instead a random texture was observed (i.e. no preferred orientation).

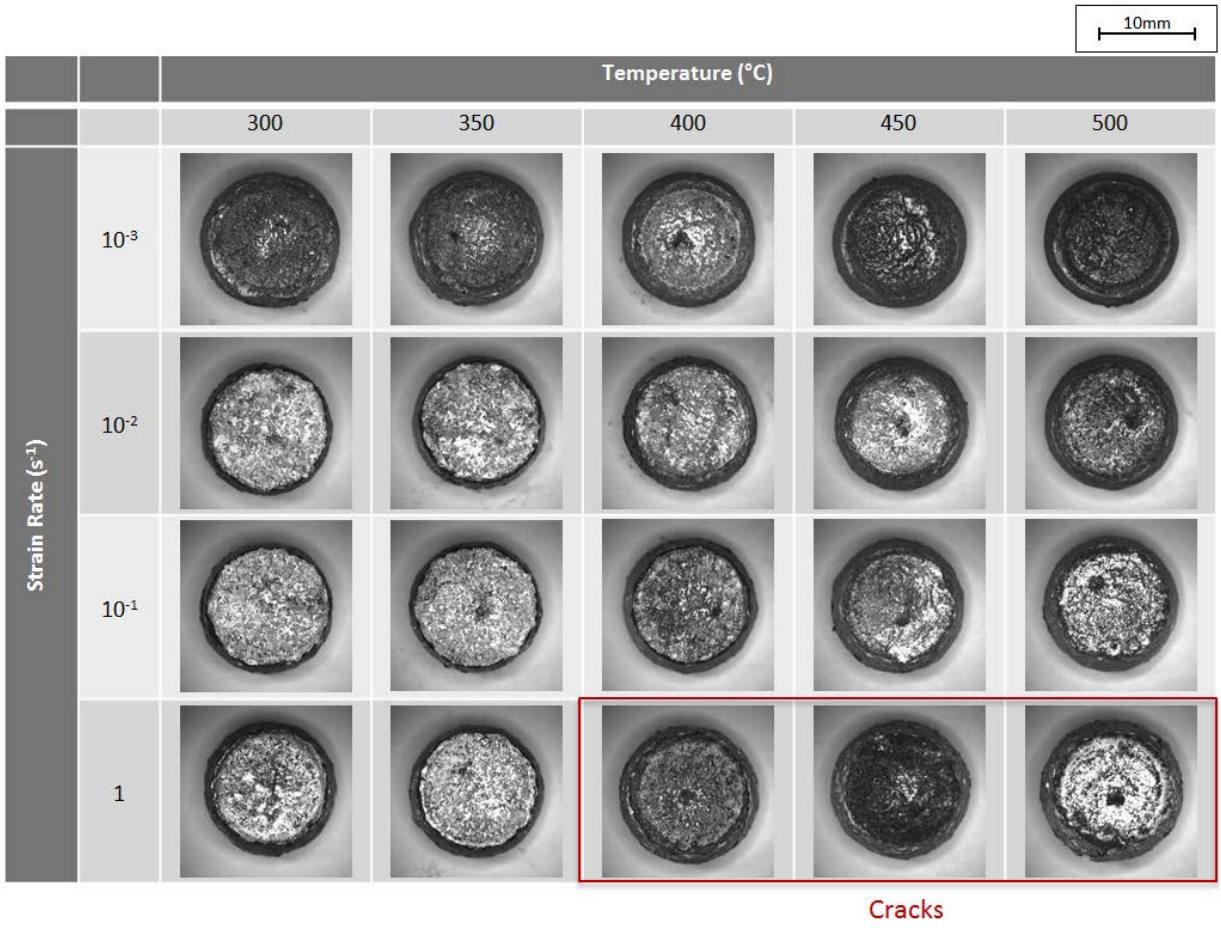

Figure 4-17: Top-view images of as-cast samples deformed to a true strain of 0.50.

Examining the final geometries after deformation, it was evident that the as-cast samples exhibited no preferential material flow under any investigated deformation condition. However, fractures occurred for the strain rate of $1.0s^{-1}$ when the deformation temperature exceeded 350°C. Images of the deformed as-cast samples are shown in Figure 4-17. Although porosity is a common defect in cast materials, large porosities were not observed in the initial microstructure.

Furthermore, pores that were present in the microstructure would have been closed upon hot compression. Therefore, the cracks observed in the as-cast condition were not attributed to coalescing of solidification pores. However, it was observed that the as-cast samples exhibited "orange peeling" on the surface after deformation, as a result of the coarse initial grain size. On the contrary, the extruded material produced a smoother surface after deformation.

4.2 Effect of Heat Treatments

4.2.1 Furnace Soak Time

With the intent of relating findings from the current study to an industrial forging process, it was important to evaluate any changes to the microstructure during the heating of the billet or ingot up to the deformation temperature. The material would then be held at temperature in the furnace for a period of time to eliminate any temperature gradients within the material. To replicate a furnace soak time, compression samples from the extruded rod were held at 450°C for three hours and water quenched. The resulting microstructures for the offset ED samples are presented in Figure 4-18. Water quenching of the sample immediately after the furnace soak, combined with rapid heating in the Gleeble® (i.e. at 10°C per second) up to the testing temperature, served as a simplified simulation of forging immediately after the billet was removed from the furnace.

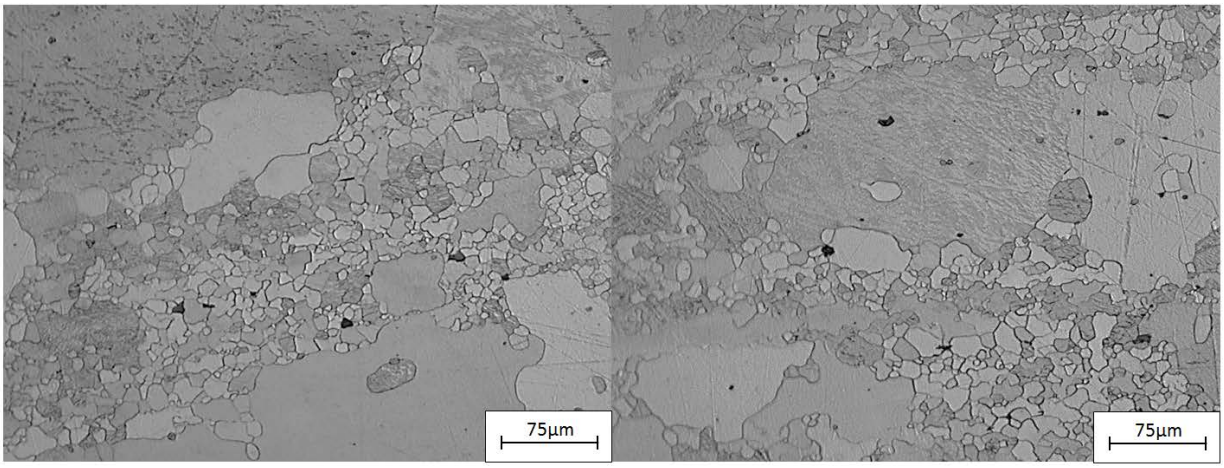

Figure 4-18: Micrographs of as-received (left) and annealed (right) offset ED samples.

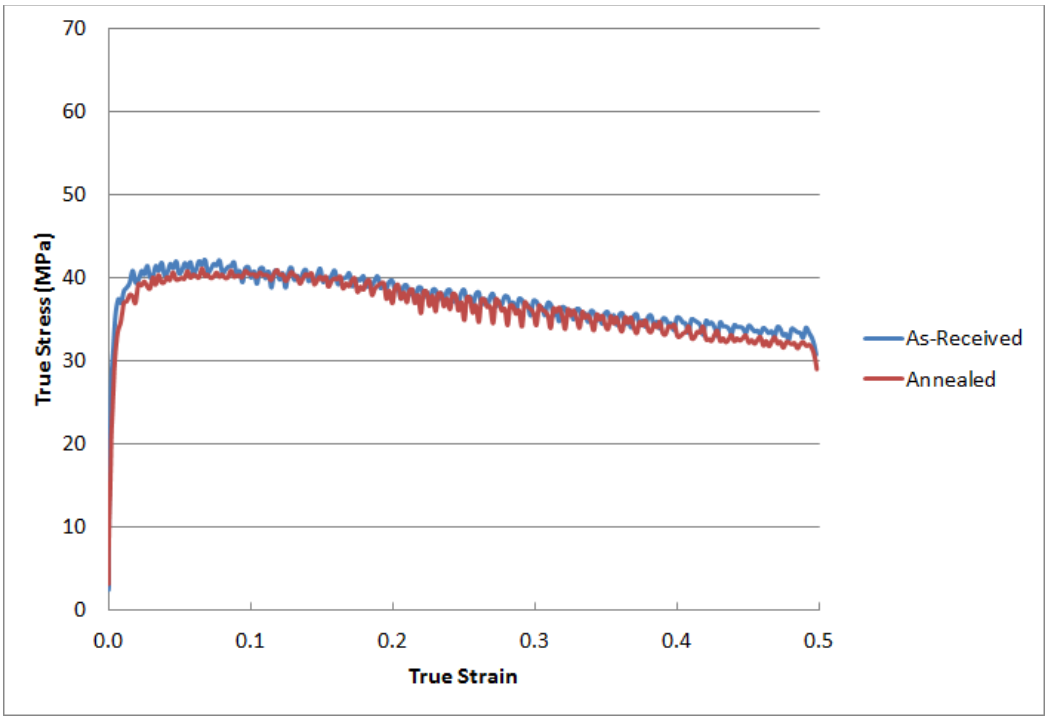

Figure 4-19: Flow curves for as-received and annealed offset ED samples, at 450°C and $10^{-1}s^{-1}$.

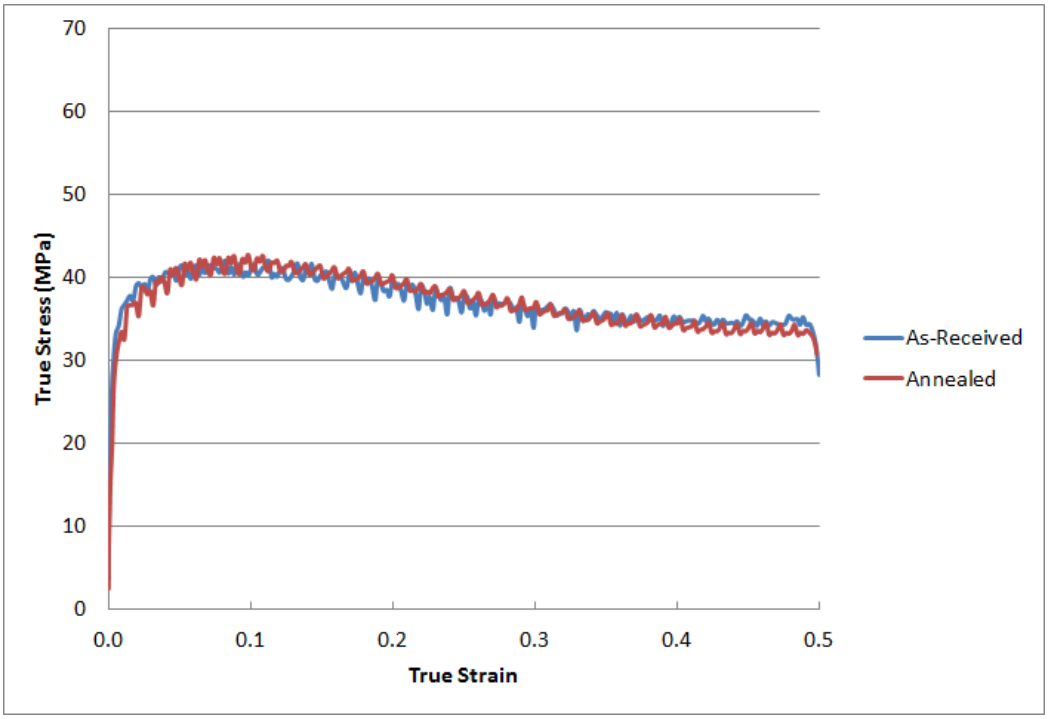

Figure 4-20: Flow curves for as-received and annealed offset TD samples, at 450°C and $10^{-1}s^{-1}$.

The micrographs obtained prior to and after annealing for 3 hours showed very similar microstructures. Abnormal grain growth, which led to the strengthening of the $<11\bar{2}0>$ pole, observed by Pérez-Prado and Ruano [26] and by Yi et al. [27] was not observed in the current study. Furthermore, the flow stress curves obtained from compression at 450°C and $10^{-1}s^{-1}$ showed no significant differences. The stress-strain curves for the as-received and annealed ED samples are shown in Figure 4-19. The same observation was made for the offset TD sample, where the microstructures and flow stress curves showed no observable differences after annealing. The stress-strain curves for the TD samples are shown in Figure 4-20. Furthermore, the final post-deformation geometries of the as-received and annealed samples were very consistent for both orientations.

The as-cast samples were also put through the same furnace heat treatment. Unlike the extruded material, significant differences were observed in the stress-strain curves, as well as in the microstructures. Since the material was essentially homogenized at 450°C for 3 hours, the result was to be expected. The dendritic structure from casting was still observable in the sample after the three hour furnace soak. The results obtained from a full homogenization treatment will be discussed in the subsequent section.

4.2.2 Homogenization Treatment

Differential scanning calorimetry (DSC) was utilized to determine the thermal events occurring within the as-cast material. The DSC traces obtained during the heating cycle for both the extruded and as-cast materials are shown in Figure 4-21. Each thermal event was identified by comparing the peaks in the DSC traces to the predictions made by thermochemical software FactSage™ [42], under the Scheil solidification condition. The phases predicted by FactSage™ [42] are shown in Figure 4-22. It was believed that the broad endothermic peak observed in the as-cast material between 340°C to 360°C encompassed the complete melting of the MgZn, AlMgZn, and $Mg_{12}Al_5Zn_5$ phases, with the rapid melting of $Mg_{17}Al_{12}$ occurring between 400°C and 415°C, as indicated by the sharp endothermic peak. Furthermore, the continual melting of the α-Mg and Al_8Mn_5 phases was to be expected beyond temperatures of 340°C and 400°C, respectively.

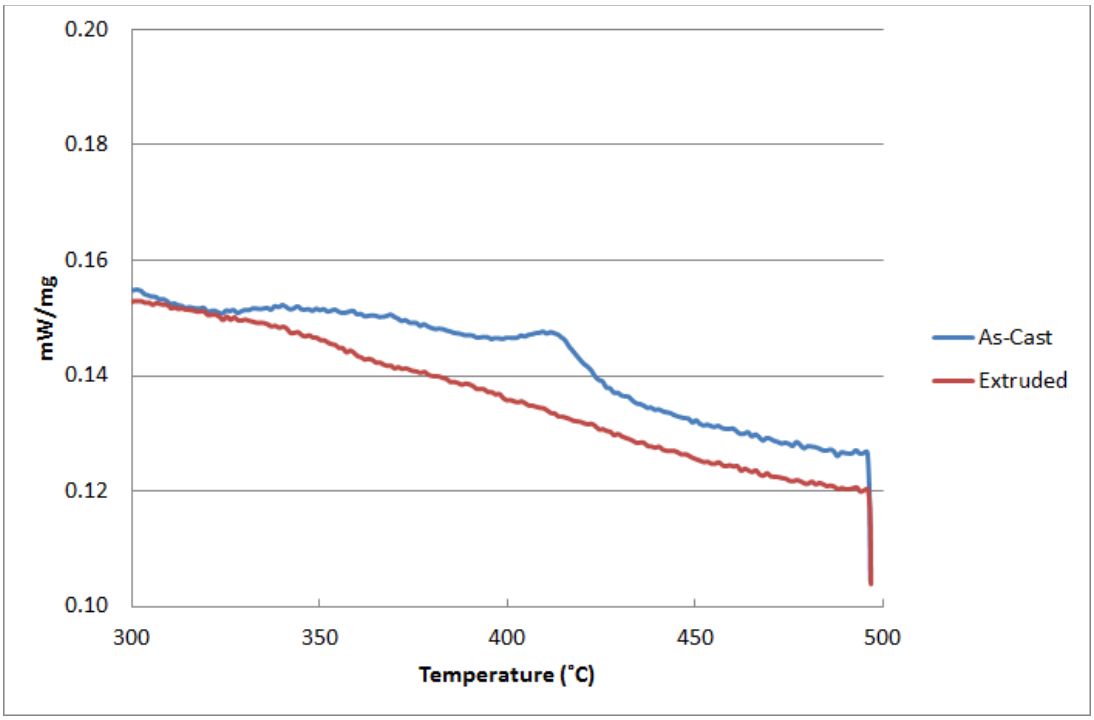

Figure 4-21: DSC traces for offset ED and as-cast samples.

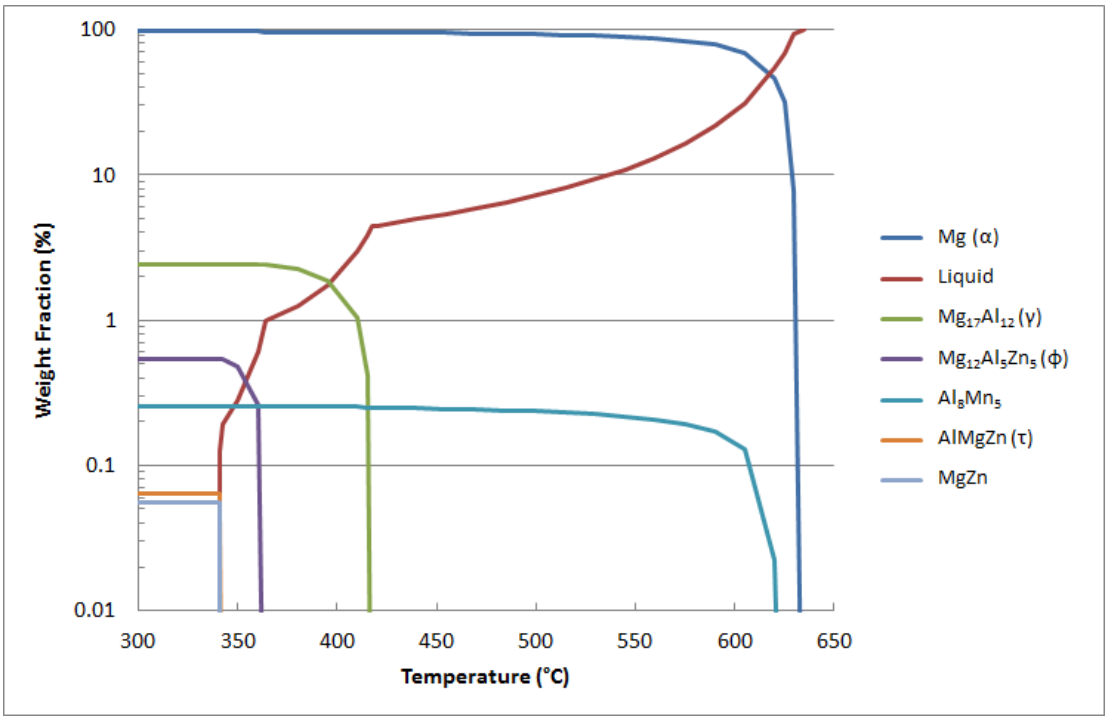

Figure 4-22: Phases predicted by FactSage™ [42].

It should be noted that the onset temperature for melting of the $Mg_{17}Al_{12}$ phase coincides with the lowest temperature (i.e. 400°C) at which cracking was observed in the as-cast material for a strain rate of $1.0s^{-1}$. No distinct peaks were observed in the DSC trace of the extruded material, which suggested that the low melting point phases had been dissolved during extrusion. Furthermore, it should be noted that the melting range and associated enthalpy of a thermal event, as captured by the DSC, have shown dependence on the heating rate and sample mass [43]. Therefore, the traces obtained from the DSC were expected to exhibit some deviations from the FactSage™ [42] predictions. In addition, the baseline (i.e. reference trace) may have shifted from one test to another due to differences in the sample-crucible contact interface, and/or chemical reactions between the previous sample and the crucible. Therefore, each trace was examined independently for thermal peaks, and direct quantitative comparisons between the traces were avoided.

The flow behaviour observed after homogenization differed from the as-cast condition. Note that due to sample availability, the as-cast compression tests were conducted on samples from ring 7 of the ingot, and the homogenized samples were extracted from ring 8. Despite the slight difference in chemical composition, compression behaviour of the as-cast samples from both rings 7 and 8 were very consistent during deformation at 400°C for all strain rates. The results of the comparison can be found in Appendix D. Comparing the flow stress curves for the two conditions, it was observed that the homogenized samples exhibited lower flow stresses compared to their as-cast counterparts, with the only exceptions being at temperatures above 350°C, at the highest strain rate of $1.0s^{-1}$, where cracks formed in the as-cast samples had lowered the observed flow stresses. The results were in agreement with those observed by Prasad and Rao [22]. The flow stress curves obtained at 350°C for the as-cast and cast-homogenized samples are shown in Figure 4-23 and Figure 4-24, respectively. Note that a decrease in yield stress was observed in some cases when the deformation strain rate was increased, the cause of the softening will be discussed in a subsequent section.

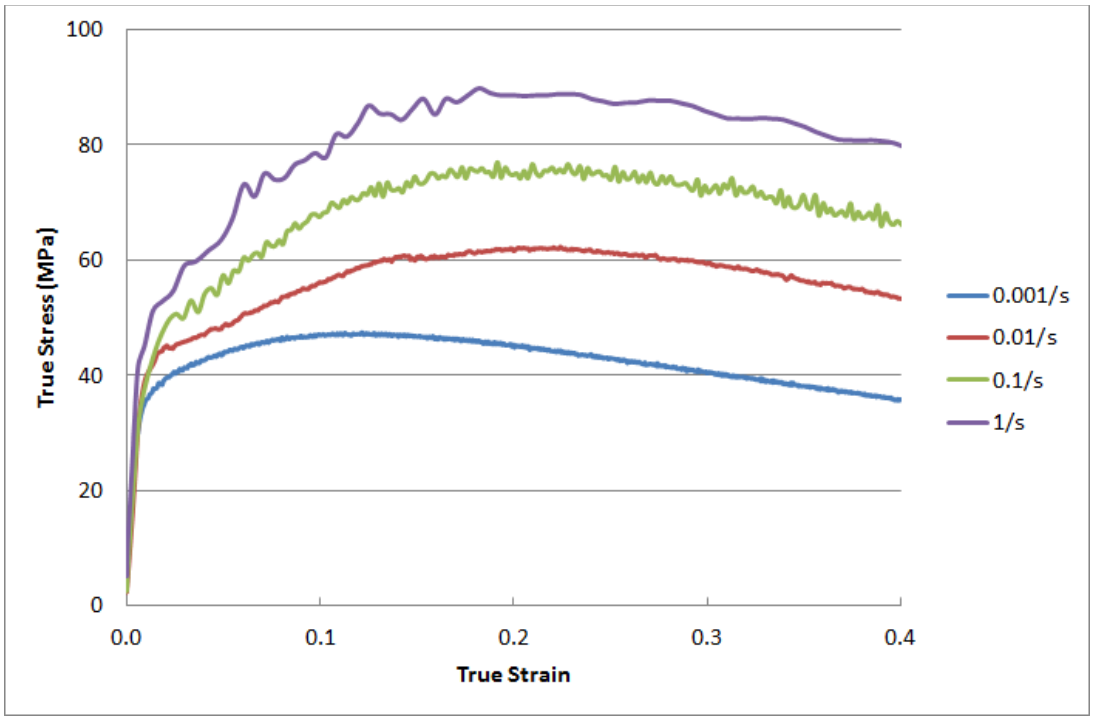

Figure 4-23: Flow stress curves for as-cast samples deformed at 350°C and various strain rates.

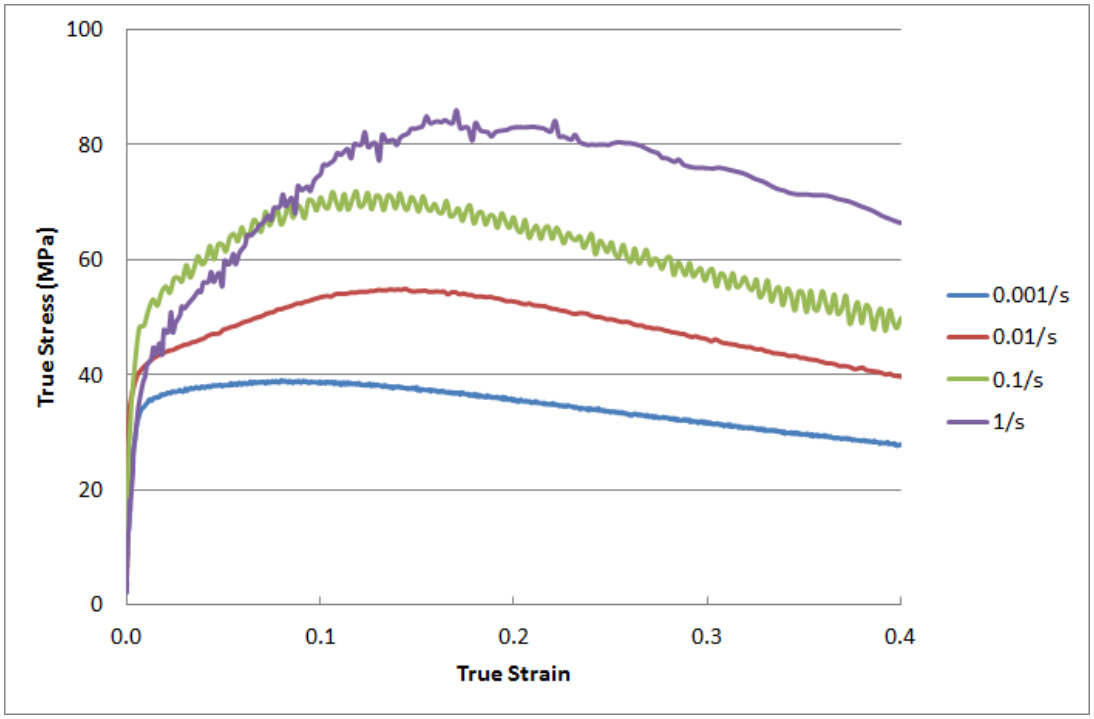

Figure 4-24: Flow stress curves for cast-homogenized samples deformed at 350°C and various strain rates.

To further investigate the homogenization behaviour of the cast material, additional homogenization heat treatments were developed; the conditions are shown in Figure 4-25. It was evident the samples homogenized at 500°C experienced severe surface oxidation compared to those homogenized at 400°C or 450°C. The air cooled samples provided data for a traditional homogenization treatment at two homogenization temperatures. The water quenched samples provided insight on the effectiveness of a furnace soak as a homogenization treatment. Considering the relatively low amount of alloying content, it was suspected that precipitation which occurred during cool down would not have a significant impact on hot workability.

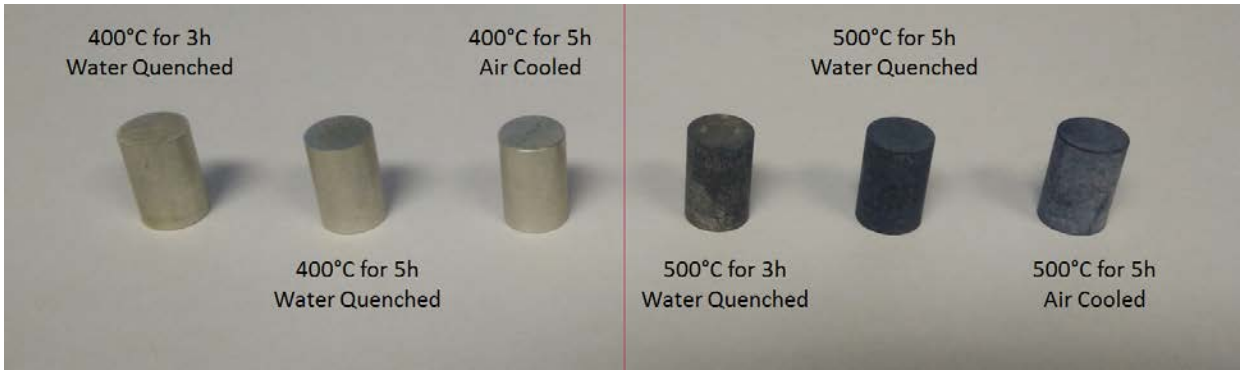

Figure 4-25: Compression samples homogenized under various conditions.

The DSC traces for the samples which had been homogenized at 400°C and 500°C are shown in Figure 4-26 and Figure 4-27, respectively. It was evident that the sharp endothermic peak observed for the as-cast condition at 400°C was no longer present after homogenizing for five hours. The result suggested that melting of the $Mg_{17}Al_{12}$ phase had been suppressed. However, for the three hour treatments, broad endothermic peaks were observed to begin at 400°C for the 400°C treatments, and at 425°C for the 500°C treatments. It was suspected that, during homogenization, melting of the $Mg_{17}Al_{12}$ phase had occurred upon heating, and diffusion of magnesium into the liquid phase had occurred. The increased magnesium content within the liquid phase had shifted the solidus temperature, and allowed for partial solidification of the liquid phase. Upon quenching, and reheating in the DSC, the chemical composition within the previously liquid region had changed and melting had been shifted to a higher temperature range. Due to more rapid diffusion kinetics at higher temperature, it was no surprise that the change in melting range was more drastic for the treatment conducted at 500°C. Therefore, it was seen that homogenizing for three hours was insufficient in suppressing the melting traces.

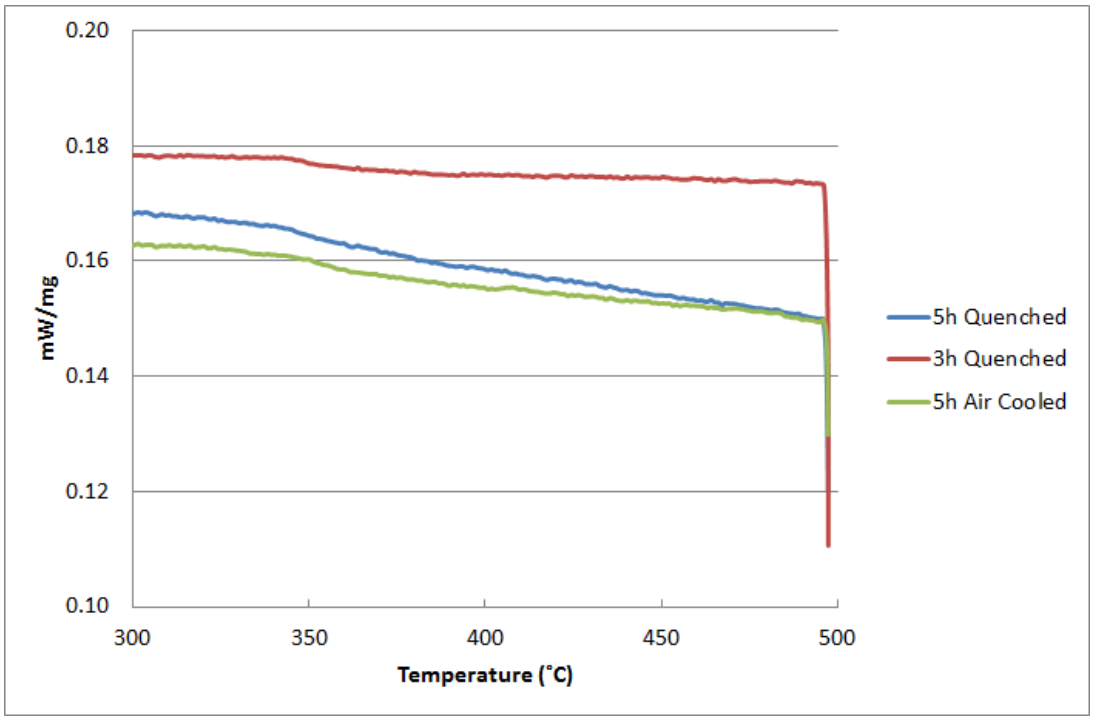

Figure 4-26: DSC traces after homogenization treatments at 400°C.

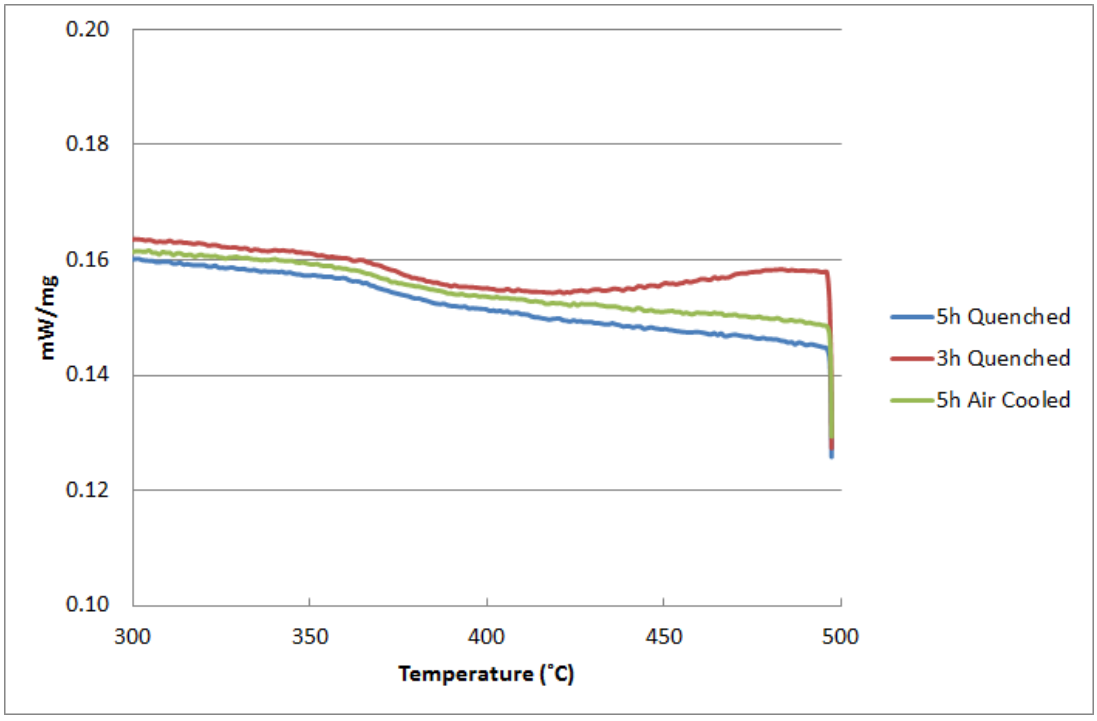

Figure 4-27: DSC traces after homogenization treatments at 500°C.

4.3 Microstructure Development

4.3.1 Effect of Thermal-mechanical Processing Conditions

One major benefit of forging is the improvement in the final mechanical properties of the in-service component. The improvements over an equivalent cast component are obtained through the development of a defect-free, fine-grained, and homogeneous microstructure. To understand the effects of thermal-mechanical processing conditions on the microstructure, offset ED samples which had undergone uniaxial compression to a true strain of 0.50 were examined. The microstructures, with emphasis on the DRX regions, are presented in Figure 4-28.

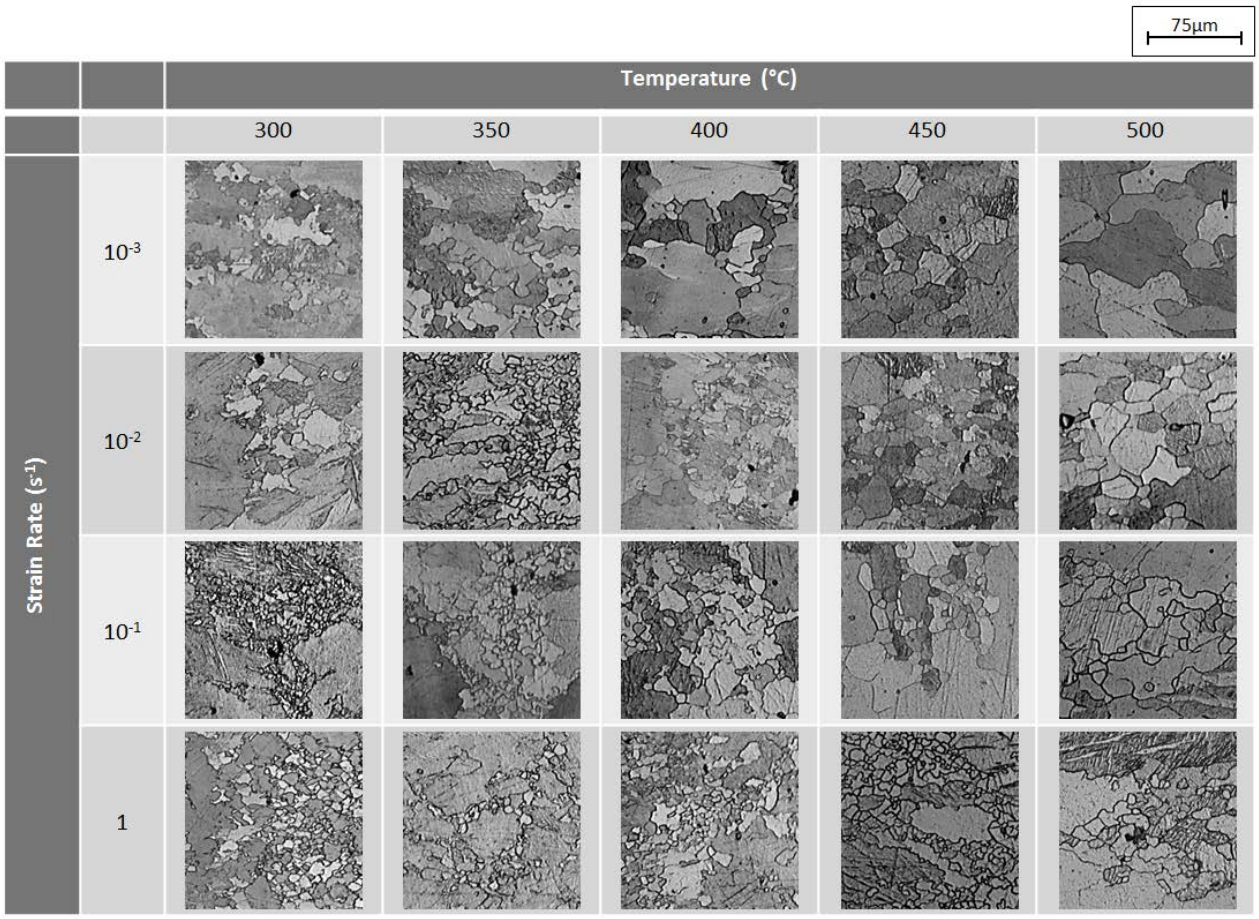

Figure 4-28: Micrographs of DRX regions within offset ED samples after deformation to a true strain of 0.50, under various conditions.

It was observed that the DRX grain size increased with deformation temperature, and decreased with increasing strain rate; the observations are consistent with those of Beer and Barnett [14]. The result was expected as the lower strain rates provided longer times at high temperature for grain growth. It was evident that processing at high temperature had the benefit of producing microstructures of greater homogeneity; however larger DRX grain sizes were produced. With consideration to production rates, the higher strain rate conditions have received greater attention in the current study. Microstructures obtained after deformation at temperatures between 400°C and 500°C are shown in Figure 4-29 and Figure 4-30. From the images at 200x magnification, it was evident that the microstructure lacked homogeneity at a strain of 0.50. The effect of strain on the final microstructure will be discussed in the next section.

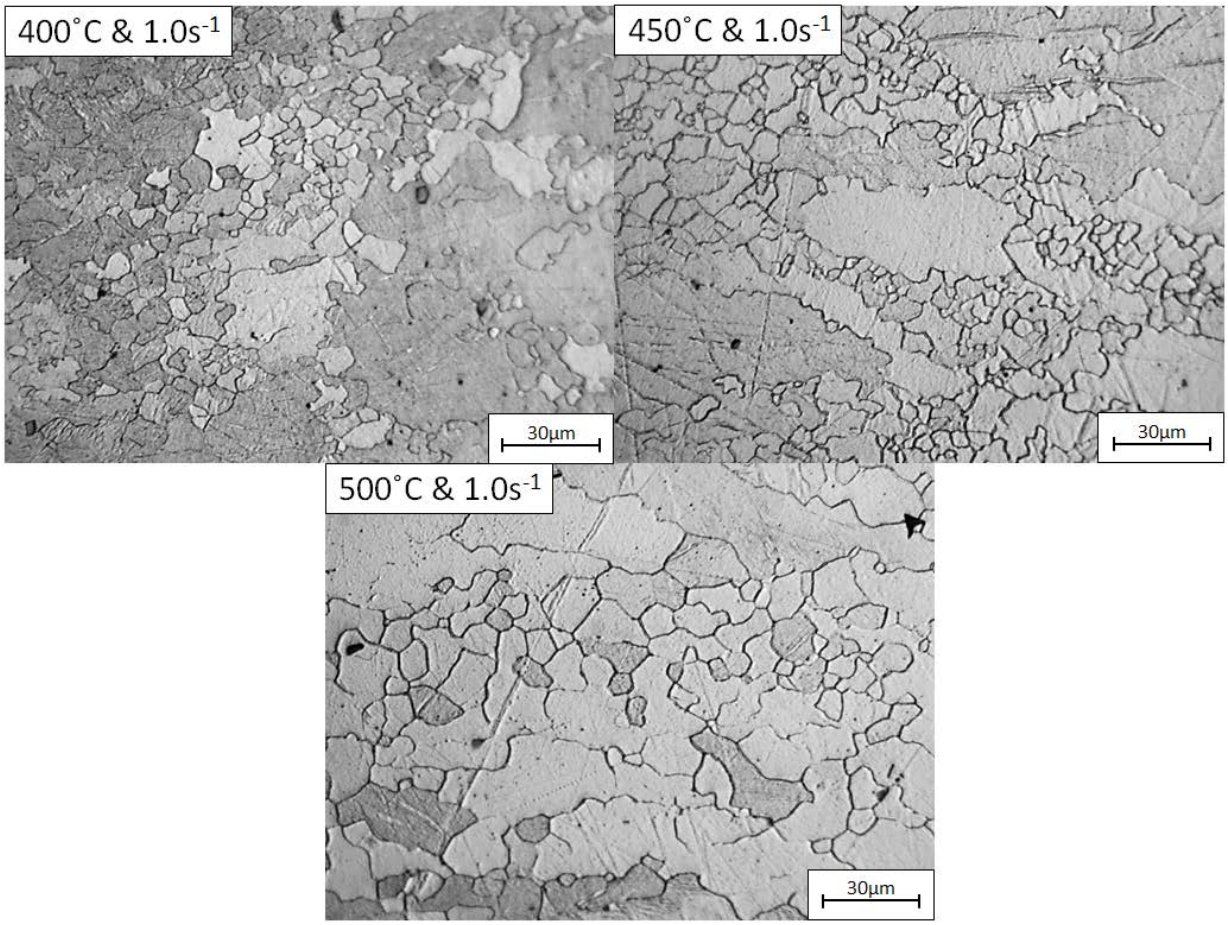

Figure 4-29: Micrographs of offset ED samples after deformation to a true strain of 0.50 at $1.0s^{-1}$ and various temperatures (500x magnification).

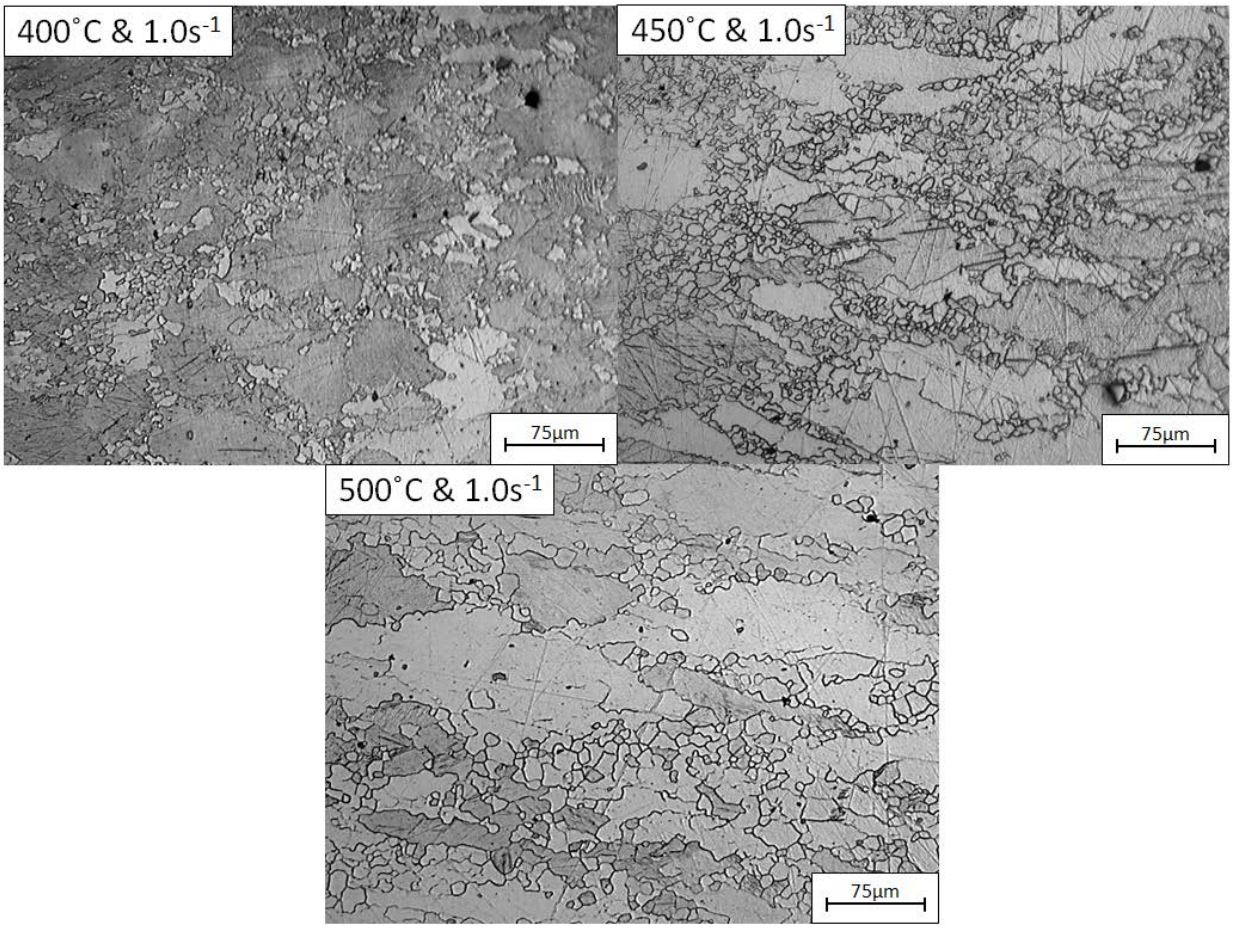

Figure 4-30: Micrographs of offset ED samples after deformation to a true strain of 0.50 at $1.0s^{-1}$ and various temperatures (200x magnification).

It had been observed by Barnett et al. [13] that a finer initial grain size resulted in lower flow stresses during deformation and also produced a finer grained microstructure after deformation. Considering the centre of the extruded rod exhibited finer grains, it was important to investigate the deformation behaviour of the centreline sample. The initial and post-deformation microstructures for both centreline and offset ED samples are shown in Figure 4-31. Despite the large differences observed in the initial microstructure, the microstructures observed after deformation were very similar. However, the flow stress behaviour shown in Figure 4-32 was in agreement with that observed by Barnett et al. [13].

Considering that rapid grain growth was observed by Miao et al. [44] in fine grained AZ31 produced by hot rolling, it was important to determine how the microstructure in the centreline sample had changed during heat up prior to deformation. A centreline ED sample was heated to

500°C, held for five seconds, and water quenched. The resulting microstructure is presented in Figure 4-33. Examination of the microstructures revealed both abnormal and normal grain growth. However, the microstructure was still relatively fine grained compared to the offset sample. The finer grains in the centreline sample was a contributing factor to the lower flow stress, however the centreline sample was expected to have lower alloying content as a result of inverse segregation from casting [39] prior to extrusion. Considering that aluminum is added primarily for strength [2], the lower aluminum content likely contributed to the lower flow stress observed.

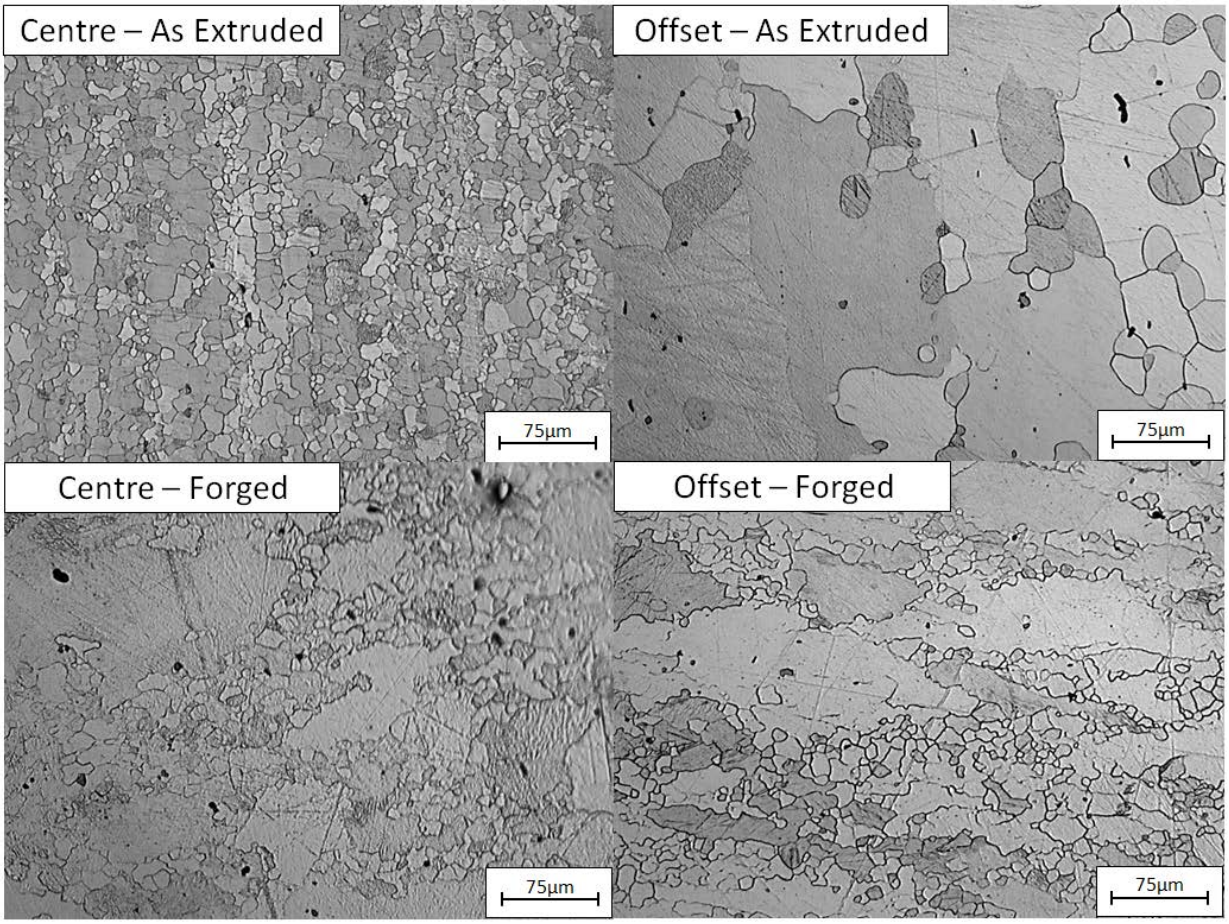

Figure 4-31: Micrographs of centre and offset ED samples before and after deformation at 500°C and $1.0s^{-1}$, to a true strain of 0.50.

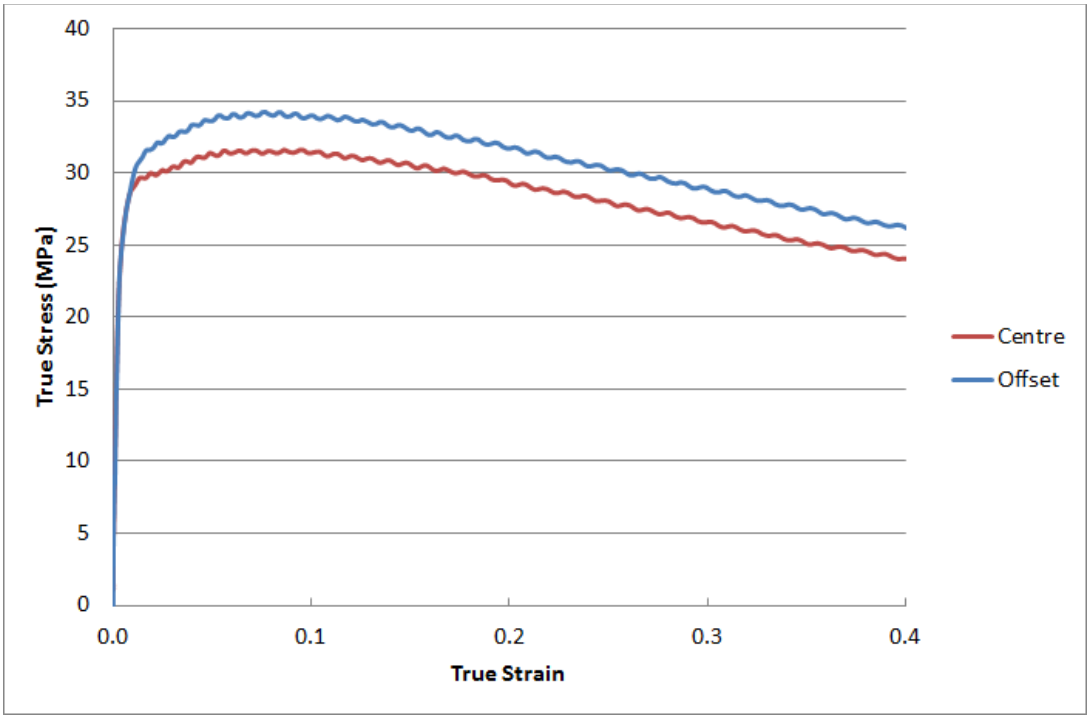

Figure 4-32: Flow stress curves for centre and offset ED samples at 500°C and 1.0s^{-1}.

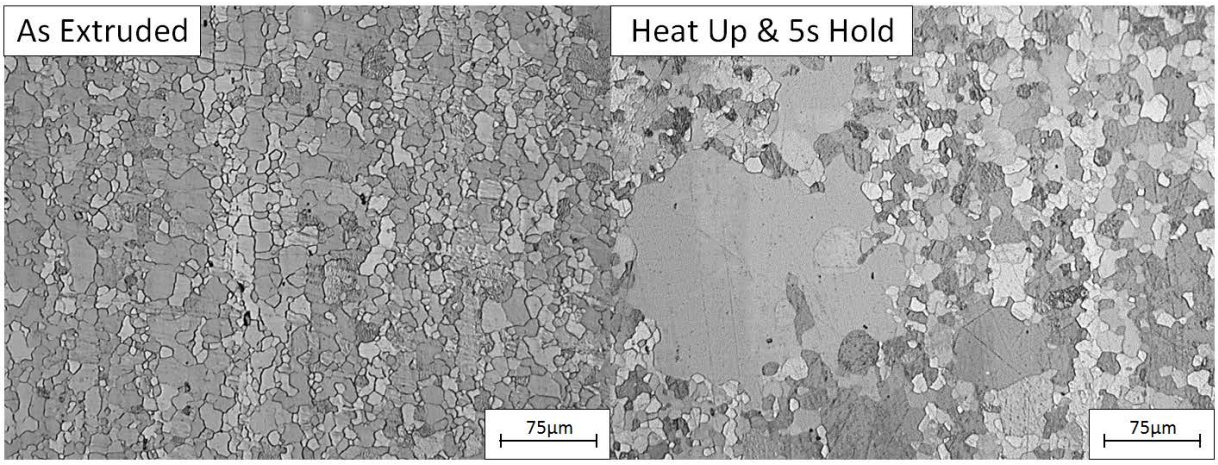

Figure 4-33: Micrographs of as-received and heated centreline ED samples.

For the cast material, it was evident that homogenization had widened the range of possible deformation conditions by allowing deformation to be successfully conducted at a strain rate of 1.0s^{-1} for temperatures of 400°C and above. No cracking was observed, up to a true strain of 0.50, for any investigated condition. To further evaluate the workability of the material at lower temperatures, the strain was varied for a deformation temperature of 350°C; the results are

shown in Figure 4-34. Cracks were observed at the surface of the sample for a true strain of 0.75, therefore it was clear that processing at 350°C was not ideal for bulk deformation processes like forging. To investigate the dependence of workability on deformation temperature, homogenized samples were deformed at 500°C to high strain; the results are provided in Figure 4-35. It was evident that processing at higher temperature improved the maximum strain that could be imparted on the sample. Closer examination of the effects of strain on the microstructure will be provided in the next section.

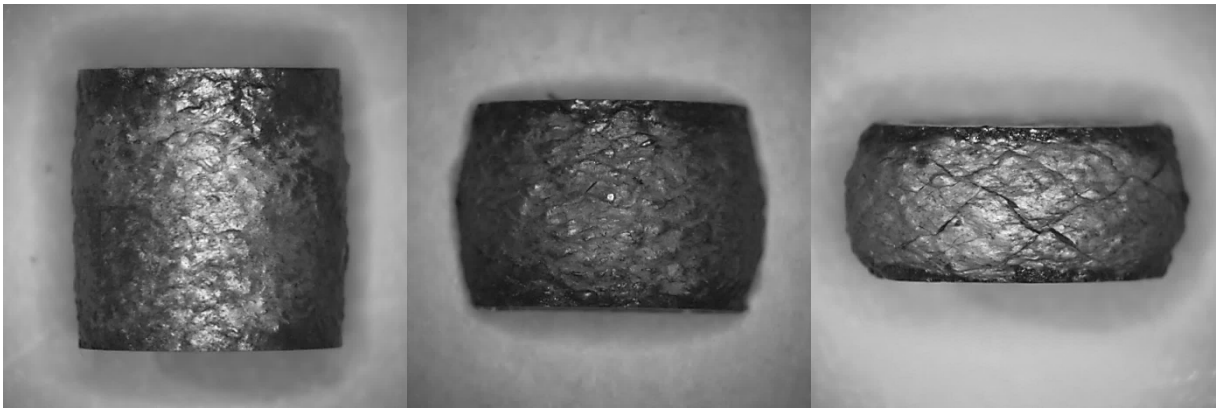

Figure 4-34: Images of cast-homogenized samples after deformation at 350°C and $1.0s^{-1}$, to strains of 0.25 (left), 0.50 (middle), and 0.75 (right). Images not to scale.

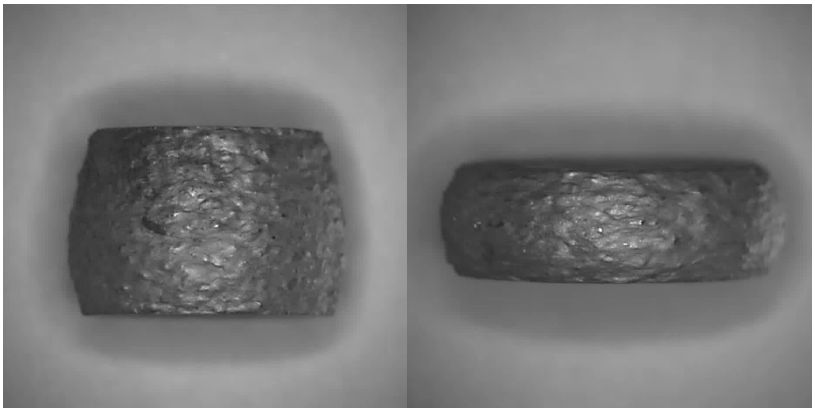

Figure 4-35: Images of cast-homogenized samples after deformation at 500°C and $1.0s^{-1}$, to strains of 0.50 (left) and 1.0 (right). Images not to scale.

4.3.2 Effect of Strain

It was previously observed that increasing the deformation temperature had increased the strain at which cracks began to form on the surface of the sample. Therefore, it was important to understand how the grain structure evolved with strain. As discussed previously, emphasis will be placed on the high strain rate deformation conditions. Considering that Al-Samman and Gottstein [12] observed no statistically significant differences in the average grain sizes of differently oriented samples for any given deformation condition, both ED and TD samples will be used for the remaining studies. Both offset ED and cast-homogenized samples were deformed to various levels of strain; the corresponding microstructures are presented in Figure 4-36 and Figure 4-37, respectively.

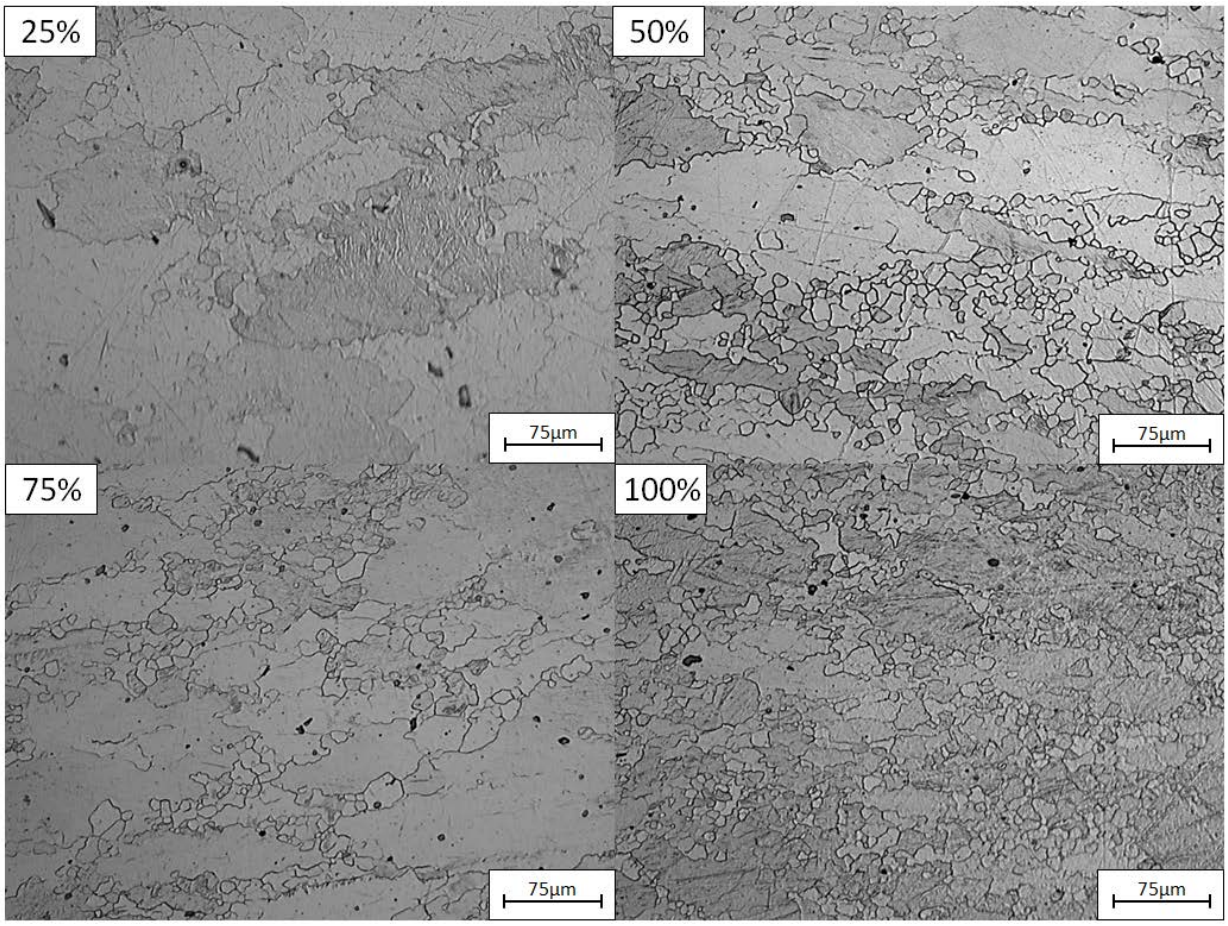

Figure 4-36: Micrographs of offset ED samples after deformation at 500°C and 1.0s^{-1}, to various levels of strain.

In both the materials, it was evident that the volume fraction of DRX grains increased with strain, with little to no change in the DRX grain size. The result was in agreement with those observed in other studies [10, 11]. Furthermore, the volume fraction of DRX grains was higher in the wrought material for all investigated strains; the result was consistent with those of Beer and Barnett [14], although a larger DRX grain size was not observed for the cast-homogenized material in the current study. It was clear that a fully recrystallized microstructure was not obtained in either material after deformation to a true strain of 1.0. Considering the samples were water quenched after deformation, the effect of cooling rate after deformation will be discussed in the next section.

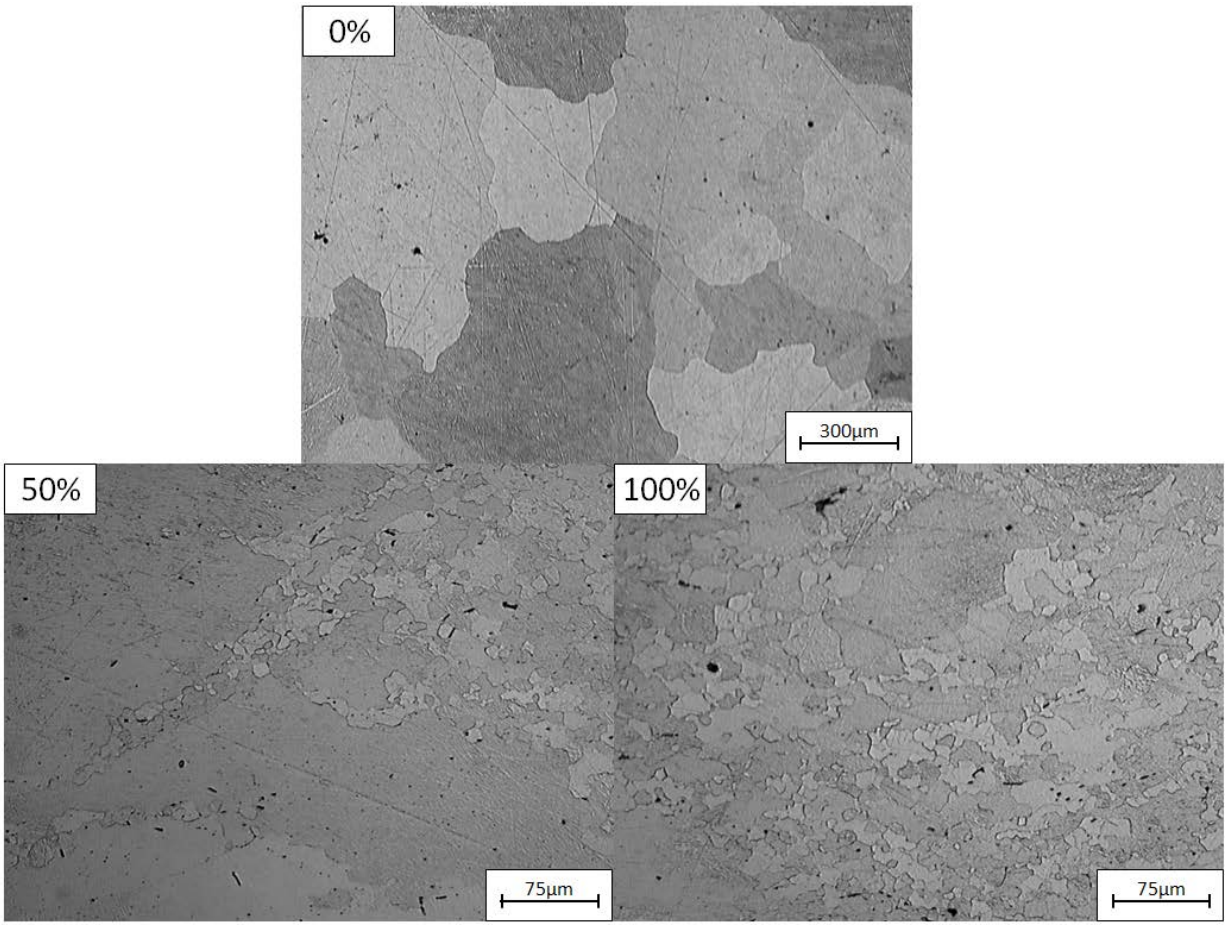

Figure 4-37: Micrographs of cast-homogenized samples after deformation at 500°C and 1.0s^{-1}, to various levels of strain.

Although the strain experienced in an industrial forging operation may be higher than 1.0, several studies had shown that the DRX grain size and volume fraction of DRX grains reached

steady state values prior to a strain of 1.0 [10, 11]. Therefore, given a defect-free microstructure at a strain of 1.0, it was presumed that the continual operation of DRX would prevent any additional microstructural damage from being incurred with further deformation. A grain size analysis was conducted on the offset ED samples deformed at 500°C and $1.0s^{-1}$, to various levels of strain. For ease of interpretation, the average grain areas obtained from image analysis were converted to average spatial diameters as per Annex A2 of ASTM E112–96 [45]. The average grain size and area fraction of grains under 20µm were determined for each case, and the results are shown in Figure 4-38. As suggested by the micrographs, it was evident from the grain size analysis that the average grain size decreased with strain. Furthermore, it was clear that the average grain size decreased rapidly at low levels of strain, but grain refinement had slowed at high strains (i.e. 0.50 and above). At the same time, the area fraction of grains under 20µm was observed to increase with strain. The decrease in average grain size was in agreement with the increase in area fraction of fine grains. Although a steady state area fraction was not observed, the result still suggested that DRX had occurred and had progressed with strain.

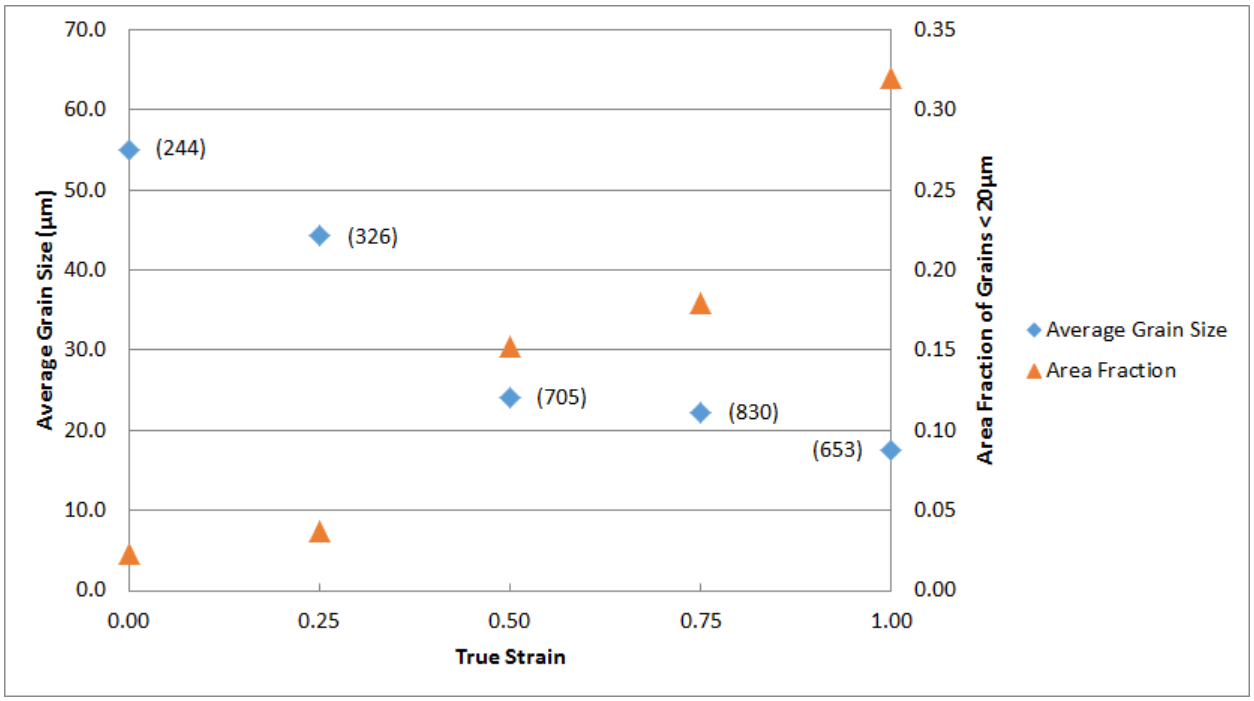

Figure 4-38: Average grain sizes and area fractions of grains < 20µm for offset ED samples deformed at 500°C and $1.0s^{-1}$ to various levels of strain (values in brackets indicate the number of grains analyzed).

4.3.3 Effect of Cooling Rate

After the dynamic evolution of microstructure had been investigated, the subsequent cooling of the forged sample and the associated changes in the microstructure had to be examined. A simple simulated cooling profile was determined by modelling the Ø63.5mm extruded rod, with the same aspect ratio as a Gleeble® sample, undergoing uniaxial compression at 500°C and $1.0s^{-1}$ to a final true strain of 1.0. To replicate a forging operation, the deformed disc was assumed to have been removed from the forging die immediately after forging and placed onto a semi-infinite steel bench for cooling. The cooling profile was simulated on the Gleeble® by simultaneously back heating and air quenching. Several conditions were examined: water quenched, simulated air cooling (as described above), die cooling (i.e. sample remained between hot, but cooling, anvils with no further heating), and a five minute hold at the forging temperature.

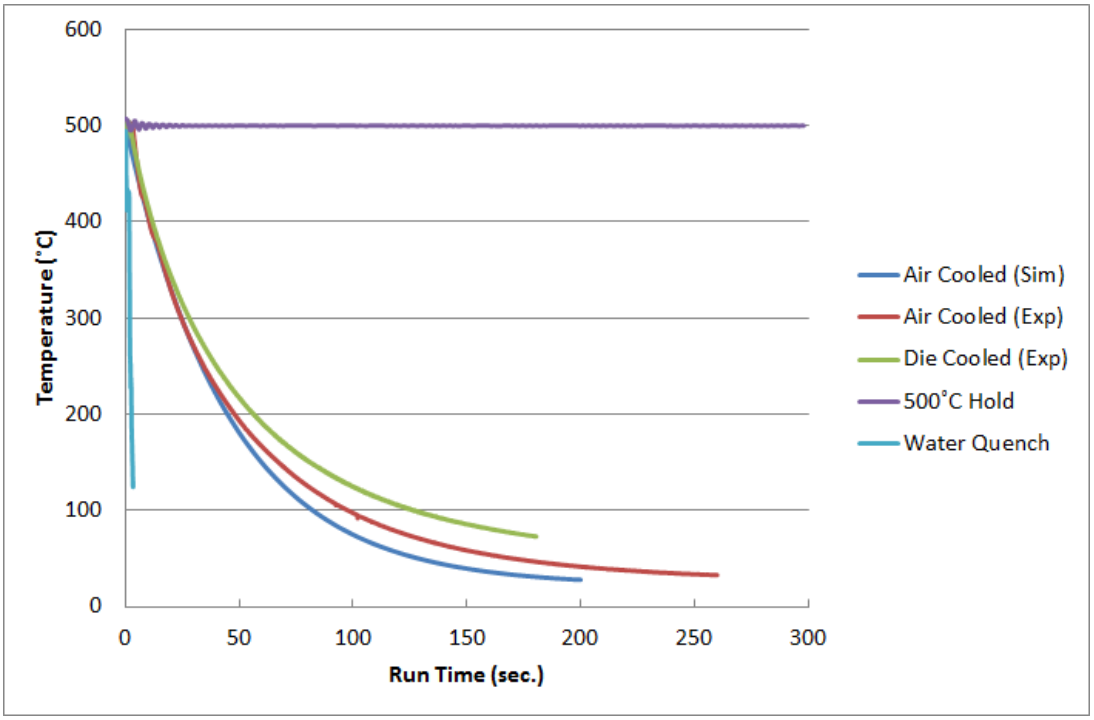

Figure 4-39: Temperature profiles for various post-deformation cooling conditions.

The simulated and experimentally obtained cooling profiles are shown in Figure 4-39. Despite the die cooled profile being quite similar to the air cooled case, three distinct cooling rates were obtained: a very high cooling rate (via water quench), an intermediate cooling rate (via air cooling or die cooling), and a very low cooling rate (via five minute hold). Offset TD samples

were deformed to a true strain of 1.0 for each cooling scenario, and the microstructures obtained after cooling are shown in Figure 4-40.

It was evident that the water quenched sample exhibited the finest grain structure, as the grains were not given sufficient time at high temperature for significant grain growth to occur. However, the water quenched microstructure exhibited the least homogeneity. On the contrary, the other three cooling rates exhibited more homogeneous microstructures, as a result of larger equiaxed grains. It was evident that the microstructures obtained from air and die cooling were quite similar to that of the five minute hold. The result suggested that grain growth occurred rapidly when the samples were still at relatively high temperatures (i.e. within the first 50 seconds of cooling) but had slowed drastically thereafter, resulting in very similar final microstructures.

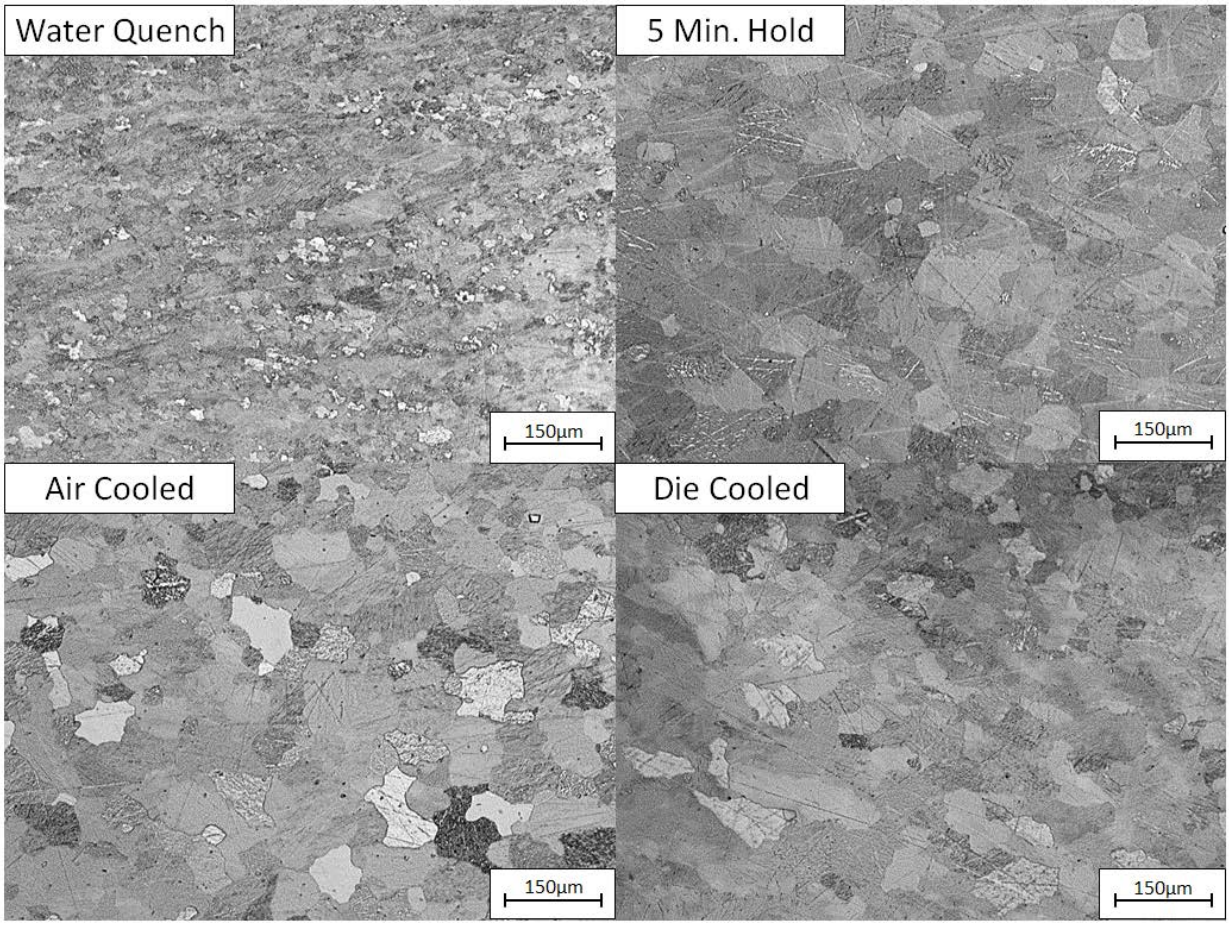

Figure 4-40: Micrographs of offset TD samples after deformation at 500°C and $1.0s^{-1}$, to a true strain of 1.0, and cooled under various conditions.

4.4 Material Processing Windows

4.4.1 Extruded Condition

With knowledge of the microstructures under various deformation conditions, the feasibility of using processing maps to identify viable processing windows was studied. The contours for power dissipation efficiency were included to evaluate their ability to predict the domains representing microstructural changes. The processing map developed using the flow stress data from twenty compression tests (i.e. one for each processing condition) of the offset ED samples is shown in Figure 4-41. The fractures that had occurred during deformation at 300°C for the two highest strain rates were captured accurately by the instability criterion proposed by Babu et al. [37]. The extremes of the observed high efficiency domains were examined and determined to be DRX domains. Microstructures of select deformation conditions are shown in Figure 4-42.

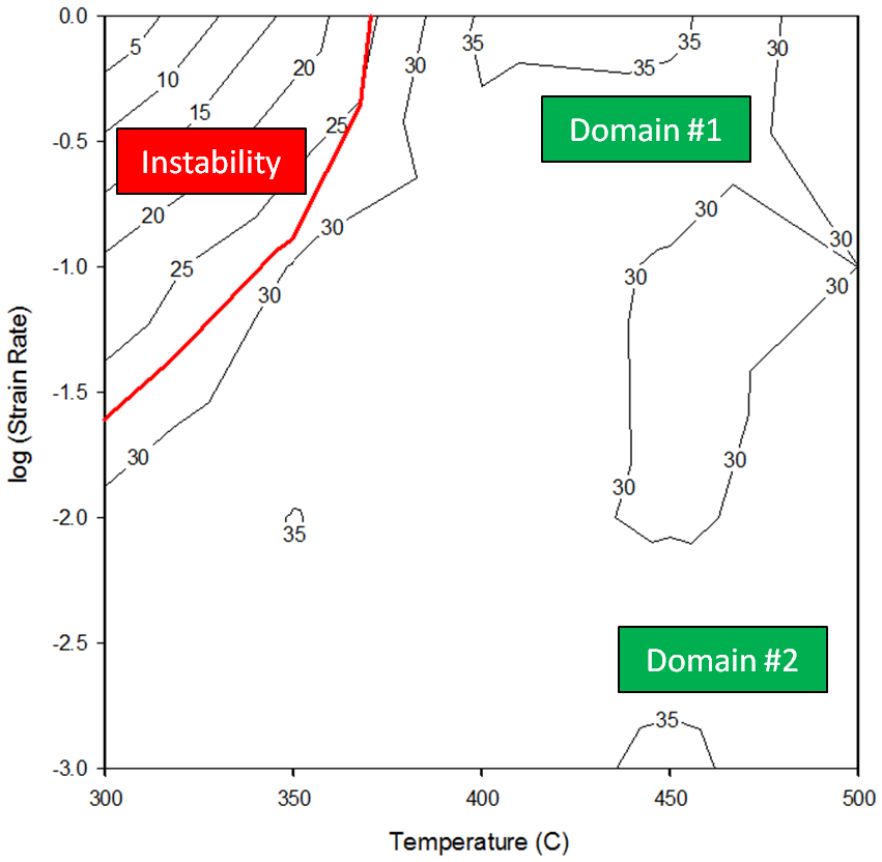

Figure 4-41: Processing map derived from the flow stress data of offset ED samples at a true strain of 0.40.

Although the maps were able to accurately predict the cracking and DRX domains, it was observed that the domains were very sensitive to changes in the flow stress. As a result of the numerical nature behind the derivation of such domains, a small change in the flow stress value extracted for one deformation condition was capable of producing or eliminating a nearby instability region. Considering that deformation at high temperatures and low strain rates resulted in very low flow stresses, it was determined that those conditions were most sensitive to changes in the flow stress. Any errors or bias in experimentation would have been masked in the flow stress data. Despite the limitation of the maps, it was evident that the extruded material exhibited a wide processing window, with DRX observed under all investigated conditions. The extruded material had undergone deformation up to a true strain of 1.2, at a strain rate of $1.0s^{-1}$ and a temperature of 500°C, with no observable damage to the microstructure.

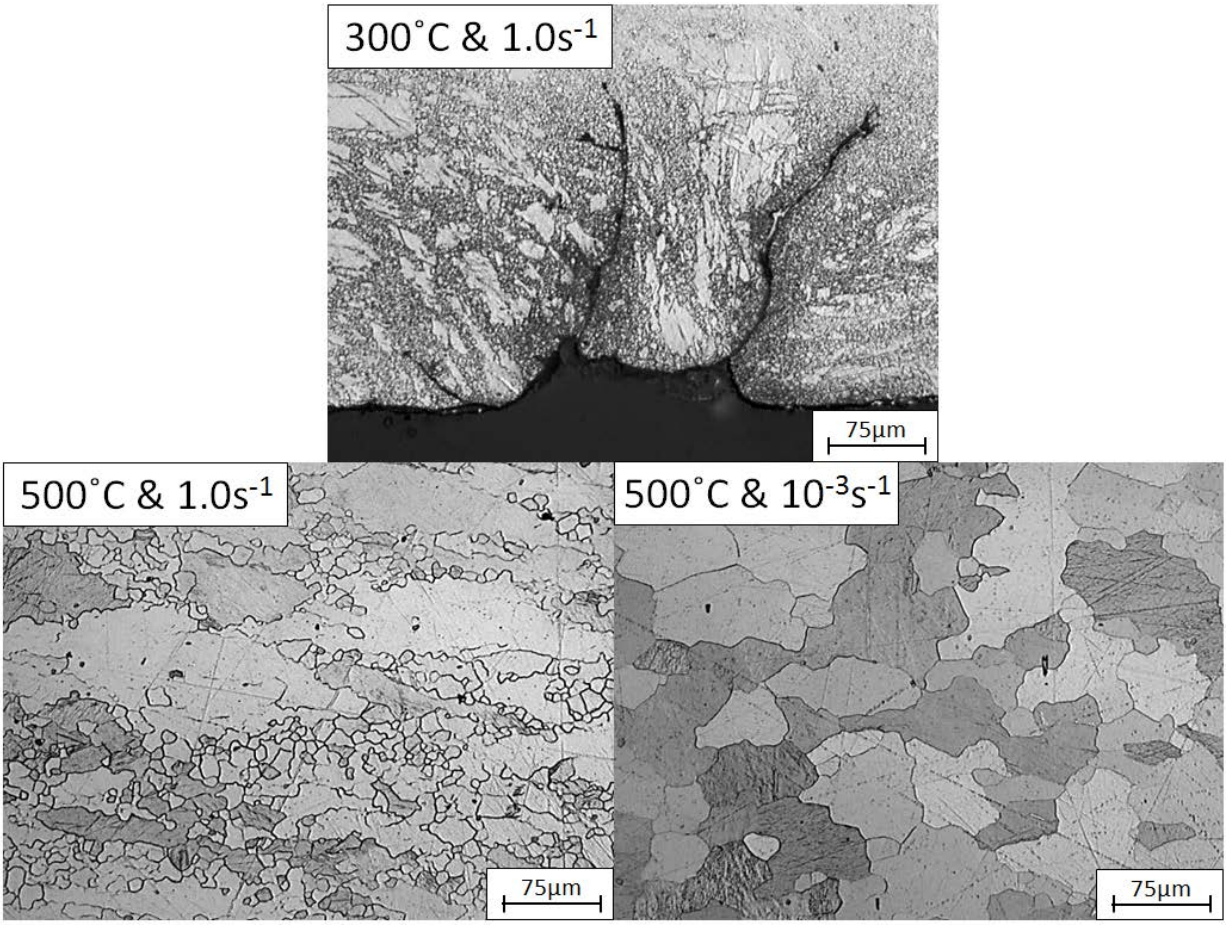

Figure 4-42: Micrographs of offset ED samples deformed to a true strain of 0.50, under various conditions.

4.4.2 As-Cast Condition

Although the extruded material provided a large processing window, the processing map developed from the flow stress curves of the as-cast samples revealed large regions of flow instability; the map is shown in Figure 4-43. Recall that macroscopic cracking was observed at a strain rate of $1.0s^{-1}$ for temperatures above 350°C; it was evident the instability region accurately captured the cracking regime. Microstructures were examined for select deformation conditions; the micrographs can be found in Figure 4-44.

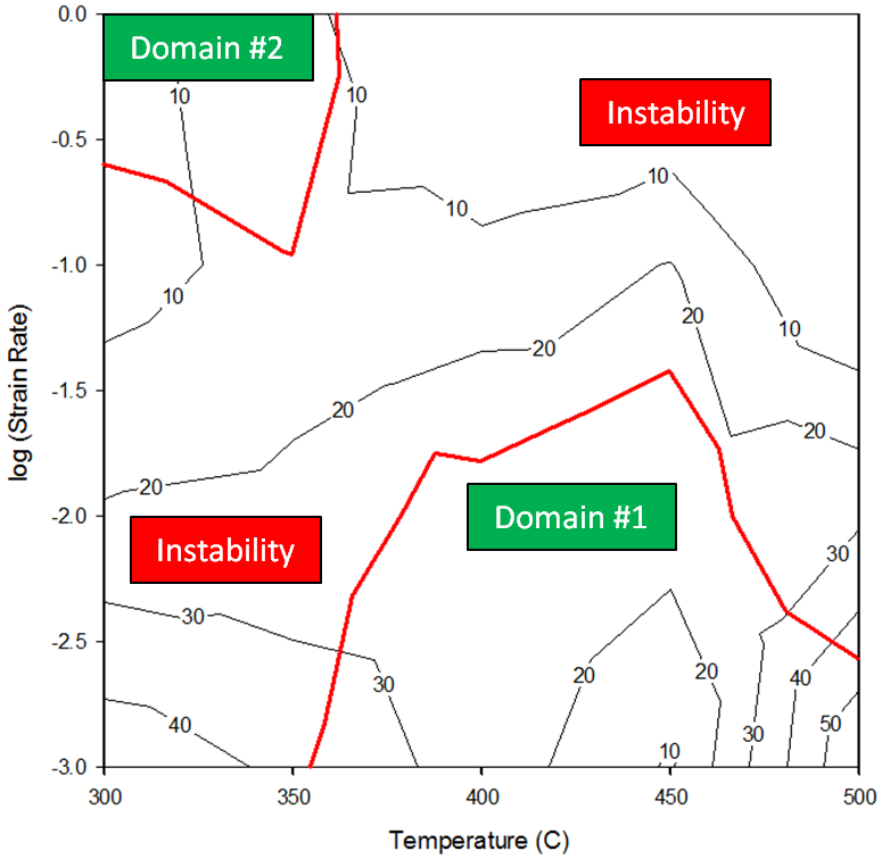

Figure 4-43: Processing map derived from the flow stress data of as-cast samples at a true strain of 0.40.

From the microstructure obtained after deformation at 300°C and $1.0s^{-1}$, it was evident the crack had formed at the boundary of the DRX and deformed regions due to strain incompatibility [16]. Furthermore, it was verified that deformation at 500°C and $10^{-3}s^{-1}$ produced large voids in the microstructure, albeit with the least number of defects. However, the low strain rate was deemed

to be too slow to be used in any industrial process. Both high efficiency domains were determined to be cracking regimes. It was evident that the as-cast processing map provided accurate predictions of microstructural changes that had occurred during deformation. With the above observations, it was determined that the as-cast condition did not exhibit any viable processing windows for a forging operation.

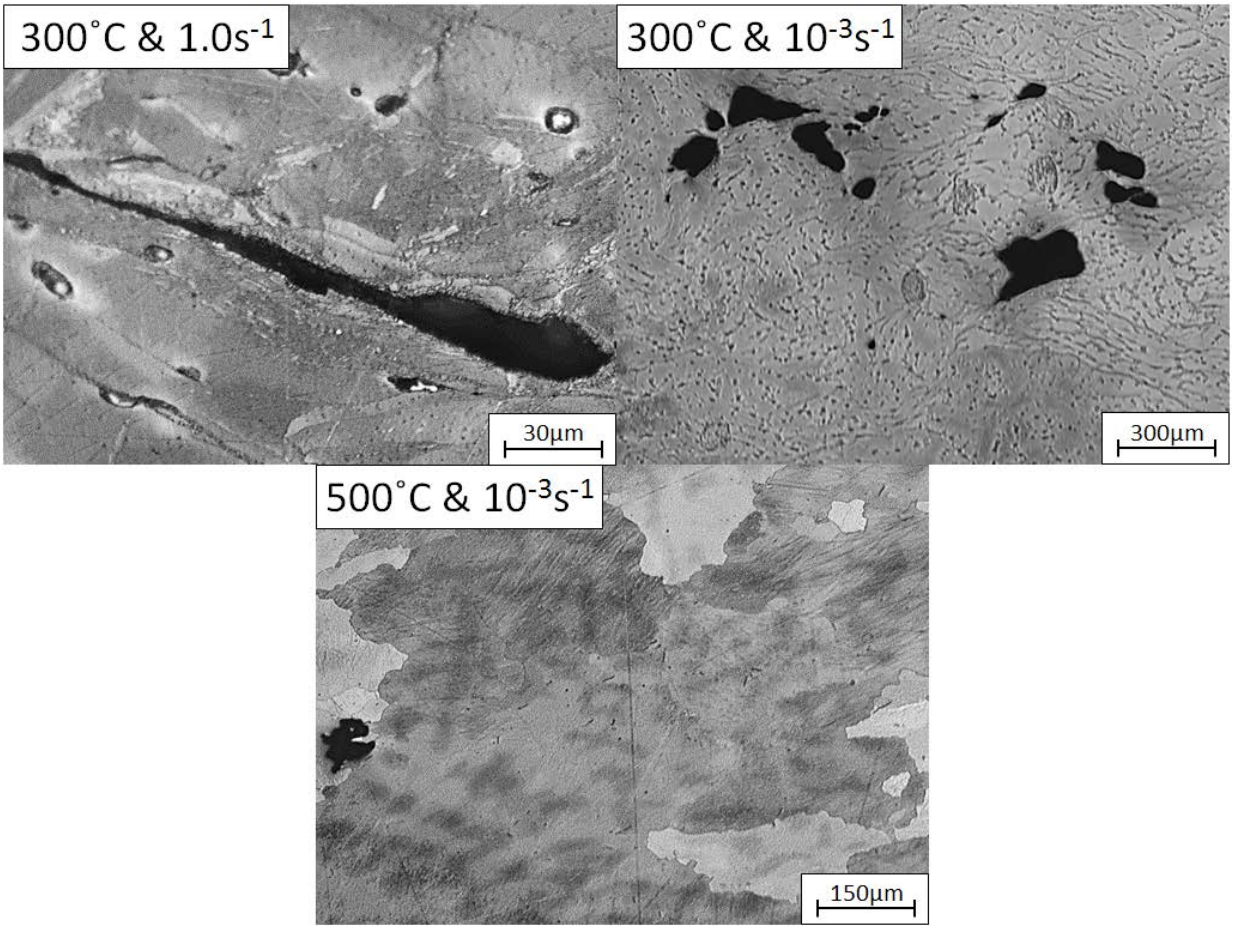

Figure 4-44: Micrographs of as-cast samples deformed to a true strain of 0.50, under various conditions.

4.4.3 Cast-Homogenized Condition

The processing map for the cast-homogenized condition differed significantly from that of the as-cast condition. The numerically derived instability regions were not as widespread as those seen in the as-cast processing map, and large regions of potentially safe processing conditions were observed. The processing map developed from the flow stress data of the cast-homogenized

samples is provided in Figure 4-45. Samples from both the unstable and stable regions were selected for metallography; the microstructures are shown in Figure 4-46. It was evident that deformation at low temperature and high strain rate resulted in twinning of select grains, and subsequent strain localization had occurred within the DRX region. By increasing the temperature and lowering the strain rate, DRX had readily occurred at the grain boundaries and not within the grains. It was evident that twinning had readily occurred at 350°C, but only in favourably oriented grains. Furthermore, the two high efficiency domains observed at 500°C were determined to be DRX domains, and processing could be conducted successfully with no damage to the microstructure. Although the microstructures obtained after deformation at 350°C and 450°C failed to verify the predicted instability regions, defects may have existed on planes differing from the ones examined. Alternatively, the numerically generated instability regions may have been artifacts of experimental error or bias masked in the flow stress data.

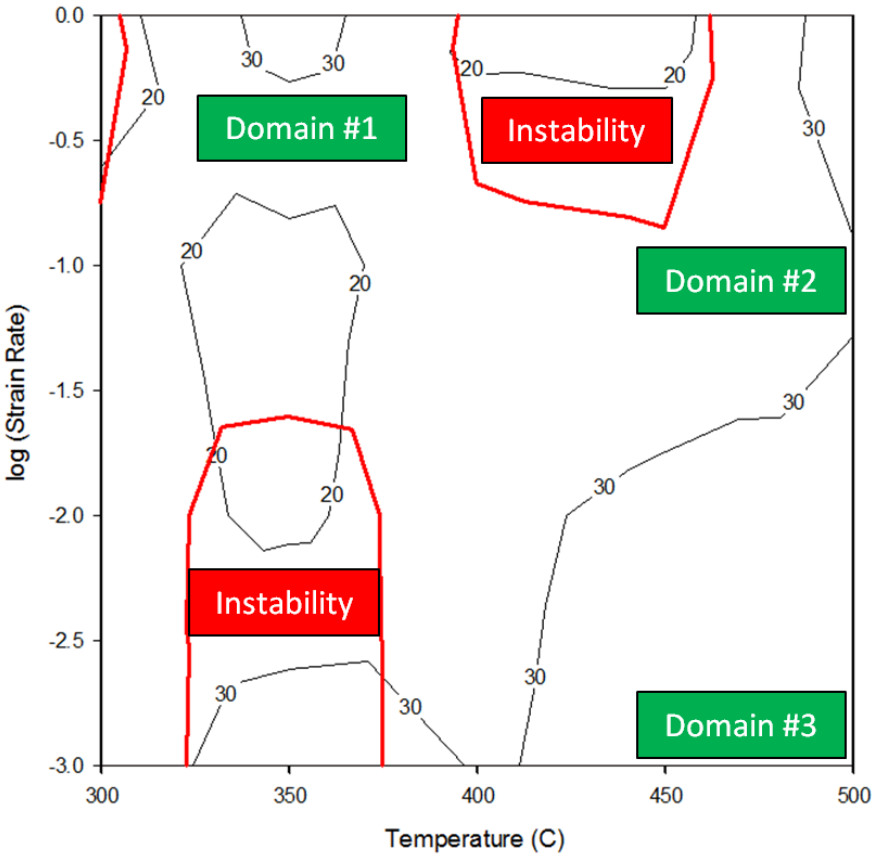

Figure 4-45: Processing map derived from the flow stress data of cast-homogenized samples at a true strain of 0.40.

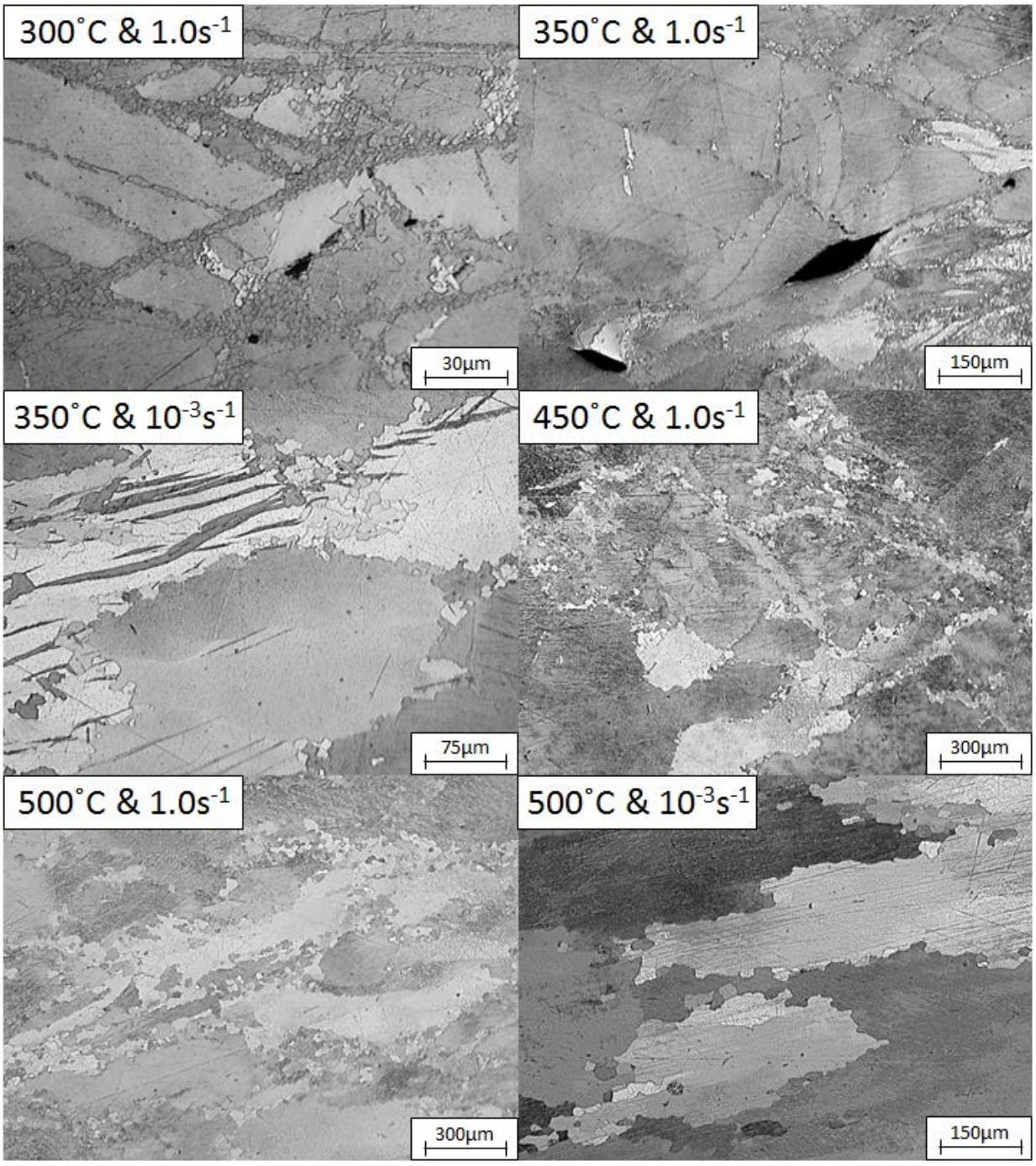

Figure 4-46: Micrographs of cast-homogenized samples deformed to a true strain of 0.50, under various conditions.

It was previously observed in the flow stress curves that yielding occurred at lower stresses when the deformation strain rate was increased. The softening was observed in the as-cast samples at 300°C for strain rates above $10^{-1}s^{-1}$, and for strain rates above $10^{-2}s^{-1}$ at temperatures below

400°C for the cast-homogenized condition. Examination of the microstructures revealed the presence of twins and/or strain localization within DRX regions, with cracks formed at the boundaries due to strain incompatibility [16]. The softening behaviour observed in the flow stress may be attributed to the activation of twins in favourably oriented grains, and subsequent strain localization and/or formation of internal cracks.

5.0 Conclusions

Isothermal uniaxial compression tests were conducted to study the forging behaviour of extruded, as-cast, and cast-homogenized AZ31B magnesium alloy. Although the open die upsetting operation, simulated through uniaxial compression, had differences from a closed die forging operation, the findings still provided insight on the relative workability of different starting conditions. The effects of thermal-mechanical processing condition, deformation strain, and post-deformation cooling rate on the microstructure were investigated. In addition, the effect of homogenization on the cast material was studied. Furthermore, the effectiveness of using processing maps to predict viable hot working conditions was evaluated.

During deformation of the extruded material, fractures occurred at 300°C for the two highest strain rates (i.e. $10^{-1}s^{-1}$ and $1.0s^{-1}$). In the as-cast material, large surface cracks were observed at temperatures above 350°C for the strain rate of $1.0s^{-1}$. However, workability was improved after homogenization at 450°C for five hours, as the cracks observed at high temperature and high strain rate were no longer present. The dendritic structure of the cast material was no longer visible after homogenization. Furthermore, melting of the $Mg_{17}Al_{12}$ phase, which resulted in the poor high strain rate workability, was suppressed after a furnace soak in the temperature range of 400°C to 500°C for five hours. Although closed die forgings take on the surface roughness of the dies, it was worth noting that open die upsetting produced a very rough surface on the cast material.

Flow stresses during deformation were observed to decrease with strain rate, and also with increasing deformation temperature. Stress-strain curves obtained from samples along the extrusion direction exhibited a tensile twinning signature when deformation was conducted at temperatures below 400°C and at strain rates above $10^{-2}s^{-1}$. Numerous twins were observed in the microstructure at low strain, but none were observed at higher strains. Compression along the transverse direction of the extrusion exhibited a comparatively low yield stress as a result of basal slip, but no tensile twinning signature was observed in the flow stress curve. Macroscopic shear bands, resulting in strain localization, were observed for deformation temperatures below 450°C at the two higher strain rates, and below 400°C at the two lower strain rates – these conditions should be avoided for bulk deformation processes. After homogenization of the cast

material, flow stresses were lower compared to their as-cast counterparts. However, due to the activation of twins in favourably oriented grains, low yield stresses were observed at temperatures below 400°C and strain rates above $10^{-2}s^{-1}$. Although homogenization had proved to be beneficial for the cast material, no differences in the microstructures or flow stress behaviours were observed when the extruded material was annealed at 450°C for three hours. However, the finding suggested that a furnace soak time under said conditions would not result in any significant changes in the deformation behaviour of the extruded material.

Compression tests conducted on the extruded material resulted in elliptical cross-sections, as a result of the initial axisymmetric fiber texture in the extruded rod. It was confirmed that the initial texture had led to preferential material flow in specific crystallographic directions, and was dependent on the direction of loading. The anisotropy observed during compression along the extrusion direction was attributed to tensile twinning at low temperature, and pyramidal slip at high temperature. Furthermore, the anisotropy was observed to increase with deformation strain rate, as a result of increased twinning activity and accelerated grain rotation. Near circular cross-sections were obtained when deformation was conducted at the lowest strain rate of $10^{-3}s^{-1}$. The anisotropy and low yield stress observed in the transverse direction was attributed to the lack of texture uniformity in the compression sample, and the occurrence of basal slip at low deformation temperatures. With the activation of pyramidal slip at higher temperatures, anisotropy was greatly reduced. Unlike the samples along the extrusion direction, samples in the transverse direction showed near circular cross-sections when deformation was conducted at 500°C and $1.0s^{-1}$. Compression tests conducted on the samples along the centreline of the extrusion, as well as on the as-cast and cast-homogenized conditions, showed no anisotropy of flow.

Although dynamic recrystallization was observed under all investigated processing conditions, the extent of DRX varied greatly under different conditions. The size and volume fraction of the DRX grains were observed to increase with deformation temperature and also with decreasing strain rate. Therefore, as a result of longer times at high temperature, deformation conducted at the highest temperature and lowest strain rate resulted in the greatest microstructural homogeneity. In both the extruded and cast materials, an increase in the volume fraction of DRX grains was observed with increasing strain. Comparing the two materials, deformed to the same

strain and under the same processing condition, it was observed that the extruded samples exhibited higher volume fractions of DRX grains; however the DRX grain sizes were similar for the two materials. The finer initial grain size observed at the centre of the extruded rod resulted in lower flow stresses during deformation and rapid grain growth occurred during heating. However, the resultant microstructure after deformation was very similar to that observed in samples extracted from an offset location in the extruded rod. With the cast-homogenized material, it was shown that increasing the deformation temperature from 350°C to 500°C had the benefit of increasing the maximum allowable strain during bulk deformation, without the presence of surface cracks.

The influence of post-deformation cooling rate on the microstructure was studied by conducting compression tests at 500°C and $1.0s^{-1}$, followed by a water quench, air/die cooling, or a five minute hold at the deformation temperature. It was observed that the water quenched sample consisted of the finest grain structure; however it was also the least homogeneous. The intermediate and low cooling rates resulted in very similar microstructures. The result suggested that the rapid grain growth occurred shortly (i.e. within the first 50 seconds) after deformation had completed, and longer times spent at high temperature had little to no impact on the final microstructure.

The processing maps derived from the hot compression flow stress curves revealed regimes of flow instability and domains of high power dissipation efficiency. The processing map for the extruded material showed good consistency between the numerically predicted domains and the experimental results. The cracks observed during deformation at low temperature and high strain rate were accurately predicted by the flow instability regime, and the safe processing window was also accurately captured. The processing map for the as-cast condition exhibited large regimes of flow instability. Select conditions were verified with metallography, and the flow instability regimes were confirmed. The high efficiency domains observed in the processing map proved to be cracking domains; thus, no viable processing conditions were observed for the as-cast condition. However, it was evident that the numerically derived regimes of flow instability were very sensitive to input data; a small change in the flow stress extracted for a specific deformation condition was capable of producing or eliminating nearby regimes of flow instability. Therefore, it was evident that extensive metallographic examination would be

required to verify each processing condition against the predictions of the processing map. Compared to the as-cast condition, the processing map for the cast-homogenized condition revealed less widespread flow instability regimes. Deformation at 500°C had produced no microstructural defects and the results were in agreement with the processing map. However, certain instability regimes predicted by the processing map could not be verified with metallography. Differences between the processing map predictions and microstructural observations were attributed to the numerical nature of the maps, and associated masking of experimental error. Alternatively, microstructural artifacts of interest may not have been present in the plane of metallographic examination. Although the processing maps were able to predict certain instability regimes and DRX domains, the observations also revealed the inadequacies associated with applying such a numerical approach to predicting all physical phenomena occurring within a dynamic process. Numerous repetitions and extensive metallographic examination would be required to verify each predicted domain.

With consideration to economically feasible production rates in an industrial application, one processing condition was found to be viable for both the extruded and cast-homogenized materials. Deformation was successfully conducted at 500°C and $1.0s^{-1}$, to a true strain of 1.0, with both materials; however, the volume fraction of DRX grains was higher in the extruded material. The corresponding microstructures revealed no undesirable traits, and the condition had proved to be viable for an industrial forging operation. Furthermore, deformation of the extruded material was successfully conducted at 450°C, to a true strain of 0.5, without the presence of shear bands. Although unsupported by the cast-homogenized processing map, it should be noted that deformation was also successfully conducted at 450°C, to a final strain of 0.5, with no observable damage to the microstructure.

To improve on the comprehensiveness of the study, several additional studies could be conducted to further investigate the high temperature deformation behaviour of AZ31B. Firstly, both extruded and cast-homogenized materials should be deformed to higher strain (i.e. up to a true strain of 3.0 – consistent with that observed in forging) to verify the workability of the material under the proposed processing conditions. Secondly, additional DSC studies should be conducted to optimize the key parameters (i.e. temperature and time profile) for homogenization of the as-cast material. To improve the accuracy of the DSC studies, the tests should be

conducted with pure magnesium as the baseline reference (i.e. in place of the empty crucible), and a new baseline reference should be established prior to each test. Lastly, to fully understand the anisotropy of the forged component, the evolution of texture during deformation, as well as during cooling after deformation, should be studied with XRD for both the extruded and cast-homogenized materials.

References

[1] S. Housh and B. Mikucki, "Selection and Application of Magnesium and Magnesium Alloys, Properties and Selection," in *ASM Handbook*, vol. 2, ASM International, 1990, pp. 455-479.

[2] H. E. Friedrich and B. L. Mordike, Eds., Magnesium Technology: Metallurgy, Design Data, Applications, Berlin: Springer, 2004.

[3] A. Chapuis and J. H. Driver, "Temperature Dependency of Slip and Twinning in Plane Strain Compressed Magnesium Single Crystals," *Acta Materialia*, vol. 59, pp. 1986-1994, 2010.

[4] W. Soboyejo, Mechanical Properties of Engineered Materials, New York: Marcel Dekker, Inc., 2003.

[5] E. Emley, Principles of Magnesium Technology, Oxford: Pergamon Press Ltd., 1966.

[6] T. Al-Samman and G. Gottstein, "Room temperature formability of a magnesium AZ31 alloy: Examining the role of texture on the deformation mechanisms," *Materials Science & Engineering: A,* vol. 488, pp. 406-414, 2008.

[7] C. S. Roberts, Magnesium and Its Alloys, New York: John Wiley & Sons, Inc., 1960.

[8] Y. Kwon, Y. Lee, S. Kim and J. Lee, "Effect of Initial Microstructure on Hot Forging of Mg Alloys," *International Journal of Modern Physics B,* vol. 22, no. 31-32, pp. 6064-6069, 2008.

[9] F. Humphreys and M. Hatherly, Recrystallization and Related Annealing Phenomena, Kidlington: Elsevier Ltd., 2004.

[10] X. Yang, H. Miura and T. Sakai, "Dynamic Evolution of New Grains in Magnesium Alloy AZ31 during Hot Deformation," *Materials Transactions,* vol. 44, pp. 197-203, 2003.

[11] S. Fatemi-Varzaneh, A. Zarei-Hanzaki and H. Beladi, "Dynamic Recrystallization in AZ31 Magnesium Alloy," *Materials Science & Engineering A,* vol. 456, pp. 52-57, 2007.

[12] T. Al-Samman and G. Gottstein, "Dynamic Recrystallization During High Temperature Deformation of Magnesium," *Materials Science & Engineering A,* vol. 490, pp. 411-420, 2008.

[13] M. Barnett, A. Beer, D. Atwell and A. Oudin, "Influence of Grain Size on Hot Working Stresses and Microstructures in Mg-3Al-1Zn," *Scripta Materialia,* vol. 51, pp. 19-24, 2004.

[14] A. Beer and M. Barnett, "Microstructural Development during Hot Working of Mg-3Al-1Zn," *Metallurgical and Materials Transactions A,* vol. 38, no. A, pp. 1856-1867, 2007.

[15] D. Sun, C. Chang and P. Kao, "Microstructural Study of Strain Localization in Hot Compressed Mg-3Al-1Zn," *Materials Science & Engineering A,* vol. 527, pp. 7050-7056, 2010.

[16] H. Kim, J. Lee, C. Lee, W. Bang, S. Ahn and Y. Chang, "Shear Band Formation during Hot Compression of AZ31 Mg Alloy Sheets," *Materials Science & Engineering A,* vol. 558, pp. 431-438, 2012.

[17] E. Yukutake, J. Kaneko and M. Sugamata, "Anisotropy and Non-Uniformity in Plastic Behaviour of AZ31 Magnesium Alloy Plates," *Materials Transaction,* vol. 44, no. 4, pp. 452-457, 2003.

[18] B. H. Lee, S. H. Park, S.-G. Hong, K.-T. Park and C. S. Lee, "Role of Initial Texture on the Plastic Anisotropy of Mg-3Al-1Zn Alloy at Various Temperatures," *Materials Science & Engineering A,* vol. 528, pp. 1162-1172, 2011.

[19] Q. Dai, D. Zhang and X. Chen, "On the Anisotropic Deformation of AZ31 Mg Alloy Under Compression," *Materials and Design,* vol. 32, pp. 5004-5009, 2011.

[20] K. Rao, Y. Prasad and K. Suresh, "Anisotropy of Flow During Isothermal Forging of Rolled AZ31B Magnesium Alloy Rolled Plate in Three Orthogonal Directions: Correlation with Processing Maps," *Materials Science & Engineering A,* vol. 558, pp. 30-38, 2012.

[21] Y. Prasad and K. Rao, "Hot Workability, Microstructural Control and Rate-Controlling Mechanisms in Cast-Homogenized AZ31 Magnesium Alloy," *Advanced Engineering Materials,* vol. 11, no. 3, pp. 182-188, 2009.

[22] Y. Prasad and K. Rao, "Effect of Homogenization on the Hot Deformation Behaviour of Cast AZ31 Magnesium Alloy," *Materials and Design,* vol. 30, pp. 3723-3730, 2009.

[23] T. Murai, S.-i. Matsuoka, S. Miyamoto and Y. Oki, "Effects of Extrusion Conditions on Microstructure and Mechanical Properties of AZ31B Magnesium Alloy Extrusions," *Journal of Materials Processing Technology,* vol. 141, no. 2, pp. 207-212, 2003.

[24] J. Mohammadi, M. Ghoreishi and Y. Behnamian, "An Investigation into the Dissolution Characteristics of Gamma Precipitates in Mg-3Al-Zn Alloy," *Materials Research,* vol. 17, no. 4, pp. 996-1002, 2014.

[25] G. Bajargan, G. Singh, D. Sivakumar and U. Ramamurty, "Effect of Temperature and Strain Rate on the Deformation Behavior and Microstructure of a Homogenzed AZ31 Magnesium Alloy," *Materials Science & Engineering A,* vol. 579, pp. 26-34, 2013.

[26] M. Perez-Prado and O. Ruano, "Texture Evolution During Annealing of Magnesium AZ31 Alloy," *Scripta Materialia,* vol. 46, pp. 149-155, 2002.

[27] S. Yi, H.-G. Brokmeier and D. Letzig, "Microstructural Evolution during the Annealing of an Extruded AZ31 Magnesium Alloy," *Journal of Alloys and Compounds,* vol. 506, pp. 364-371, 2010.

[28] M. Li, Y. Ping, Z. Zude and M. Weimin, "An OIM Analysis on the Deformation Mechanism in Hot Compressed AZ31 Magnesium Alloy," *Materials Science Forum,* Vols. 488-489, pp. 633-636, 2005.

[29] B.-s. Wang, R.-l. Xin, G.-j. Huang, X.-p. Chen and Q. Liu, "Hot-Deformation Behaviors of AZ31 Alloys with Different Initial States," *Transactions of Nonferrous Metals Society of China,* vol. 18, pp. 145-149, 2008.

[30] X.-y. Yang, Z.-s. Ji, H. Miura and T. Sakai, "Dynamic Recrystallization and Texture Development during Hot Deformation of Magnesium Alloy AZ31," *Transactions of Nonferrous Metals Society of China,* vol. 19, pp. 55-60, 2009.

[31] M. R. Barnett, "Quenched and Annealed Microstructures of Hot Worked Magnesium AZ31," *Materials Transactions,* vol. 44, no. 4, pp. 571-577, 2003.

[32] X. Yang, H. Miura and T. Sakai, "Isochronal Annealing Behaviour of Magnesium Alloy AZ31 after Hot Deformation," *Materials Transactions,* vol. 46, no. 12, pp. 2981-2987, 2005.

[33] X.-y. Yang, Y.-k. Zhu, H. Miura and T. Sakai, "Static Recrystallization Behavior of Hot-Deformed Magnesium Alloy AZ31 during Isothermal Annealing," *Transactions of Nonferrous Metals Society of China,* vol. 20, pp. 1269-1274, 2010.

[34] Y. Prasad and S. Sasidhara, Hot Working Guide: A Compendium of Processing Maps, Materials Park: ASM International, 1997.

[35] Y. Prasad, "Processing Maps: A Status Report," *Journal of Materials Engineering and Performance,* vol. 12, pp. 638-645, 2003.

[36] Y. Prasad and K. Rao, "Hot Deformation Mechanisms and Microstructural Control in High-Temperature Extruded AZ31 Magnesium Alloy," *Advanced Engineering Materials,* vol. 9, no. 7, pp. 558-565, 2007.

[37] N. Babu, S. Tiwari and B. Nageswara Rao, "Modified Instability Condition for Identification of Unstable Metal Flow Regions in Processing Maps of Magnesium Alloys," *Materials Science and Technology,* vol. 21, pp. 976-984, 2005.

[38] J. Luan, C. Sun, X. Li and Q. Zhang, "Constitutive Model for AZ31 Magnesium Alloy Based on Isothermal Compression Test," *Materials Science and Technology,* vol. 30, no. 2, pp. 211-219, 2014.

[39] Z. Zhang, Q. Le and J. Cui, "Structure and Mechanical Properties of AZ31 Magnesium Alloy Billets by Different Hot-Top Semi-Continuous Casting Technology," *Rare Metals,* vol. 30, no. 4, pp. 414-418, 2011.

[40] "ImageJ," National Institutes of Health, 2004. [Online]. Available: https://imagej.nih.gov/ij/.

[41] I. Robertson, J. Lambros and A. Beaudoin, "Determining the mechanical constitutive properties of metals as a function of strain rate and temperature: A combined experimental and modeling approach," US Department of Energy, Office of Scientific and Technical Information, 2004.

[42] "FactSage," CRCT - ThermFact Inc. & GTT-Technologies, 2015. [Online]. Available: http://www.factsage.com/.

[43] R. M. Saeed, J. Schlegel, C. Castano and R. Sawafta, "Uncertainty of Thermal Characterization of Phase Change Material by Differential Scanning Calorimetry Analysis," *International Journal of Engineering Research & Technology,* vol. 5, no. 1, 2016.

[44] Q. Miao, L. Hu, X. Wang and E. Wang, "Grain Growth Kinetics of a Fine-grained AZ31 Magnesium Alloy Produced by Hot Rolling," *Journal of Alloys and Compounds,* vol. 493, pp. 87-90, 2010.

[45] "E112-96 Standard Test Methods for Determining Average Grain Size," ASTM International, 2004.

APPENDIX A: Engineering Drawings for Compression Samples

Cylindrical samples, Ø10mm by 15mm, were extracted from Ø63.5mm extruded rods and Ø304.8mm as-cast ingots of AZ31 for uniaxial compression. Samples with the compression axis oriented along the extrusion direction have been termed “ED” samples, and samples with the compression axis oriented along the radial direction have been termed “TD” samples. In some cases, scribe lines were marked in known orientations to observe the material flow. Furthermore, small scale samples were produced to observe the impact of texture uniformity.

The engineering drawings created for the machining of the various samples are provided in the following figures. The drawings illustrate the sample locations and orientations, as well as the associated manufacturing tolerances.

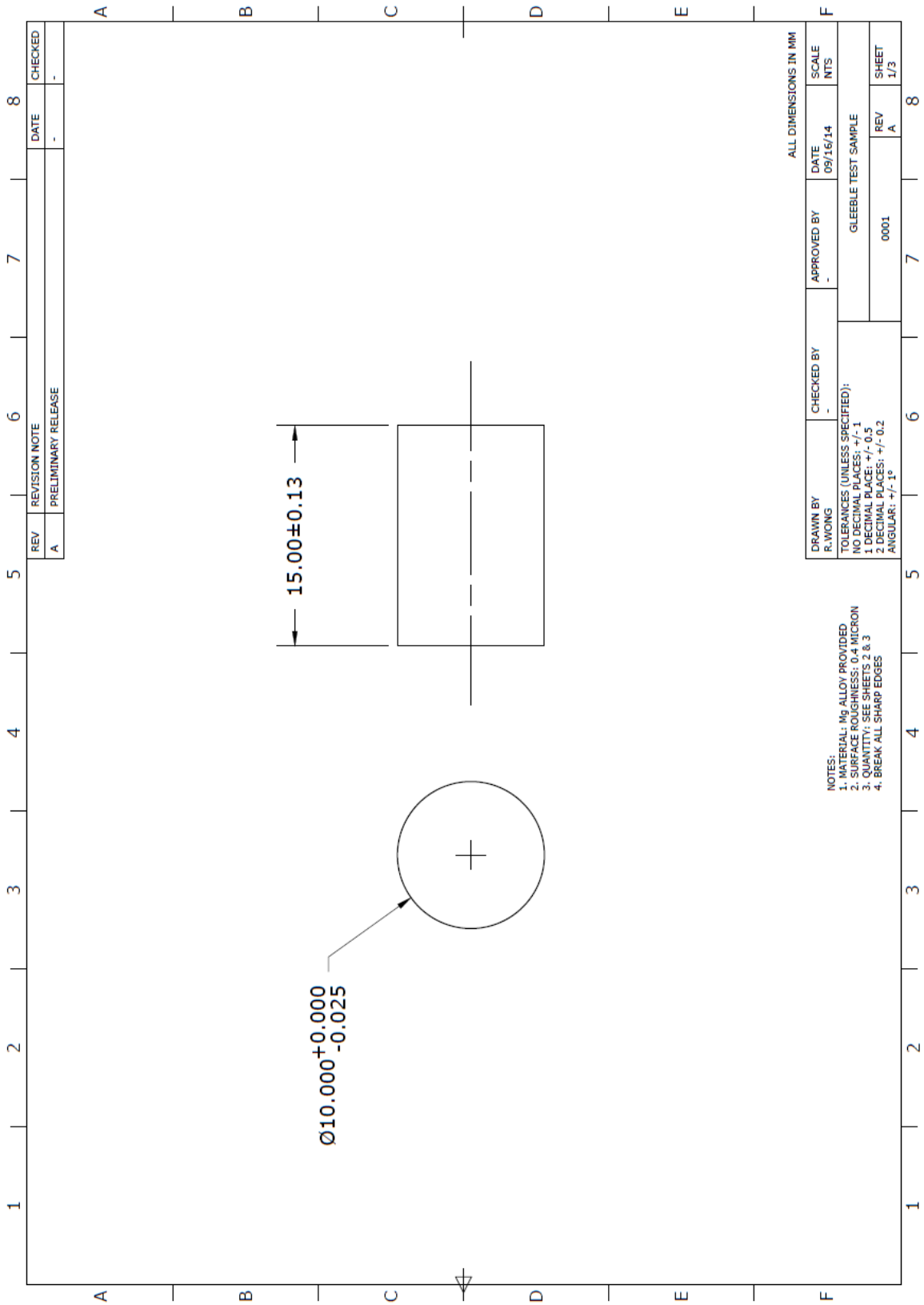

Figure A-1: Engineering drawing for standardized compression sample.

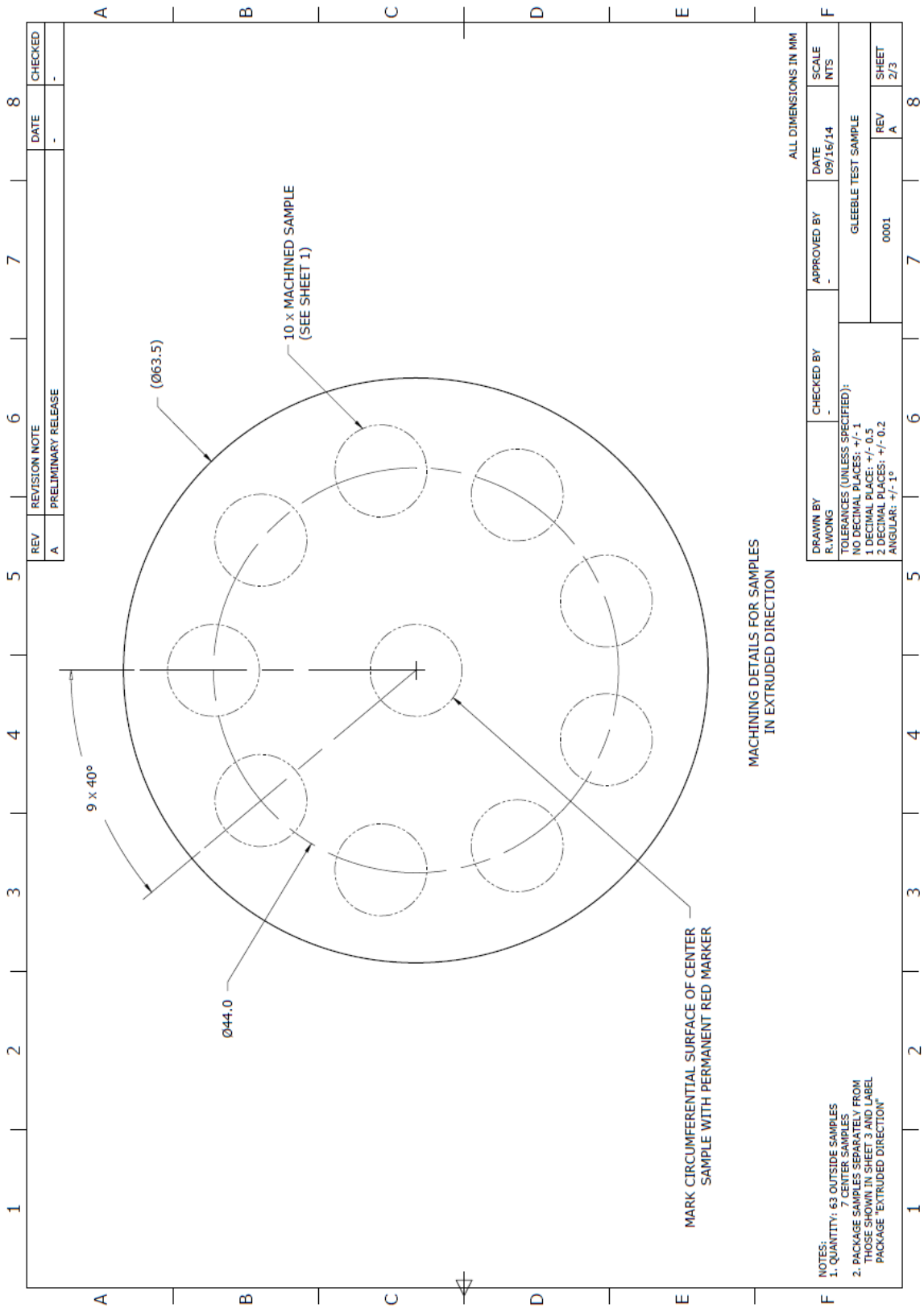

Figure A-2: Engineering drawing for ED compression samples.

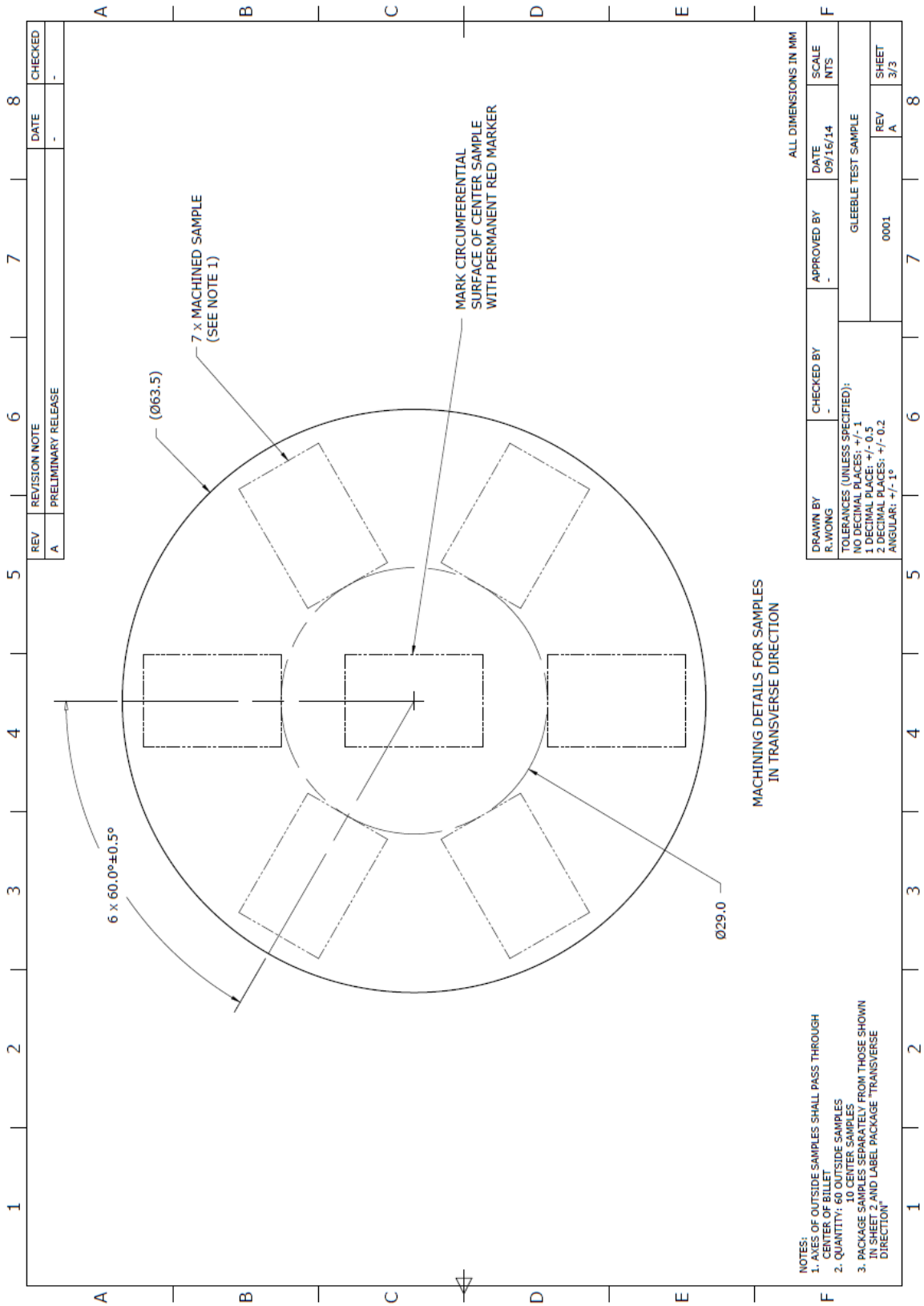

Figure A-3: Engineering drawing for TD compression samples.

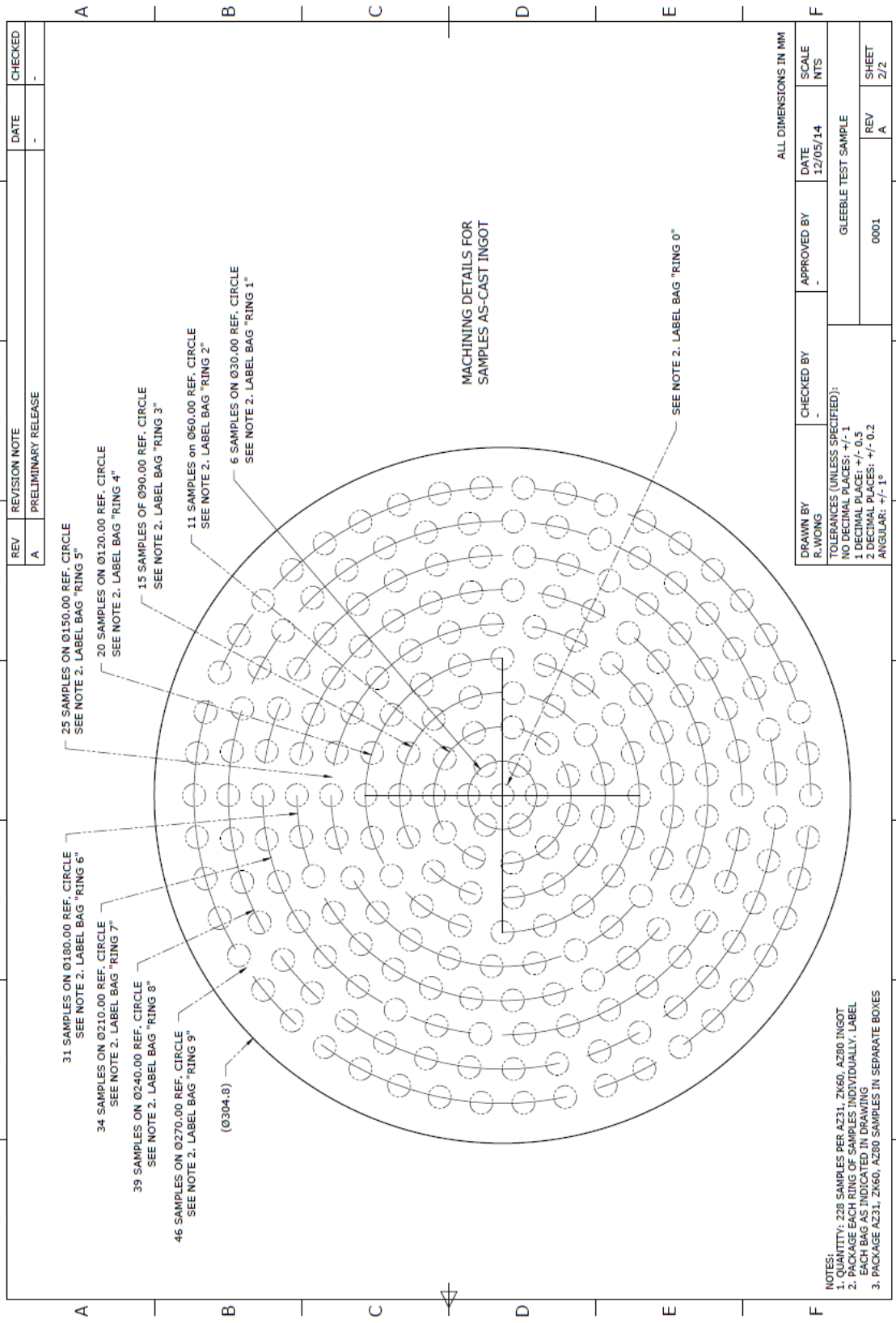

Figure A-4: Engineering drawing for as-cast compression samples.

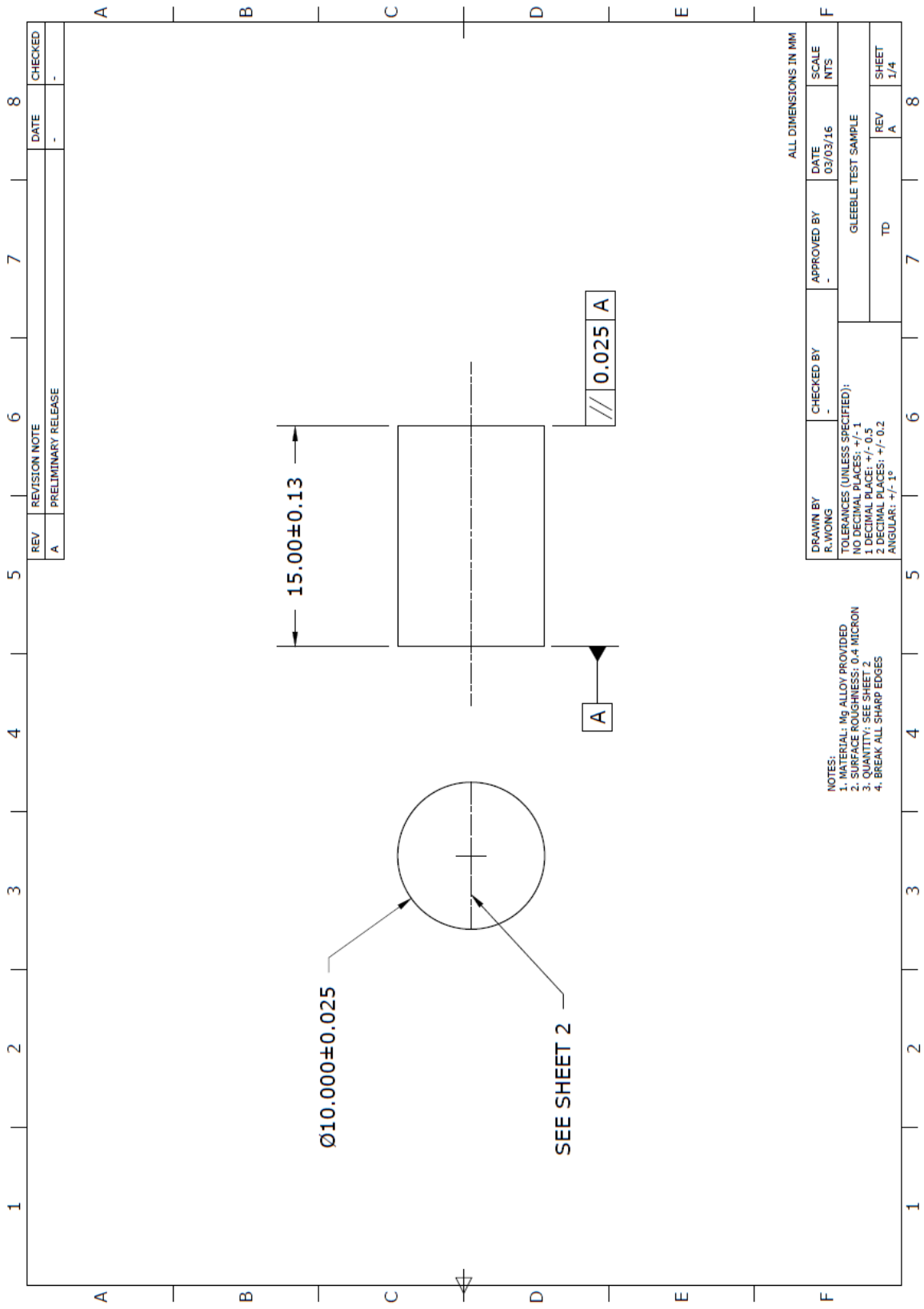

Figure A-5: Engineering drawing for scribed compression sample.

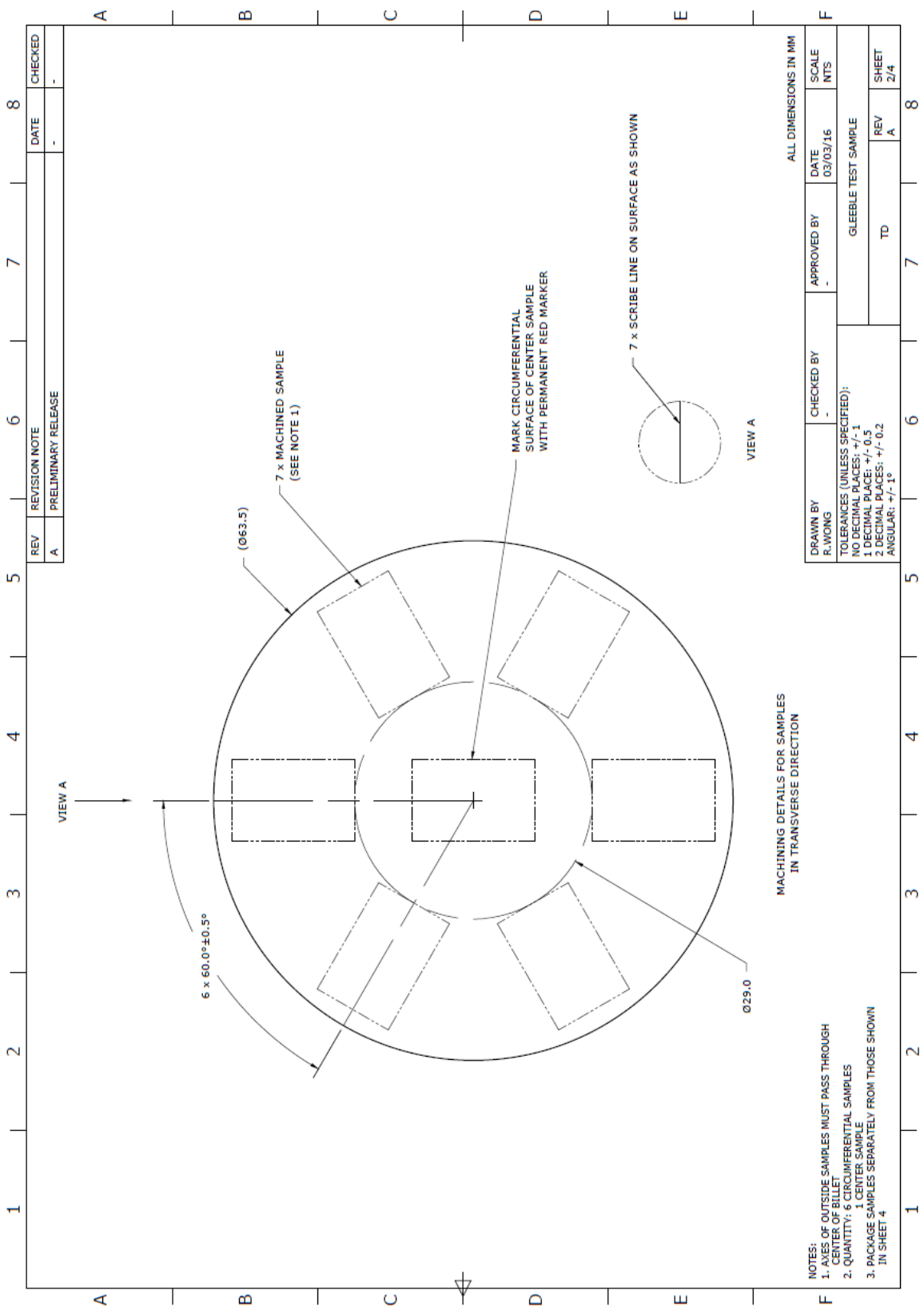

Figure A-6: Engineering drawing for scribed TD compression samples.

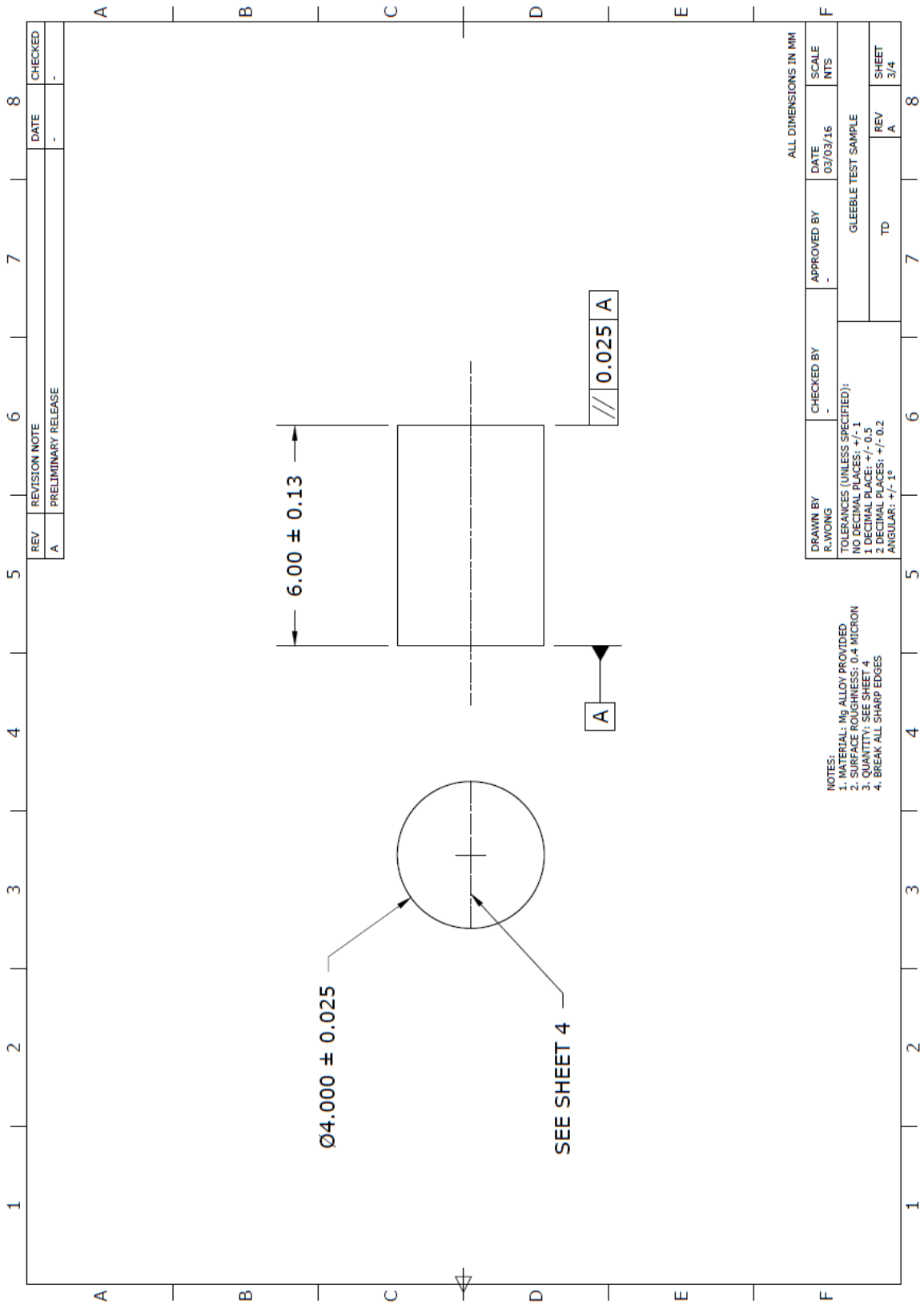

Figure A-7: Engineering drawing for scaled compression sample.

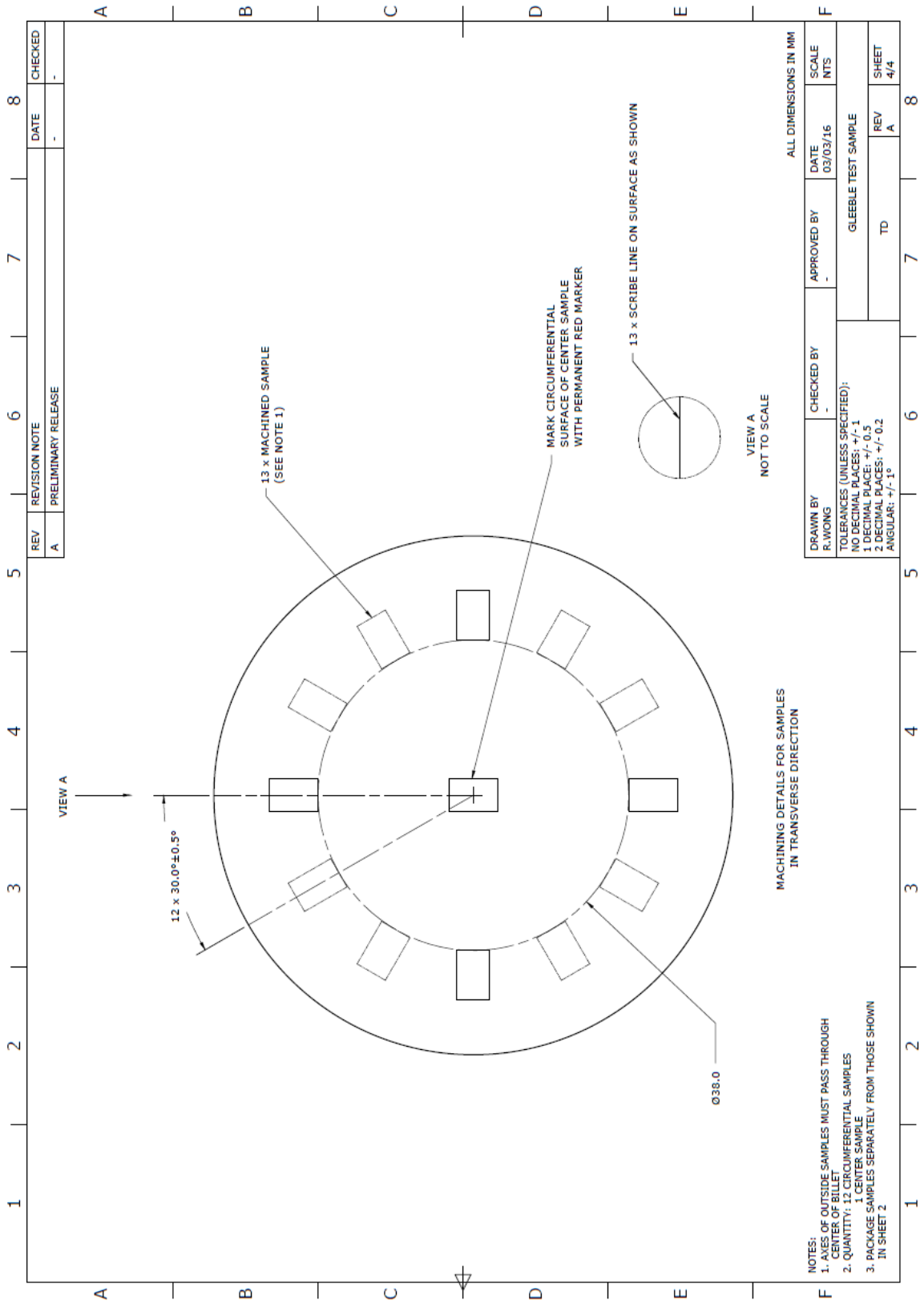

Figure A-8: Engineering drawing for scaled TD compression samples.

APPENDIX B: Room Temperature Formability of AZ31B

The importance of elevated temperature forming of magnesium alloys was understood by examining room temperature formability. The stress-strain curves from uniaxial compression of AZ31B, corrected using standard true stress and true strain equations, for the extrusion direction (ED) and transverse direction (TD) of an extruded rod, as well as for an as-cast (AC) condition are shown in Figure B-1. It was evident that the samples failed catastrophically at relatively low strains. Therefore, it was clear that bulk deformation processes like forging must be conducted at elevated temperatures.

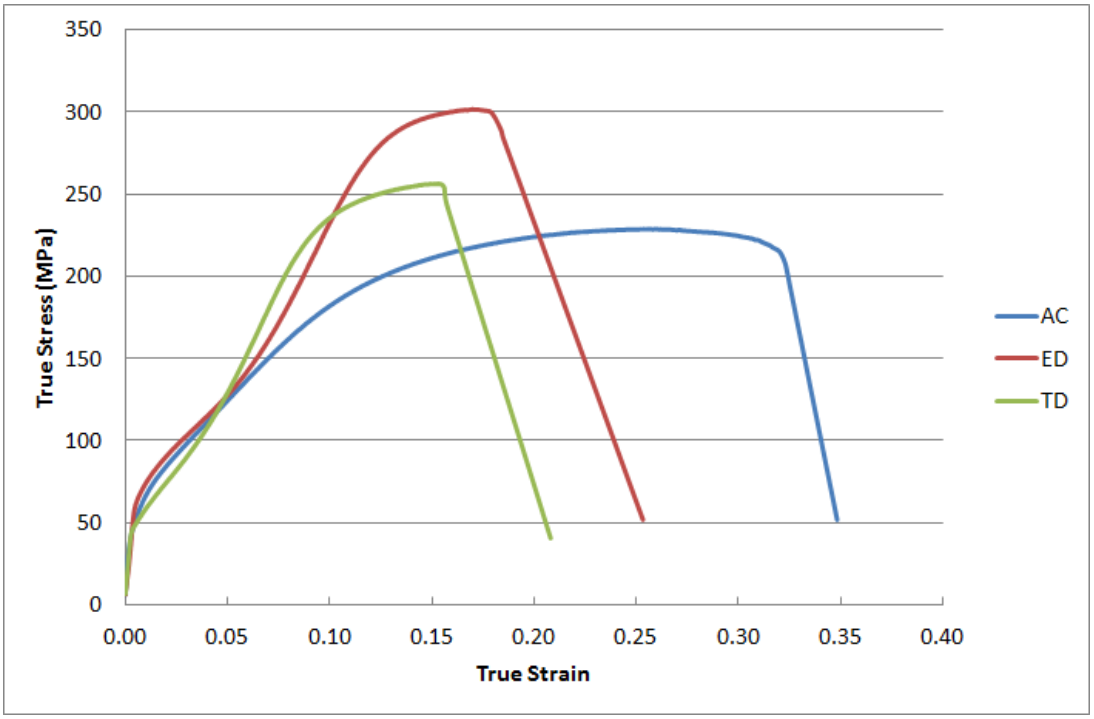

Figure B-1: Room temperature stress-strain curves for AZ31B.

APPENDIX C: Metallographic Procedure

The metallographic procedure utilized in sample preparation for optical microscopy is outlined below. Grinding of each compression sample to a depth close to the midplane, and parallel to the compression axis, was performed on 180 grit grinding paper. The height of the sample was recorded and the associated depth to the exact midplane was determined. The sample was cold mounted in epoxy (Struers EpoFix) and given a minimum of twelve hours to cure.

Grinding

Rough grinding was conducted manually for each cold mounted sample on successive grits of grinding paper, with a constant supply of water. Starting with the roughest grit of 240, onto 320 grit and 400 grit, and finally to 600 grit, one minute was spent on each grinding step. Fine grinding was performed on an automatic grinding machine (Struers RotoPol), operating at 150 revolutions per minute, with grinding papers of 1200 and 2400 grit. One minute was spent on each step, with subsequent grinding on 2400 grit to reach the exact midplane of the sample.

Polishing

Three polishing steps were used to prepare the sample surface for optical microscopy. Each step involved the use of an alcohol-based lubricant (Struers DP-Lubricant Blue), a rinse in methanol after polishing and the sample was immediately dried using compressed air. For the first step, a three micron polycrystalline diamond spray (Struers DP-Spray P, 3µm) was used in conjunction with a wool pad (Struers MD-Mol) at 250 revolutions per minute on an automatic polisher (Struers LaboPol). The sample was polishing for eight minutes and cleaned. The second step involved polishing with one micron diamond spray (Struers DP-Spray P, 1µm) on a short synthetic nap pad (Struers MD-Nap) for 5 minutes, at 250 revolutions per minute. Final polishing was performed by hand until a scratch-free surface was obtained, using quarter micron diamond spray (Struers DP-Spray P, 0.25µm) on a separate stationary short nap pad. Final polishing using diluted colloidal silica (Struers OP-S) and a porous neoprene pad (Struers MD-Chem) had produced numerous surface pits and was not adopted into the polishing procedure.

Etching

Each polished sample was etched using a solution of 4.2g picric acid, 10mL acetic acid, 10mL water, and 70mL ethanol. Considering the small size of the samples, and hazards associated with picric acid spills, a chemical dropper was used to etch the samples. Samples were etched for ten seconds, rinsed with methanol, and dried with compressed air.

APPENDIX D: Consistency between Rings of Cast Ingot

Compression tests were conducted on samples extracted from various locations of the AZ31B cast ingot. The stress-strain curves, corrected using standard true stress and true strain equations, obtained for ring 7 (Ø210mm) and ring 8 (Ø240mm) of the Ø304.8mm cast ingot under various deformation conditions are presented in Figure D-1. For an intermediate temperature of 400°C and at strain rates of $10^{-1}s^{-1}$, $10^{-2}s^{-1}$ and $10^{-3}s^{-1}$, it was evident that the compression behaviour was very similar between the two rings. Both samples deformed at a strain rate of $1.0s^{-1}$ exhibited cracking, and thus the results were omitted from the study. Furthermore, the final geometries of the samples were very consistent between the two rings.

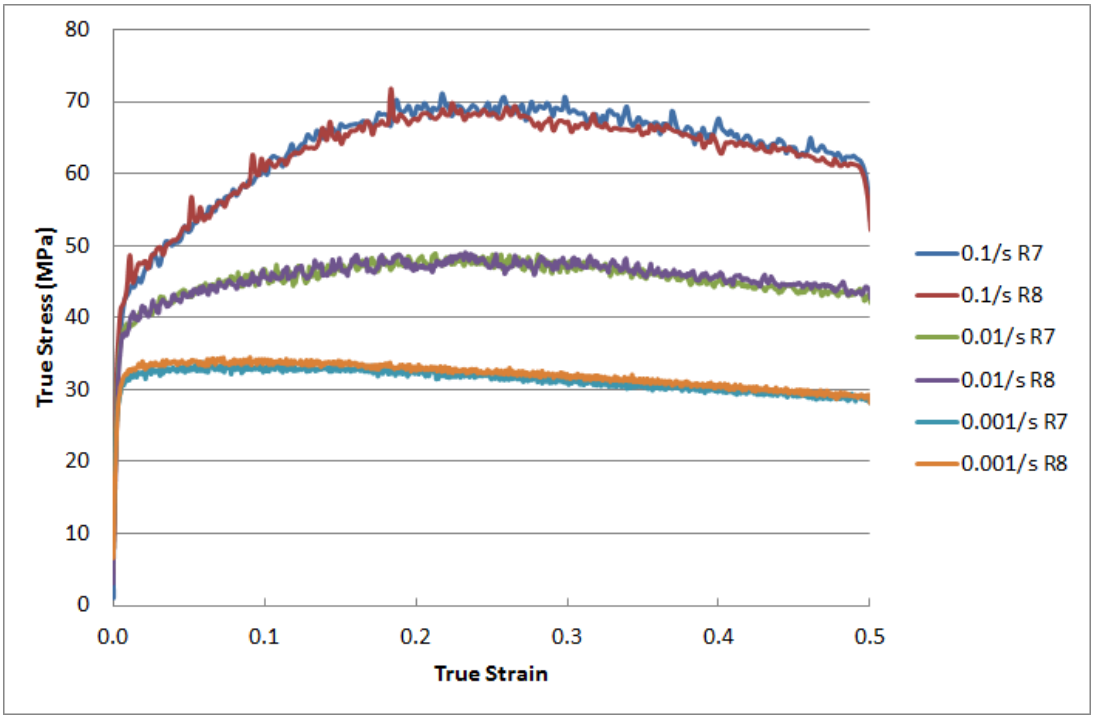

Figure D-1: Flow stress curves for rings 7 and 8 of the cast ingot, at 400°C and various strain rates.